Spring 2021

Force regulation in contractile cells by chemical and mechanical signaling

Esteban Vazquez-Hidalgo
Claremont Graduate University

Force regulation in contractile cells by chemical and mechanical signaling

by
Esteban Vazquez-Hidalgo

Claremont Graduate University and San Diego State University
2021

Approval of the Review Committee

This dissertation has been duly read, reviewed, and critiqued by the Committee listed below, which hereby approves the manuscript of Esteban Vazquez-Hidalgo as fulfilling the scope and quality requirements for meriting the degree of Doctor of Philosophy.

Parag Katira, Chair
San Diego State University
Associate Professor, Department of Mechanical Engineering

Paul Paolini, Member
San Diego State University
Professor Emeritus, Department of Biology

Christal Sohl, Member
San Diego State University
Associate Professor, Department of Biochemistry

Ali Nadim, Member
Claremont Graduate University
Professor, Institute of Mathematical Sciences

Claudia Rangel-Escareño, Member
Claremont Graduate University
Adjunct Professor, Institute of Mathematical Sciences

"Don't underestimate the force."

Darth Vader

Abstract

Force regulation in contractile cells by chemical and mechanical signaling

by
Esteban Vazquez-Hidalgo

Claremont Graduate University and San Diego State University: 2021

Chemical and mechanical signaling are essential for physiological processes. Dysregulation of these signals can promote disease states by altering force generation. It is crucial that we understand how these signals affect force generation and the implication of that force in health and disease. We approach this by investigating cells from two types of tissues: heart tissue cells and epithelial tumor cells. Chemical signaling by intracellular calcium directly regulates heart contractions. Altered calcium handling in heart cells is known to affect force generation in the heart, leading deleterious effects resulting in cardiovascular disease. Chemical and mechanical signaling in epithelial affect epithelial cell force generation. Responses to chemomechanical signals that increase force by epithelial cells has been shown to increase metastatic potential in tumors. The need to understand how these signals affect force generation could provide new insights in identifying targets for treatment. We use computational models to help us gain mechanistic insight into how cells regulate force generation as a response to chemical and mechanical cues.

To Julie

Acknowledgements

I have so many people to thank, who have contributed in a significant way in the pursuit of my dreams. I would first like to thank my advisors and mentors Dr. Paul Paolini and Dr. Parag Katira. Thank you for your endless support, encouragement, and friendship. Thanks for pushing me when I needed it, and knowing when to stop when I didn't. Dr. Christal Sohl, thank you for being there when things got tough. Dr. Ali Nadim and Claudia Rangel-Escareño, thank you for you feedback during my time in grad school. CSRC professors: Dr. Peter Blomgren, Dr. James Otto, Dr. Sam Chen, and Dr. Robert Edwards. Dr. Jose Castillo, thank you for all you've done. UCLA collaborators: Dr. Amy Rowat and Dr. Tae-Hyung Kim. My CGU cohorts: Dr. Lixia Zhu, Dr. Siddhi Tavlidar, Dr. Hareshram Natarajan, Dr. Peter Calhoun, Dr. John Waynelovich, Dr. Daniel Cuevas, and Dr. Genivaldo Silva. My peer mentors: Dr. Luis Escalona, Dr. Johnny Corbino, Dr. Omair Zubairi, Dr. Mariangel Garcia. My labmates in the Katira lab: Ashrith Reddy, Esra Tiftik, Benjamin Yeoman, Jamey O'Neill, James Julian, Nadia Beydoun, Tyler Collins, and Jhovanna Garcia. My labmates in the Paolini lab: Dr. David Torres-Barba, Dr. Xian Zhang, Dr. Carlos Bazan, and Elesha Bartolotta. SDSU faculty/staff: Dr. Cathie Atkins, Dr. Estralita Martin, Dr. Sanford Bernstein, Dr. Forest Rowher, Dr. Vi Vu, Dr. Alejandra Morlett Paredes, Parisa Plant, Thomas Zink, Thelma Chavez, and Maureen Paolini. Friends: Sara, Stasi, Eric, Ray, Andy, Carly, Amelia, Jacob, and Juana. Thank you all for your patience and understanding. My extended family: Kay, Hugh, Mike, Michelle, and Audrey– it's time for a visit. My parents Esteban and Raquel, and my sister, Raquel– I'm thankful you are always nearby.

Lastly, Julie, Elena, and Josie– I couldn't have done this without you.

Contents

List of Figures

List of Tables

Chapter 1

Introduction

Contractile cells, such as muscle cells and epithelial cells, are cells with intracellular structures that decrease in length in response to a trigger. Contraction can be local where only part of the cell contracts, or cellular, where the whole cell contracts. Contractile cells exhibit a wide range of behaviors that arise from actin and myosin activity. Actin and myosin form a force generating contractile unit. The force generated by the actin-myosin complex is crucially significant in health and disease.

Actin-myosin contractility determines heart health. Healthy hearts generate sufficient force to pump blood to all the tissues. The efficiency of each pump improves with exercise. Hearts benefit from exercise training. Force develops faster, blood is ejected more efficiently, and heartbeats decrease in frequency. Hearts with decreased force generation suffer systolic heart failure; the heart simply cannot generate sufficient force to pump blood out of the heart.

Epithelial cells exhibit migratory behaviors that result from intracellular actin-myosin forces. Indeed, cellular migration by contractile cells plays a major role in developmental and physiological processes. Cellular migration is the process by which a cell translocates in a directed manner i.e., not random. During embryonic development, cells migrate to form the endoderm, mesoderm, and ectoderm. Each will engage in further differentiation and migration to form all the different tissues in the body. Cells

also migrate to maintain physiological health. For example, cell migration mediates immune response where neutrophils in the bloodstream migrate to an infection site to neutralize infections or destroy invading pathogens. Cell migration is necessary for tissue repair and wound healing. In some instances, cell migration might be undesired as it can contribute to chronic inflammatory disease, vascular disease, tumor formation, and metastasis.

Our interest is to understand how forces are generated and regulated in cardiac and epithelial cells. To explain the roles that actin-myosin contractility plays, we first describe what actin and myosin are, what contractility is, and how actin-myosin contractility affects cellular behavior.

1.1 Actin and Myosin

Actin is an abundant protein found in eukaryotic cells and plays a vital role in intracellular processes. Furthermore, actin is an essential component of cytoskeletal structures such as microfilaments and intermediate filaments. *De novo* actin is synthesized as a monomer. Newly synthesized acting is a polar globular protein (G-actin) with a positive and negative end. Nucleating factors, such as ARP2/3, initiate G-actin polymerization into double helical filaments (F-actin) [1]. F-actin polymerizes by the sequential addition of G-actin monomers to the positive end of the newly formed G-actin aggregate (Figure 1.1A-C). In its filamentous form, actin is a main component of the cytoskeleton giving cells shape and structure. In contractile cells, actin has a secondary role: to provide a substrate for motor proteins, like myosin, to do work.

Myosin is a motor protein. It converts chemical energy from ATP hydrolysis into mechanical work. Myosin is a superfamily consisting of 15 myosin classes [2]. Myosins serve different functions but have similar structures and domains. Of the 15 classes, we are interested in myosin II. Myosin II is found in skeletal, cardiac, and smooth muscle cells as well as in non-muscle cells, such as epithelial cells. Myosin II consists of 3 domains: head, neck, and tail. The head domain contains two functional regions: one is an actin binding site and the other is an ATP binding site. The neck region regulates

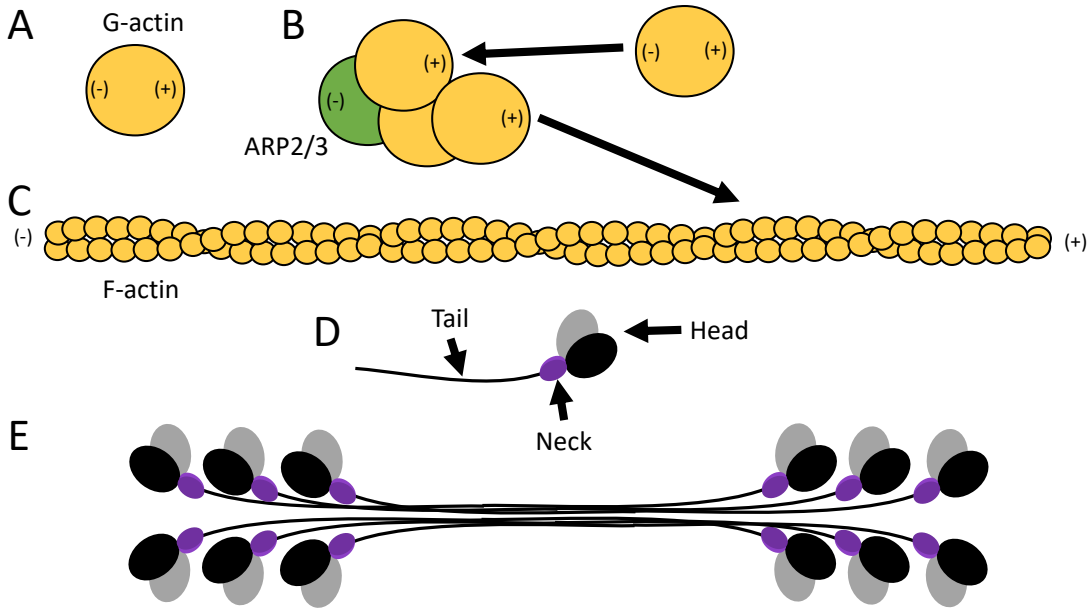

FIGURE 1.1: A) Actin synthesizes *de novo* as a globular polar monomer, G-actin. B) Nucleation factors, like ARP2/3, initiate actin polymerization by adding actin monomers to the positive end of the growing filament. C) Filamentous actin, F-actin, is a parallel double helix with a positive and negative end. D) Myosin contains 3 regions: Head, neck, and tail. E) Myosin tails interact with each other to form parallel bundles that interact with the tails of other myosin tails to form a myosin ensemble with heads at both ends.

the availability of the head domain to engage in ATP hydrolysis. Mechanically, the neck acts as a lever to transfer the myosin head movement onto actin. The tail domain interacts with tail domains of other myosin II. These tail-tail interactions result in bipolar molecules with myosin heads at opposite ends and tails in the middle [3] (Figure 1.1D-E).

1.2 Actin-Myosin Organization

Actin and myosin work together as a contractile unit. Actin-myosin contraction only happens when actin and myosin organize in a specific way, first described by observing actin-myosin organization in muscle cells [5]. In muscle cells, actin and myosin

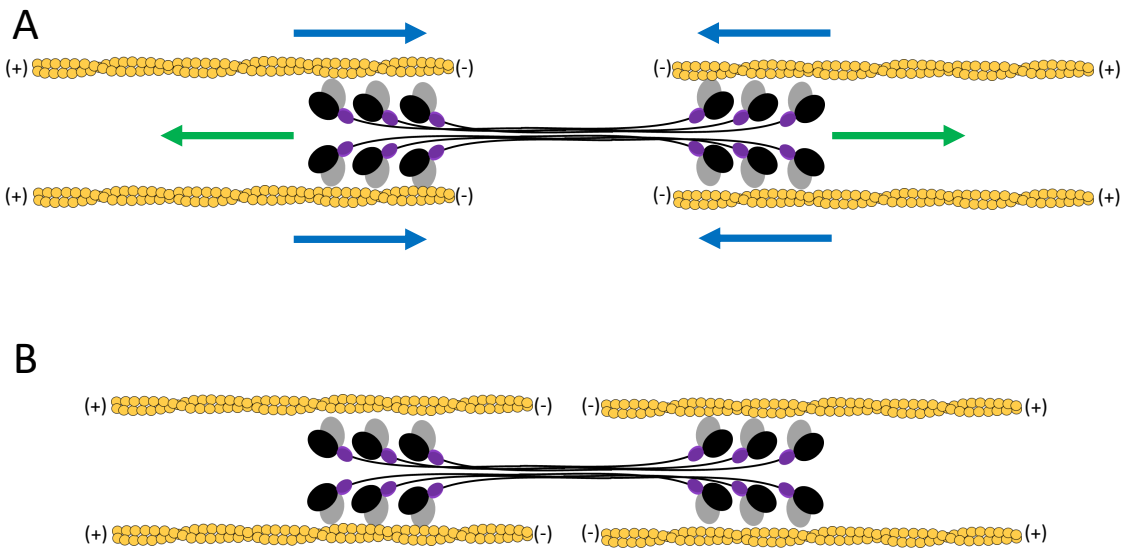

FIGURE 1.2: A) Sarcomeres consists of parallel bundles of actin filaments orient themselves with their negative end pointed toward each other and their posive ends pointed away. Myosin sits between the two bundles of parallel actin filaments. Myosin "walks" towards the positive end of actin (green arrows). Actin is displaced in the opposite direction (blue arrows). B) Sarcomere contraction decreases the spacing between the two bundles of parallel actin filaments without altering the length of either protein [4].

form highly organized repeating contractile units called sarcomeres. Sarcomeres are basic contractile units that consist of bundles of parallel thin (actin) and thick (myosin) filaments. Two bundles of parallel actin filaments orient their negative ends pointing towards the middle of the sarcomere and the positive ends pointing outwards. In between the actin filaments lies the bipolar myosin filament. This orientation, with myosin sitting between two groups of parallel actin filaments is called sarcomeric orientation. Figure 1.2 shows a schematic view of sarcomeric orientation.

Contraction occurs when myosin binds to actin, hydrolyzes ATP, and walks towards actin's positive end. Myosin displaces actin in the opposite direction of myosin's walking. As myosin walks, it remains stationary realtive to the actin displacement. It is essentially treadmilling by displacing actin. As actin is displaced, the gap between the bundles of parallel actin filaments decreases. Sliding filament theory states contraction

occurs when actin filaments slide by myosin filaments without a change in length of the contractile proteins [6]. That is, during contraction neither the length of the actin filament nor the length of the myosin filament change–only spacing between bundles of parallel actin filaments decreases. Other types of actin-myosin non-sarcomeric orientations are possible (Figure 1.3). When myosin sits between a two parallel actin filaments, instead of in between two bundles of parallel filaments, myosin simply walks along the filaments like a train on tracks. Another orientation occurs when actin organize themselves in an antiparallel orientation and depending on the orientation of surrounding actin-myosin complexes, force may or may not be generated.

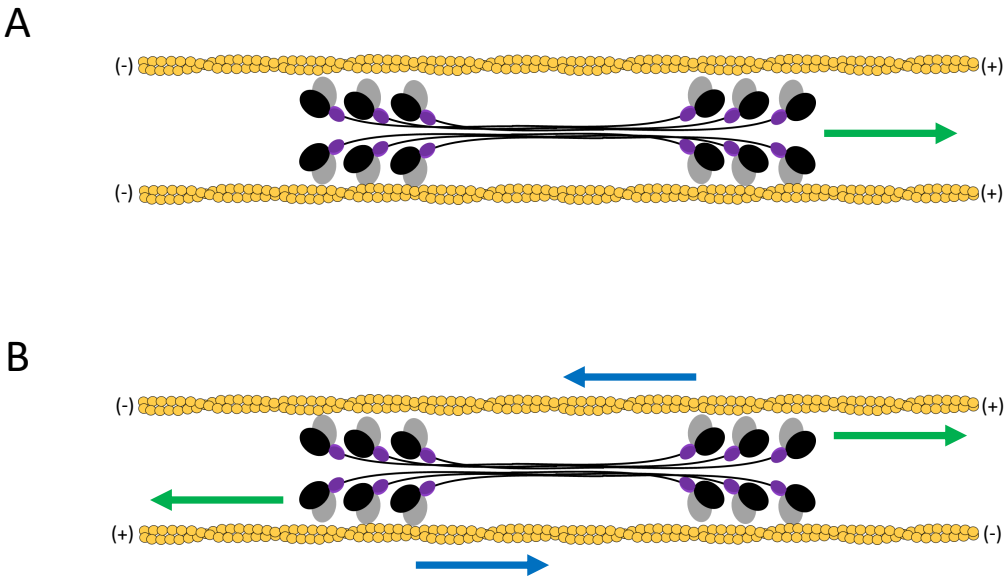

FIGURE 1.3: Actin and myosin organize in non-sarcomeric orientations. A) Uniform organization occurs when myosin sits between two parallel actin filaments. Myosin moves towards actin's positive without displacing actin. B) Mixed orientation has myosin sitting between anti-parallel actin filaments myosin walks towards opposing positive end, but not necessarily generating force [4].

1.3 Actin-Myosin Force Regulation

Sarcomeric actin-myosin contractility generates force. Sarcomere orientations can be highly organized, as in skeletal and cardiac muscle cells, or less organized, like in epithelial cells. Nonetheless, contractile cells are able to use this force to affect their environments.

Contractile cells regulate force generation as a response to some environmental signal. Some of these signals are of interest to us. Specifically, we are interested in how force generation is regulated in cardiac cells by calcium signaling. In epithelial cells we are interested in force generation in response to mechanical and chemical cues.

This dissertation builds on our current understanding of cellular and molecular dynamics that regulate force generation at the cellular and molecular level. In the following chapters, we will discuss specific chemical and mechanical triggers of force generation and their effect on cardiac and epithelial cells. We use computational models to help us gain mechanistic insight into how cells regulate force generation as a response to chemical and mechanical signals.

Chapter 2

Calcium Signaling in Cardiocytes

The heart is a pump that transports necessary blood to the tissues to deliver nutrients, remove metabolic waste, and aid in gas exchange. Tasked with these functions, the heart is the first organ to develop and become functional [7, 8]. Unlike other organs, the heart begins to function while it continues to develop. Heartbeats are detectable in early developmental stages (embryonic day 22 (ED 22) in humans, ED 9 in rats)[7]. At this stage, the heart is a beating tube (Figure 2.1) with a functioning excitation-contraction coupling (ECC) mechanism [9]. ECC describes the communication that starts with electrical signals, transduced by calcium signals, and results in mechanical pumping [10].

2.1 Calcium Signaling

Cells possess the ability to receive, process, and transmit signals to its immediate environment, to cells over short or great distances, or with itself [13]. Heart cells are able to detect different signals, such as electrical signals, transduce them, and respond to the signal in the form of a contraction. While cardiac electrical signaling has its own relevance in heart health and disease, we focus on the force regulating intracellular signal that is the calcium signal. Calcium (Ca^{2+}) is a necessary ion in cardiac contraction regulation [10, 14, 15]. Cytosolic Ca^{2+} concentrations ($[Ca^{2+}]$) fluctuate cyclically during

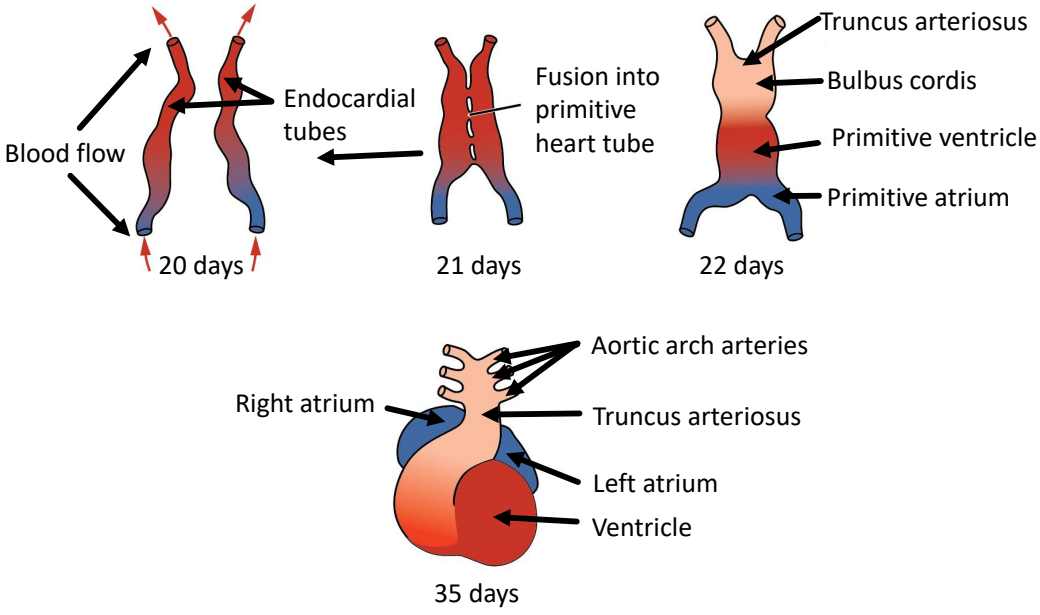

FIGURE 2.1: The heart is the first functioning organ. At early developmental stages, the heart is a pair of tubes that undergoes fusion. The heart tubes contain the tissues that will undergo further differentiation and morphogenesis to become the atria, ventricles, valves, and blood vessels. At embryonic day 22 (ED 22), heart beats are detected. By ED 35, the heart is fully formed [11, 12]

contraction and relaxation. An increase in $[Ca^{2+}]$ initiates contraction and removal of Ca^{2+} terminates contraction. The strength of the contraction is regulated by the amplitude and duration of the Ca^{2+} transient [14]. The Ca^{2+} transient represents the change in cytosolic $[Ca^{2+}]$ over time.

Prior to contraction, diastolic cytosolic $[Ca^{2+}]$ is low, approximately 100 nM. At its peak, cytosolic $[Ca^{2+}]$ increases upwards of 1μM [16]. Contraction ceases when Ca^{2+} levels decrease and revert to their diastolic levels. Cytosolic Ca^{2+} increases when the electrical signal from the pacemaker cells depolarize the cardiocyte sarcolemma (SL) membrane. Cardiocytes maintain a membrane potential by selectively shuttling sodium (Na^{+}) and potassium (K^{+}) ions across either side of the membrane. Ion channels and pumps are responsible for creating and maintaining the membrane potential. Electrical stimulation depolarizes the membrane potential and activates ion channels. The channels work as gates to prevent ions from inwardly diffusing with the gradient. When the voltage-gates are open, Ca^{2+} ions passively diffuse with the chemical gradient. Extracellular calcium concentrations are approximately 1.4 mM [17], orders of magnitude greater than intracellular diastolic Ca^{2+} concentrations, making the inward diffusion of Ca^{2+} favorable. Calcium enters the cell via the sarcolemmal voltage-gated L-type Ca^{2+} channels (LTCC) and diffuses into the cytosol. This newly entered Ca^{2+} does not initiate contraction, but it is responsible for releasing the Ca^{2+} that initiates contraction [14, 18–21].

Relatively low concentrations of extracellular Ca^{2+} diffuse across the cytosol until it reaches the sarcoendoplasmic reticulum (SR). The SR is an internal Ca^{2+} reservoir with a $[Ca^{2+}]$ approximately 700 nM, appreciably higher than the cytosolic calcium concentration, making diffusion from the SR into cytosol favorable [22]. Ryanodine receptors (RyR) are sensitive to small increases in cytosolic calcium concentration. SR Ca^{2+} is released when extracellular Ca^{2+} activates Ca^{2+} sensitive ryanodine RyR on the surface of the SR membrane. Upon activation, RyR opens and the SR rapidly releases the stored Ca^{2+} into the cytosol. Cytosolic calcium concentrations peak milliseconds after RyR activation.

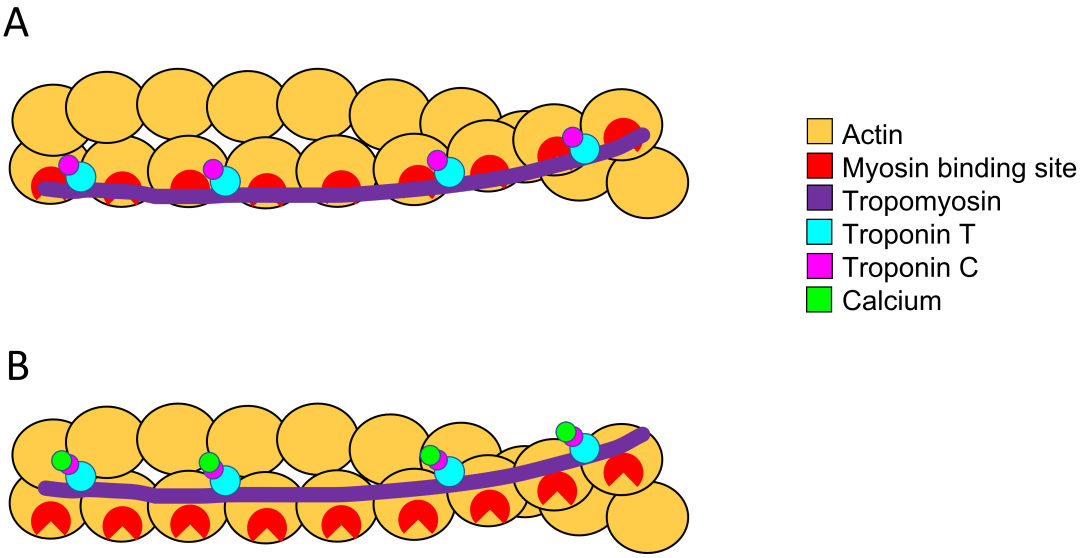

FIGURE 2.2: Tropomyosin is a filamentous protein that runs alongside actin. The troponin complex attaches to tropomysin and actin. A) At low cytosolic calcium concentrations, the tropomyosin-troponin complex blocks the myosin binding sites on actin. When calcium diffusion reaches the sarcomere, calcium binds to troponin C, causing a conformational change that results in the tropomysosin-troponin complex to shift, revealing the mysosin binding sites (B).

As cytosolic [Ca^{2+}] increases, it diffuses to the sarcomeres. Skeletal and cardiac sarcomeres contain tropomyosin [23]. Tropomyosin is a filamentous protein, similar to F-actin, that twists alongside actin filaments, blocking the myosin binding sites on actin. Tropomyosin has 3 additional proteins attached to it: troponin T, troponin C, and troponin I [23, 24]. Troponin T binds the troponin complex (troponin T, C, and I) to tropomyosin. Troponin C has a calcium binding domain and a troponin I binding domain. Troponin I attaches to actin, holding the tropomyosin-troponin complex in place. When Ca^{2+} reaches the sarcomeres, it binds to troponin C causing a conformational change. This results in troponin I detaching from actin, which causes a shift in tropomyosin, exposing the myosin binding sites on actin [25, 26].

With tropomyosin out of the way, myosin is unrestricted to bind to actin to initiate contraction via ATP (adenosine triphosphate) hydrolysis to produce ADP (adenosine diphosphate) and energy.

$$\mathrm{ATP} + \mathrm{H_2O} \longrightarrow \mathrm{ADP} + \mathrm{P_i} + \text{energy}$$

The conceptual model that describes the temporary attachment of myosin to actin to generate force is the crossbridge cycle [6, 27]. The states in the crossbridge cycle are:

1. Myosin is dissociated from actin. ATP binds to myosin.
2. Myosin moves into position, ready to bind to actin. ATP is hydrolyzed into ADP and phosphate (P_i).
3. Myosin binds to actin.
4. Myosin generates force, displacing ADP and (P_i). Myosin is ready to repeat the cycle.

Elevated [Ca^{2+}] activates the removal process of cytosolic Ca^{2+}. Activation of the sarco-endoplasmic reticulum calcium-ATPase (SERCA) pump and the sodium-calcium exchanger (NCX) regulate in this process. SERCA is located at the SR membrane and actively pumps Ca^{2+} from the cytosol into the SR. NCX, on the other hand, is located

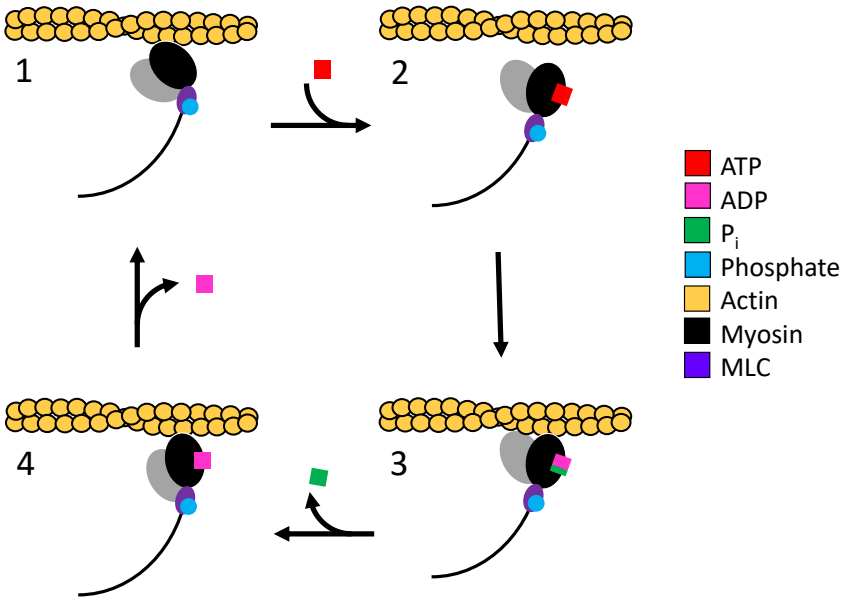

FIGURE 2.3: The crossbridge cycle (tropomyosin-troponin complex not shown) shows how myosin generates force by hydrolyzing ATP and its position relative to actin at each state. ATP causes conformational changes in myosin. The binding and hydrolysis of ATP are mechanically significant for myosin. ATP binds to myosin and is hydrolyzed, priming myosin for binding. Myosin binds, engages in the powerstroke cycle, and releases ADP. Each step in the crossbridge cycle has a forward rate, except for ATP hydrolysis. ATP hydrolysis is reversible and is represented by the reverse reaction.

at the sarcolemma and removes Ca^{2+} by exchanging it with sodium. Every calcium ion is exchanged for 3 sodium ions [28]. In this manner, calcium released from the SR is returned to the SR and calcium that originated from the extracellular space is returned to the extracellular space.

Proper regulation of cytosolic calcium concentrations by RyR, SERCA, and NCX is necessary for heart functions. Alterations in expression levels of RyR, SERCA, and NCX have been identified in cases of cardiovascular disease. The regulation of Ca^{2+} cyclilng is critically important as the strength of contraction is regulated by the amplitude and duration of the Ca^{2+} transient [20]. Examples of altered Ca^{2+} transients are evident in some cardiovascular diseases.

2.2 Calcium signaling dysregulation

Changes in Ca^{2+} handling are observed with certain cardiovascular diseases [29]. Altered expression or activity of Ca^{2+} regulating proteins are known to change the contractile behavior of the cell and the heart. Incomplete removal of cytosolic Ca^{2+} results in elevated diastolic $[Ca^{2+}]$ that triggers spontaneous RyR Ca^{2+} release [30] leading to arrhythmic cardiac function [31]. Improper Ca^{2+} handling can occur by RyR, SERCA, or NCX. Failure to remove cytosolic Ca^{2+} can activate RyR. RyR is sensitive to cytosolic $[Ca^{2+}]$ and can release SR Ca^{2+} spontaneously, or it can be "leaky", further increasing cytosolic $[Ca^{2+}]$ [32–34]. SR Ca^{2+} uptake by SERCA is reduced in the failing human heart [29]. The reduced uptake can happen either by down-regulated SERCA expression or suppressed SERCA activity [35] with NCX activity increasing to compensate for SERCA's inability to lower cytosolic $[Ca^{2+}]$ [36]. These observations show that Ca^{2+} handling has a role in heart disease and that some compensatory response is present to maintain physiological cytosolic $[Ca^{2+}]$.

To study Ca^{2+} regulation further, we use neonatal rat cardiomyocytes. Unlike adult cardiocytes that are rod-like, neonatal cardiocytes are spherical and have minor anatomical differences. Adult cardiocyte membrane voltage receptors are found in sarcolemmal invaginations, called T-tubules. T-tubules are pocket-like structures that probe into the

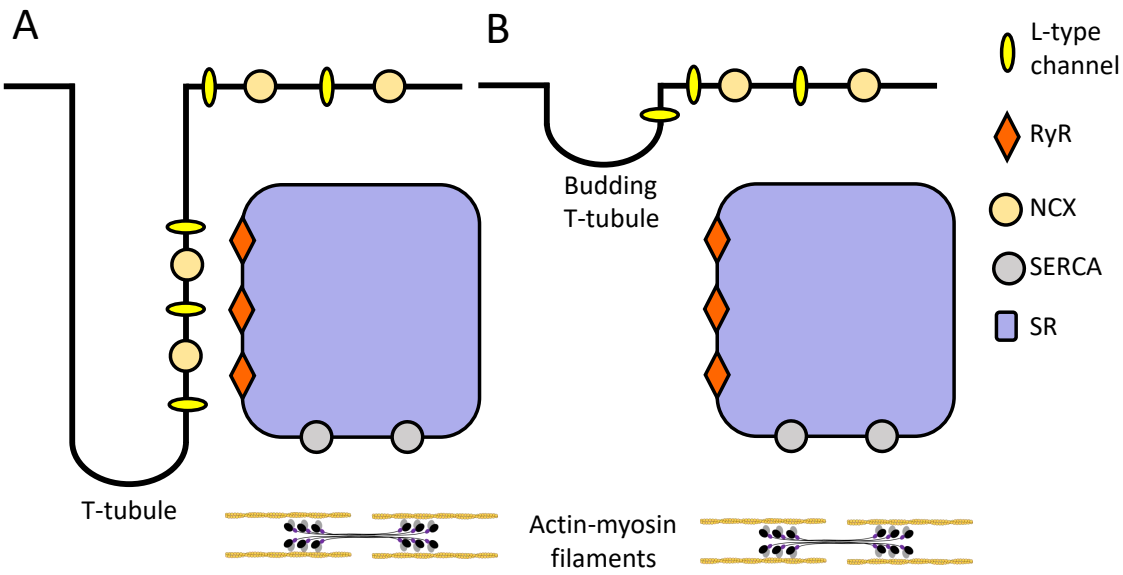

FIGURE 2.4: A) Adult cardiocytes contain T-tubules, specialized invaginations that serve to minimize the distance that extracellular calcium diffusion distance. T-tubules bring LTCCs close to RyR. B) Neonate cardiocytes do not contain T-tubules, or contain budding T-tubules. Extracellular calcium has to diffuse over a greater distance since the LTCCs are far from RyR.

cell. The invaginations bring the LTCCs closer to the SR inside the cell, minimizing the distance between the LTCC and the RyR receptor. Neonatal cardiocytes either lack T-tubules structures or have budding T-tubules that are starting to form. The LTCCs are farther from RyR and Ca^{2+} has to diffuse across a greater distance. The morphological differences do not affect the mechanisms that regulate cytosolic [Ca^{2+}].

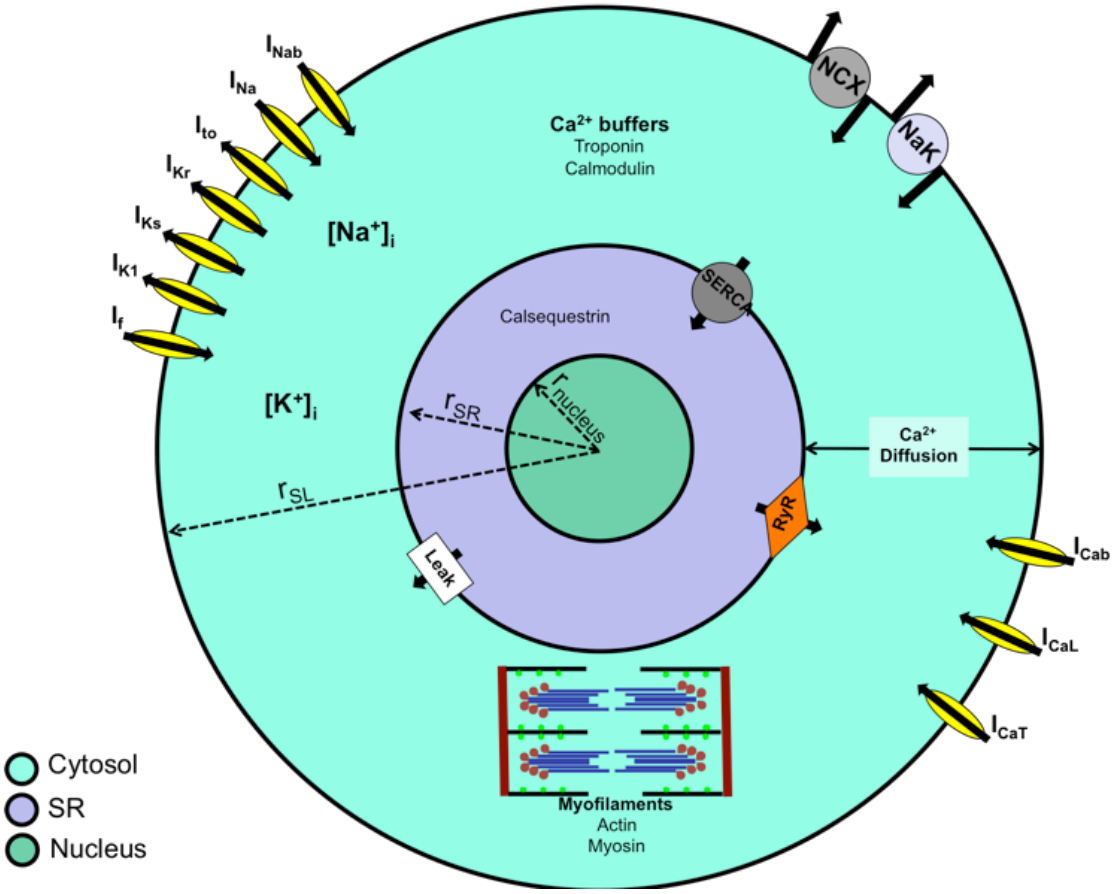

FIGURE 2.5: Model representing a neonate cardiocyte. Ca^{2+} enters primarily by the inward LTCC, I_{CaL}. Other voltage-gated channels, I_f,I_{K1},I_{Ks}, I_{Kr}, I_{to}, I_{Na}, I_{Nab}, I_{Cab}, and I_{CaT} regulate the membrane potential. Ca^{2+} diffuses across the cytosol, activating RyR to releases Ca^{2+} from the SR stores. Ca^{2+} then causes a conformational change in troponin at the myofilaments, initiating contraction. Increased cytosolic [Ca^{2+}] activates SERCA and NCX to return SR Ca^{2+} back to the SR and extracellular Ca^{2+} back to the extracelluar space. Removal of cytosolic Ca^{2+} terminates contraction.

Chapter 3

Downregulation of RyR and NCX in the neonatal rat ventricular myocyte modulates cytosolic [Ca^{2+}]

Esteban Vazquez-Hidalgo[1,3]

in collaboration with

Xian Zhang[3]

David Torres Barba[1]

Paul Paolini[1], 3

[1]Computational Science Research Center, San Diego State University, San Diego, CA, 92182, United States

[2]Mechanical Engineering, San Diego State University, San Diego, CA, 92182, United States

[3]Biology, San Diego State University, San Diego, CA, 92182, United States

Funding Information California Metabolic Research Foundation

Article preprint can be found at: https://doi.org/10.1101/2021.10.20.465171

3.1 Abstract

Calcium (Ca^{2+}) is necessary for cardiac muscle contraction. RyR, NCX, and SERCA are key regulatory protein channels for cytosolic Ca^{2+} in the cardiomyocyte. Expression levels of these proteins are a function of development and disease. We investigated how downregulation by siRNAs of RyR and NCX affected expression levels of complimentary proteins their corresponding intracellular Ca^{2+} transients. We compared the experimentally observed Ca^{2+} transients to those predicted by mathematical models. Experimental results show RyR downregulation decreased SERCA and increased NCX protein levels. The associated Ca^{2+} transient had decreased amplitude, increased time-to-peak (TTP), time-to-50% (T_{50}), and time-to-90% (T_{90}) Ca^{2+} removal with respect to the control population. NCX downregulation increased SERCA production without significant changes in RyR expression levels. The corresponding Ca^{2+} transient increased amplitude, no change in TTP and T_{50} Ca^{2+} removal, but increased T_{90} Ca^{2+} removal with respect to the control population. Computational models that accurately predict the observed experimental data suggest compensatory changes occurring in the expression levels as well as biochemical activity of the regulatory proteins.

3.2 Introduction

The heart is a pump that transports necessary blood to the tissues to deliver nutrients, remove metabolic waste, and aid in gas exchange. Tasked with these functions, the heart is the first organ to develop and become functional [7, 8]. Heart beats are detectable in early developmental stages (embryonic day (ED) 22 in humans, ED 9 in rats)[7]. At this stage, the heart is a beating tube with a functioning excitation-contraction coupling (ECC) mechanism [9] that controls electrical signals to mechanical pumping [10], establishing early on the importance of producing controlled cardiac contraction from electrical stimulation and ionic flux balance.

Each heart beat is the result of numerous orchestrated multiscale efforts. Our study

is at the cellular and molecular level, focusing on Ca^{2+} flux handling. Ca^{2+} is a necessary ion in heart contraction [14] as the strength of cardiac contraction is regulated by the amplitude and duration of the Ca^{2+} transient [20]. Specifically, we are interested in learning how cytosolic [Ca^{2+}] behaves in cultured neonatal rat ventricular myocytes (NRVMs) when short interfering RNAs (siRNA) are used to independently inhibit protein expression of the Na^{+}/Ca^{2+} exchanger (NCX1, refered to as NCX) and the cardiac isoform of ryanodine receptors (RyR2, refered to as RyR). Furthermore, we are interested in observing any compensatory changes in protein expression of RyR, NCX, and the sarcoendoplasmic reticulum Ca^{2+}-ATPase (SERCA) pump when RyR and NCX are downregulated.

NRVMs are a robust model used to study mechanical and physiological properties [20, 37], develop spatiotemporal computational models of ECC [15, 19], and investigate drug-induced differential gene expression [38]. Similarity between post-natal and diseased adult cardiomyocytes has been used as a rationale for using NRVMs as a model to study certain aspects of cardiovascular disease, such as Ca^{2+} handling and ECC[39]. We acknowledge that NRVMs *in vivo* and *in vitro* are morphologically different [40, 41] from healthy and diseased adult myocytes with the immature myocytes being spheroid while healthy and adult myocytes are rod-like [42]. However, in diseased hearts, transverse tubule (t-tubule) density within the adult myocytes decreases or their position drifts. This drift changes the proximity of the sarcolemmal (SL) L-type Ca^{2+} channel (LTCC) to the sarcoplasmic reticulum (SR) RyR channels [43–45], essentially leaving "orphaned" RyR channels resulting in altered extracellular and SR Ca^{2+} fluxes [18, 46–49].

We begin by an independent knockdown of RyR and NCX. We measure relative protein expression of RyR, NCX, and SERCA for each knockdown followed by fluorescence intensity measurements of free cytosolic [Ca^{2+}] for each knockdown group. Lastly, we use an established computational model calibrated to our experimental conditions to identify underlying dynamics mechanistic implications not explained by differential protein expression.

3.3 Material and Methods

Experiments were carried out in accordance with institutional and federal guidelines. Animal use protocols were approved and supervised by San Diego State University Office of Laboratory Animal Care and the Institutional Animal Care and use Committee.

All procedures were done according to manufacturer's protocols unless otherwise stated.

3.3.1 Neonatal Rat Ventricular Myocyte Isolation

NRVMs were harvested from litters of 1-day old Sprague-Dawley (*Rattus norvegicus*) hearts. The ventricles were separated from the hearts and placed in air compatible Dulbecco's Modified Eagle's Medium (DMEM)(Thermo Fisher, CA). The ventricles were pooled, minced, and enzymatically isolated by seven rounds of trypsin (Invitrogen, CA) at 37°C. After each digestion round, the supernatant was removed and placed in DMEM/F12 (Thermo Fisher, CA) containing 20% fetal bovine serum (FBS) (Thermo Fisher, CA). NRVMs were pre-plated for 2 hours to remove fibroblasts [50].

3.3.2 Gene Silencing

We use downregulation by siRNA as we are interested in altering gene expression in healthy cells vs. using genetically modified cells from animals with congenital abnormalities. Stealth RNAi and scrambled oligo-ribonucleotide duplex (Invitrogen, CA) were used. Reverse transcription of siRNAs were preformed with TransMessenger Transfection Reagent (Qiagen, USA). Fluorescently labeled dsRNA oligomer, BLOCK-iT (Thermo Fisher, CA), optimized delivery rates. Transfections were done prior to NRVM seeding. Gene of interest (GOI) siRNA or control siRNA were incubated at room temperature with Enhancer R and Buffer EC-R (Qiagen, USA) for 20 minutes. TransMessenger Transfection Reagent was added and incubated for an additional 10 minutes at room temperature. Immediately after room temperature incubation, NRVMs with transfection mixtures were placed in DMEM-air at 37°C, 5% CO_2, for 4-6 hours. Transfection

mixtures and DMEM-air were removed and replaced with DMEM/F12 supplemented with 10% FBS, incubated for 48 hours at 37°C and 5% CO_2.

3.3.3 Western Blots

NRVMs for western blots were pooled and plated in 6-well plates at 0.5×10^6 cells per well from 12 ventricles. NCX and RyR knockdown were performed on separate populations from different litters, each with a control group from the respective group. Protein was extracted 48 hours post transfection with All Prep RNA/Protein Kit (Qiagen, USA). Protein concentrations were determined by Lowry assay (Bio-Rad, CA). 20 μg of total protein was denatured at 70°C for 10 minutes and loaded in 3-8% Tris-Acetate Gel (Invirogen, CA) for NCX and RyR2, running in 1×Tris-glycine SDS Running Buffer (Invitrogen, CA) at 125V for 90 minutes. Proteins were transferred to 0.45 μm pore size nitrocellulose membrane in 1×NuPage Transfer Buffer (Invitrogen, CA). SERCA proteins were loaded in 4-12% Bis-Tris Gels (Invitrogen, CA) running in 1×MOPs SDS running buffer (Invitrogen, CA) at 150V for 90 minutes and transferred to 0.45 μm pore size PVDF membrane (Invitrogen, CA). 0.5% Ponceau-S was used for protein visualization followed by a 5% non-fat milk block buffer for 1 hour at room temperature. Membranes were then transferred to fresh blocking buffer with diluted antibodies (RyR2 1:500, NCX 1:200, SERCA 1:2000, GAPDH 1:5000) (Jackson ImmunoResearch, PA) followed by overnight incubation on a shaker at 4°C. The following day, 3 10-minute TBST washes were performed followed by Western Lightning plus ECL Enhanced Chemiluminescence (Perkin Elmer, MA). Proteins were detected on x-ray film (Fuji, Japan). Protein levels were determined with Image J gel analysis tool kit (NIH, USA). Experiments were performed three times with triplicate samples. Unpaired t-tests were used with population means±SEM. Differences in the means were deemed statistically significant when $P < 0.05(^*)$, $P < 0.01(^{**})$, and $P < 0.001(^{***})$.

3.3.4 qRT-PCR Analysis

Relative mRNA levels were compared by reverse transcription quantitative polymerase chain reaction (qRT-PCR). Total mRNA was extracted from NRVMs with All Prep RNA/Protein Kit 48 hours post transfection. RNA was amplified in 48-well plates using Eco Real-Time PCR Detection System (Illumina, CA) with KAPA SYBR FAST One-Step qRT-PCR Kits (Kapa Biosystems, MI). NCX, SERCA, and RyR2 RNA samples were analyzed in triplicate using comparative CT value to determine fold change of mRNA expression. Data were normalized by GAPDH (see supplementary tables).

3.3.5 Calcium Transient Measurement

NRVMs for Ca^{2+} measurements were plated at 1×10^6 cells per well on fibronectin coated coverslips. Ca^{2+} fluorescence intensities were acquired with a dual emission photometry system (Photon Technology International, Lawrenceville, New Jersey) [51]. Briefly, 10μM of Fluo-3AM (Molecular Probes, Inc) in dimethly sulfoxide (DMSO) was added to 10 ml of 10% FBS supplemented with 0.05% pluronic F-127 (Molecular Probes, Inc). Each well was loaded with 1 ml of Fluo-3AM complex and incubated for 20 minutes. After incubation, NRVMs were washed with 1:1 media and the coverslip was placed onto an environmental stage chamber with 1 ml of 1:1 medium. NRVMs were field stimulated at 0.3 Hz for 3 msec duration at 50mV. Fluorescence intensity was measured using Felix computer software (Photon Technology International, Lawrenceville, New Jersey). Due to limitations by the use of non-ratiometric dye, experimental and computational baselines are set to [Ca^{2+}] = 0. Cytosolic free [Ca^{2+}] was approximated by the pseudoratio

$$[Ca^{2+}] = \frac{\Delta F}{F_0} \tag{3.1}$$

where ΔF is the fluorescence intensity and F_0 is the baseline measurement as described in [52] and as performed computationally by Korhonen et al [19].

3.4 Computational Model

Computational models for ventricular and atrial cardiac systems exist for adult animals. Some of the more recognizable adult ventricular models include rabbit [53], mouse [54], and human [55]. Fewer neonatal models exist. Fewer computational models exist for neonatal animals. There is a neonatal mouse ventricular model [15] and a neonate rat ventricular model [19]. Both models use ordinary differential equations to solve action potential based on ionic concentrations. We employ the mathematical model presented by Korhonen of NRVMs as it closely matches our cell geometry and initial conditions. The model takes into account action potentials based on potassium (K^+) and sodium (Na^+) currents as well spatiotemporal cytosolic changes in [Ca^{2+}] from the SL and SR. The model provides us with a method to perform a functional analysis of the Ca^{2+} cycling proteins NCX, RyR, and SERCA.

Our focus in this model are the equations related to RyR, NCX, and SERCA. The mathematical model describes the Ca^{2+} efflux from the SR via the RyR channel as

$$J_{RyR} = k_{RyR} P_{open} \left([Ca^{2+}]_{SRrelease} - [Ca^{2+}]_{subSR} \right) \tag{3.2}$$

where k_{RyR} is the RyR scaling factor, $[Ca^{2+}]_{SRrelease}$ is the [Ca^{2+}] from the SR, $[Ca^{2+}]_{subSR}$ is the [Ca^{2+}] immediately adjacent to the SR membrane, and P_{open} is the probability function of the channel being in the open state.

$$\frac{dP_{open}}{dt} = \frac{P_{closed} k_{open}}{1 + \left(\frac{K_{m,RyR}}{[Ca^{2+}]_{subSR}} \right)^4} - k_{close} P_{open} \tag{3.3}$$

k_{open} is the rate constant for RyR opening, k_{close} is the rate constant for RyR closing, and $K_{m,RyR}$ is the half-saturation for RyR. P_{closed} is defined as

$$P_{closed} = 1 - P_{open} \tag{3.4}$$

Ca^{2+} uptake into the SR is represented by a Hill-type equation

$$J_{SERCA} = \frac{V_{max}\left(\frac{[Ca^{2+}]_{subSR}}{K_{mf}}\right)^{H} - V_{max}\left(\frac{[Ca^{2+}]_{SRuptake}}{K_{mr}}\right)^{H}}{1 + \left(\frac{[Ca^{2+}]_{subSR}}{K_{mf}}\right)^{H} + \left(\frac{[Ca^{2+}]_{SRuptake}}{K_{mr}}\right)^{H}} \tag{3.5}$$

where V_{max} is interpreted as the SERCA scaling factor, H is the Hill coefficient, $[Ca^{2+}]_{SRuptake}$ is the $[Ca^{2+}]$ sequestered into the SR, K_{mf} is the SERCA forward half-saturation constant, and K_{mr} is the SERCA reverse half-saturation constant.

Ca^{2+} efflux to the extracellular space by NCX is described as

$$I_{NCX} = \frac{k_{NCX}[Na^{+}]_i^3[Ca^{2+}]_o e^{\gamma V} - e^{(\gamma - V)V}}{1 + d_{NCX}\left([Na^{+}]_o^3[Ca^{2+}]_{subSL} + [Na^{+}]_i^3[Ca^{2+}]_o\right)} \tag{3.6}$$

where k_{NCX} is the NCX scaling factor, d_{NCX} is the denominator scaling factor, γ is the energy barrier parameter, V is the total voltage, $[Na^{+}]_i$ is the cytosolic $[Na^{+}]$, $[Na^{+}]_o$ is the extracellular $[Na^{+}]$, and $[Ca^{2+}]_o$ is the extracelluar $[Ca^{2+}]$. For the full list of model equations, see [19].

Our experimental setup required changes to the model proposed in [19]. At the time of Ca^{2+}fluorescence measurements, our cultured NRVMs were larger, 14 μm vs 10μm and our culture media had higher $[Ca^{2+}]$, 1.9 mM vs 1.7 mM. The appropriate changes were made in the initial conditions to calibrate the model to obtain a control model for our experimental NRVM (Figure 3, Table 3). Using the observed Ca^{2+} transient from our control NRVM population, we performed minimal RyR, NCX, and SERCA parameters fitting to establish a model that predicted the expected Ca^{2+} response (Figure 3).

3.5 Results

3.5.1 Downregulation by siRNA

RyR downregulation by siRNA showed a decrease in RyR protein expression by 73% (±9% SEM), an increase in NCX protein expression of 51% (±6% SEM), and a decrease of SERCA expression by 31% (±12% SEM) (Figure 1A, Table 1). The associated Ca^{2+}

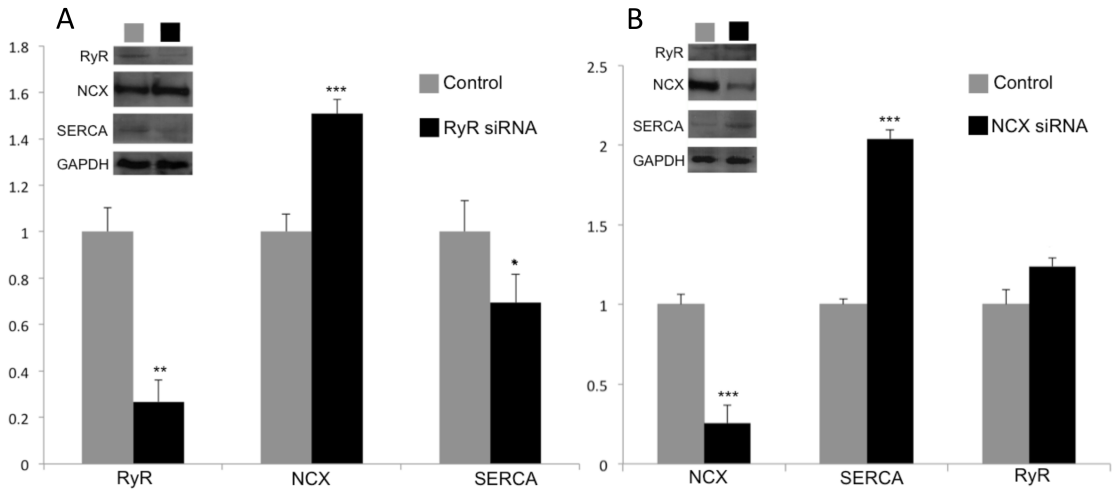

FIGURE 3.1: Western blots for RyR knockdown (A) and NCX knockdown (B) efficacy. NRVMs with RyR knockdown experienced increased NCX and decreased SERCA protein expression. NRVMs with NCX knockdown demonstrated increased SERCA expression and statistically insignificant change ($P \geq 0.05$) of RyR protein expression.

transients showed decreased amplitude, increased time-to-peak (T_{peak}) and increased time to 50% transient decay (T_{50}) with respect to the control (Figure 2A).

Inhibition of NCX by siRNA showed a decrease of NCX protein expression by 75% ($\pm$16% SEM), no statistically significant change in RyR expression, and an increase in SERCA expression by 104%($\pm$2% SEM) (Figure 1B). The associated Ca^{2+} transients showed increased amplitude, and no change to T_{peak} and T_{50} with respect to the control (Figure 2B, Table 1). Similar trends in increased or decreased transcripts of the target protein were observed by qRT-PCR analysis. Transcripts for RyR downregulation experiments decreased RyR by 65%, increased NCX by 75%, and decreased SERCA by 37%. Transcripts for NCX downregulation experiments decreased NCX by 79%, decreased RyR by 3%, and increased SERCA by 56% (Supplementary table 1). There will be some discrepancies in western blot and PCR measurements as there is not a 1:1 relationship in transcript availability and protein expression.

TABLE 3.1: Western blot expression levels

Knockdown Condition	RyR Expression	NCX Expression	SERCA Expression
Control	1	1	1
RyR Knockdown	0.27±0.09**	1.51±0.06***	0.69±.012*
NCX Knockdown	1.25±0.16	0.19±0.04***	2.04±0.02***

Western blot expression levels for each of the knockdown conditions. Shifts in expression levels are reported with respect to the control group. *P<0.05, **P<0.01, ***P<0.001.

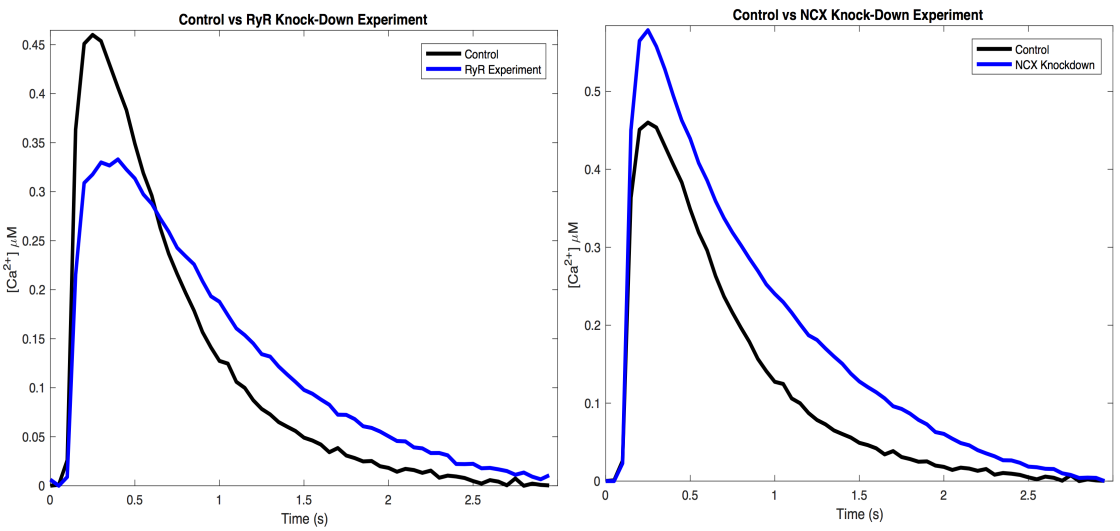

FIGURE 3.2: Average Ca^{2+} transients for RyR knockdown (A) and NCX knockdown (B) experimental group with respect to the respective control.

TABLE 3.2: Ca^{2+} Transient Functional Parameters

Experimental Condition	Amplitude (μM)	T_{peak}(s)	T_{50}(s)	T_{90}(s)
Control	0.46±0.03	0.25±0.02	0.75 ±0.02	1.55±0.09
RyR Knockdown	0.33±0.05**	0.40±0.01**	1.07±0.04***	2.25±0.11**
NCX Knockdown	0.59±0.04**	0.25±0.01	0.78±0.02	2.10±0.03**

Functional parameters of note include Ca^{2+} transient amplitude, time-to-peak (T_{peak}), time-to-50% transient decay (T_{50}), and time-to-90% decay (T_{90}). *P<0.05, **P<0.01, ***P<0.001.

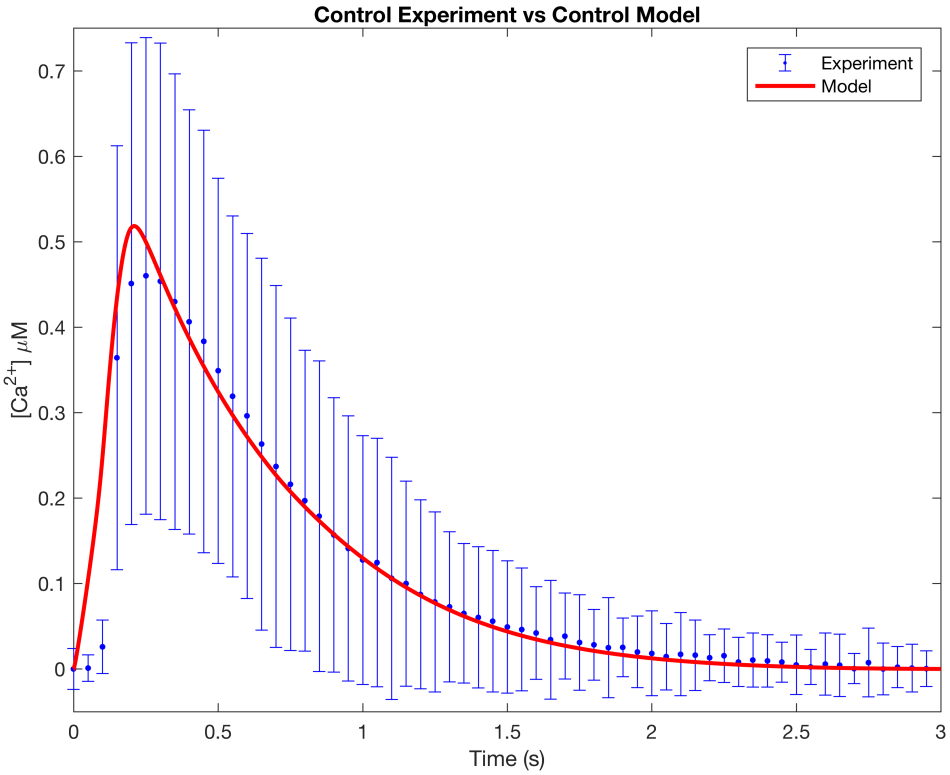

FIGURE 3.3: Fitting results for establishing a computational NRVM model for the control experiment. RyR knockdown and NCX knockdown transients were fitted to results of the control model fitting (n = 32).

TABLE 3.3: Parameter fitting results

Parameter	Units	Control	RyR KD	Fold	NCX KD	Fold
k_{NCX}	pA/(pF(μM)^4)	5.08×10^{-16}	7.37×10^{-16}	1.45×	1.52×10^{-16}	0.3×
d_{NCX}	(μM)^4	1×10^{-16} *	5.5×10^{-16}	5.5×	2×10^{-17}	0.2×
k_{RyR}	ms^{-1}	0.14	.041	0.3×	0.14	1×
$K_{m,RyR}$	μM	0.16*	0.12	0.3×	0.2	1.25×
V_{max}	μM/ms	0.32	0.26	0.8×	0.66	2.06×

Fitting results for the parameters of interest for. Fitted values are reported for the control. RyR and NCX knockdown experiment fitting results are reported. Additionally, fold factors are provided.
* Values are unchanged from [19]

3.5.2 Comparison to Computational Model

We provide the best-fit results from parameter estimates that minimize the weighted sum of squared errors

$$\min \text{SSE} = \sum_{i=1}^{N} w_i \left(x_i - \bar{x}\right)^2 \tag{3.7}$$

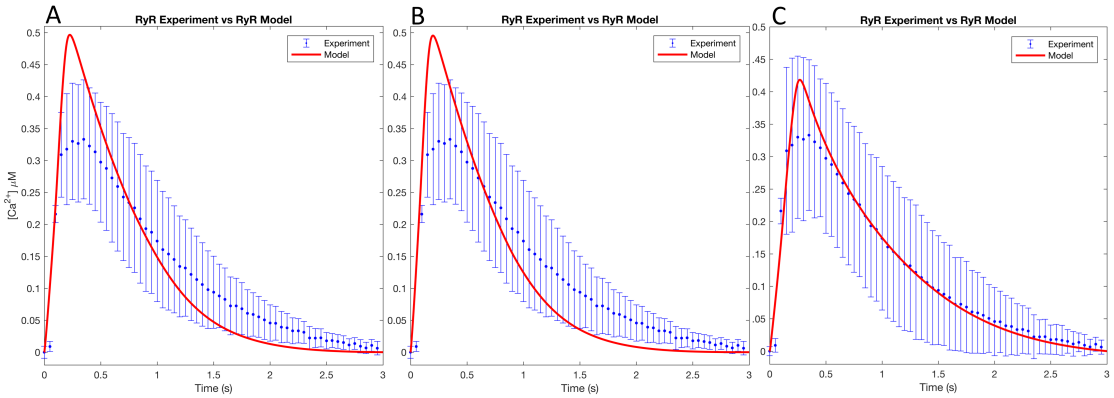

FIGURE 3.4: Fitting results using k_{RyR} as the only parameter (A) did not predict the observed transient. Including additional scaling parameters k_{NCX} and v_{max} (B) also failed to predict the experimental transient. Only when $K_{m,RyR}$ and d_{NCX} (C) were included with the previous parameter fits did we obtain a representative RyR knockdown Ca^{2+} transient (n = 21).

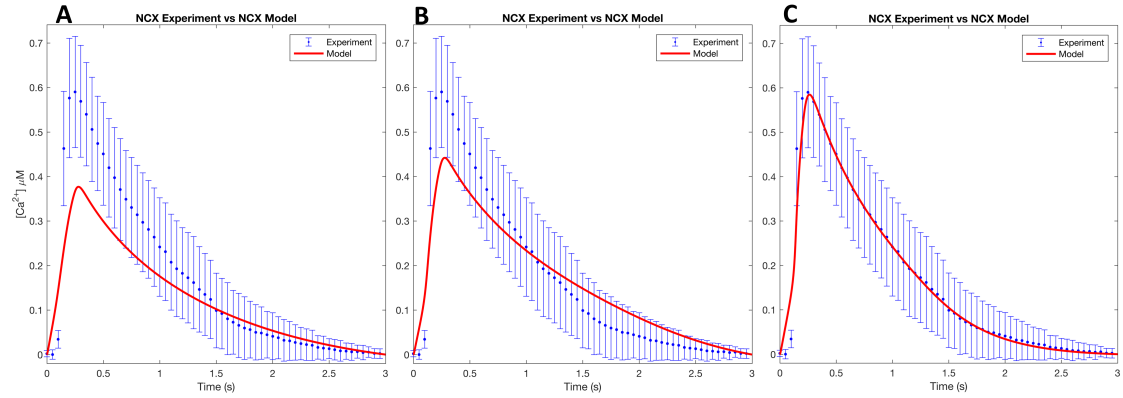

FIGURE 3.5: Fitting results using k_{NCX} as the only parameter (A) did not predict the observed transient. Including additional scaling parameters k_{RyR} and v_{max} (B) also failed to predict the experimental transient. Only when d_{NCX} and $K_{m,RyR}$ (C) were included with the previous parameter fits did we obtain a representative NCX knockdown Ca^{2+} transient (n = 27).

where the weight coefficient is

$$w_i = \frac{1}{\sigma_i^2} \tag{3.8}$$

thereby providing experimental data points with less variance, σ^2, greater weight. We perform an initial three-parameter fitting,k_{NCX}, k_{RyR}, and V_{max}, to obtain the right scaling parameters for our control experiments. Parameters used for fitting the data to the

model are kept at a minimum to keep the degrees of freedom as small as possible to avoid over-fitting. These parameters are assumed to represent protein expression levels for our control cells (Figure 3, Table 3). Only when necessary are additional parameters used, and only parameters related to the proteins in question are included.

In order to understand how Ca^{2+} transients respond to the down regulation of key regulatory proteins, we fit the predicted Ca^{2+} transients to the experimental data. For RyR knockdown, we start with only k_{RyR} as the fitting parameter, restricted within a range based on the western blot analysis for RyR expression. This limits the parameter search to only within the fractional change corresponding to the western blot data. The model fails to accurately predict experimental data (Figure 4A). Adding the scaling parameters k_{NCX} for NCX and V_{max} for SERCA also fail to accurately represent the observed measurements (Figure 4B). Only with the inclusion of the additional parameters $K_{m,RyR}$ for RyR and d_{NCX} for NCX do we have a model that is able to predict the experimental Ca^{2+} transient for NRVMs with downregulated RyR (Figure 4C , Table 3).

Similarly, we fit the NCX knockdown experimental Ca^{2+} transients using only the NCX k_{NCX} parameter. Again, we see that a single parameter fit does not predict the expected Ca^{2+} response (Figure 5A). Fitting with the inclusion of the additional scaling parameters k_{RyR} and V_{max} does not accurately predict the NCX knockdown Ca^{2+} transient (Figure 5B). Only by including the additional activity parameters $K_{m,RyR}$ for RyR and d_{NCX} for NCX we obtain an accurate prediction of the experimental NCX knockdown Ca^{2+} transient (Figure 5C, Table 3).

3.6 Discussion

We present an effort to couple protein expression from NRVMs, their respective [Ca^{2+}] transients, and computational modeling to predict changes in cytosolic Ca^{2+} fluxes in the isolated cultured NRVMs when either RyR or NCX are downregulated by siRNA. While direct comparisons to adult ventricular myocytes is not appropriate, we can compare specific mechanisms in the ECC and CICR process and interpret computational model predictions to generate mechanistic implications. Animal and human studies

have shown that protein expression levels of RyR, NCX, and SERCA are altered in diseased states [56, 57] while other experiments with NCX1 knockout mouse models observe no compensatory changes in efflux mechanisms [28]. Furthermore, murine KO models did not show any changes in expression of RyR, SERCA, or Ca^{2+} transients [58, 59]. Our experiments show that healthy NRVMs subjected to downregulation of RyR or NCX demonstrate similar trends in protein expression and Ca^{2+} response as observed in CVD [60]. While insightful, relative expression of Ca^{2+} handling proteins in CVD gives us a snapshot of the current state of the protein levels without mechanistic understanding as to how they reached those levels. Here, we try to provide some answers as to how selective downregulation affects other complimentary proteins and overall regulatory mechanisms of cytoslic [Ca^{2+}].

RyR Downregulation NRVMs with downregulated RyR have decreased Ca^{2+} amplitude, increased T_{peak}, and increase T_{50}, suggesting that less Ca^{2+} is being released due to fewer RyR channels and less SR Ca^{2+} store sequestration. Reduction of SERCA expression appears to be a response of SR Ca^{2+} content [21, 61, 62]. Studies have shown lower Ca^{2+} transients and SR store depletion are characteristics of heart failure (HF) arising from depressed SERCA expression and increased NCX expression [16, 63, 64] Increased NCX expression has been reported as compensatory mechanisms to remove cytosolic Ca^{2+} in the presence of reduced SERCA [57, 65, 66]. These differential levels of NCX and SERCA expression in response to siRNA induced RyR knockdown match our experimental observations (Figure 1).

However, the computational model suggests that accounting for RyR, NCX, and SERCA expression levels alone does not recreate the experimental Ca^{2+} transient. Additional fit parameters for RyR such as $k_{m,RyR}$ for RyR and d_{NCX} for NCX associated with protein activity are required to accurately predict the experimental observations.

The changes in these additional parameters could be explained by posttranslational modifications of RyR and NCX. $k_{m,RyR}$ is decreased in the RyR model. A decrease in $k_{m,RyR}$ implies an increase in RyR activity, possibly from changes in phosphorylation status [67]. This increase in RyR activity could be a response to compensate lower RyR

expression. Hyperphosphorylation has been observed in heart failure manifesting as decreased SR Ca^{2+}, decreased Ca^{2+} transient amplitude, and increased diastolic [Ca^{2+}] possibly from leaky RyRs [16].

The NCX parameter d_{NCX} is larger in the RyR knockdown model than in the control. An increase in d_{NCX} corresponds to an increase in NCX activity, which along with an increase in the NCX expression would modulate the cytosolic Ca^{2+} by dampening the transient amplitude [68].

NCX Downregulation NRVMs with downregulated NCX have increased Ca^{2+} amplitudes while maintaining T_{peak} and T_{50}. Increases in Ca^{2+} SR storage have been reported when NCX efflux is decreased. SERCA upregulation compensates for the lack of cytosolic Ca^{2+} extrusion by NCX. The increase in SR Ca^{2+} results in increased systolic Ca transients [69]. The upregulation of SERCA in response to NCX knockdown is observed in our experiments (Figure 1). However, once again accounting for only the protein expression levels does not adequately predict the Ca^{2+} transient (Figure 5A and 5B). However, when we include the additional NCX and RyR parameters, we do have an accurate prediction of the expected Ca^{2+} response.

As mentioned above, NCX's d_{NCX} parameter serves to modulate the Ca^{2+} transient. Decreased NCX expression does not account for the increase in Ca^{2+} amplitude. NCX needs to be less active, decreasing Ca^{2+} efflux. This can be explained by the decrease in d_{NCX}. Similarly, RyR has to compensate for an increase in SR content. We see an increase $k_{m,RyR}$ with RyR being less sensitive to Ca^{2+}, possibly to compensate for increase cytosolic [Ca^{2+}]. Decrease in RyR activity may be attributed to decreased phosphorylation due to increased luminal Ca^{2+}. Luminal SR [Ca^{2+}] is known to have a close interrelation between SR function and SR [Ca^{2+}] which affects Ca^{2+} binding, Ca^{2+} release channels, and Ca^{2+} pumps [70].

3.7 Conclusion

Ca^{2+} handling is a function of developmental stage and disease state [10, 30, 50, 51, 71]. Expression levels of NCX and SERCA in rat cardiocytes alter significantly with development. Post-natal rats express high NCX and low SERCA levels while adult rats have low NCX and high SERCA levels [72]. As expected, differences is cytosolic Ca^{2+} transient decline due to NCX and SERCA are observed in adult vs. neonate rats. In adult rats, Ca^{2+} removal by NCX accounts for 7% while SERCA removes 92%. Contrasted with neonates, NCX removes 46% and SERCA removes 50% [73]. Similarly, murine models demonstrate drastically significant integrated Ca^{2+} flux handling with adult cardiocytes removing 91% of calcium to the SR and 3% removed by NCX while neonates remove 70% to the SR and 24% extruded by NCX [74]. With calcium flux varying between developmental stages, we consider comparisons between NCX1 KO models in adult myocytes and downregulation in NRVMs. Does an 80-90% NCX1 KO, responsible for 3% of calcium removal impact calcium flux in a manner observed by 70-80% NCX downregulation in NRVMs? Answering these questions would expand our understanding of cardiac disease as a congenital or acquired condition with respect to developmental stage.

The experimental and computational results presented here show that protein expressions of key Ca^{2+} regulatory channels are interdependent. Additionally, the activity of these channels is co-regulated to compensate for changes in the Ca^{2+} transient and the cytosolic Ca^{2+} concentration. Our understanding of how Ca^{2+} cycling proteins respond to induced downregulation can help us create a response pathway in posttranslational mechanisms to generate and test new hypothesis. With Ca^{2+} involvement in so many signaling processes, experiments identifying which pathways are activated when RyR or NCX are downregulated are needed. This work is limited by the number of proteins measured and use of cell-wide calcium measurement. Measuring if any change in LTCC Ca^{2+} flux and SR content would further help validate claims that the observed changes in Ca^{2+} transient amplitude are due to increased or decreased SR Ca^{2+} storage. Proteomic and genomic studies could be used quantify how accessory proteins adapt

to induced protein inhibition and identify which pathways are actively responsible for changes in protein expression.

3.8 Disclosures

None.

Chapter 4

Actin-Myosin Force Generation in Epithelial Cells

In muscle cells, Ca^{2+} is a primary regulator of force generation and contractility as described in the previous chapters. For epithelial cells on the other hand, Ca^{2+} concentration in the cytosol is not directly controlled by pacemaker cells or neurons. Instead, actin-myosin activity is controlled via a variety of mechanical and chemical signals. Epithelial cells migrate–using actin-myosin contractility–as a response to environmental stimuli. Stimuli can be mechanical, as with substrate stiffness sensing, or chemical, as a response to a endocrine or paracrine signaling. Both endocrine and paracrine signaling involve hormones or other soluble cues. The main difference between these types of signals is distance over which they are transmitted. Endocrine signaling uses the circulatory system to deliver cues, while paracrine signals are transmitted to nearby cells [75]. Other types of cellular signaling exist. For the scope of our research, we focus only on the chemical and mechanical signaling effects on actin-myosin force generation.

Cells are able to send and receive signals intercellularly, to or from neighboring cells, or over great distances [13]. The specific response to environmental cues set off a series of a reactions that result in actin-myosin force modulation. Different pathways can affect actin-myosin contractility. Depending on the signal's appropriate response, force could

increase or decrease [76]. We limit our focus to direct physical and chemical regulation of actin-myosin activity and ignore the signals upstream of this regulation. In this way, we can provide a general understanding of force regulation that can be customized to fit specific cell types or pathways.

4.1 Migration

Cellular migration is the result of endogenous forces transmitted from the actin-myosin machinery to the substrate. Sarcomeres in epithelial cells are notably less organized than cardiac or skeletal muscle sarcomeres [4]. Furthermore, the myosin in epithelial cells is different than cardiac or skeletal muscle myosin. Non-muscle myosin is a myosin II, similar to cardiac and skeletal myosin. Non-muscle myosin II has two isoforms: non-muscle myosin IIa and non-muscle myosin IIb (NMIIa and NMIIb). NMIIa and NMIIb are functionally similar, albeit weaker, than muscle myosin [3, 77]. Nonetheless,the crossbridge cycle of muscle and non-muscle myosin is functionally the same–NMII hydrolyzes ATP to displace actin in the powerstroke state.

In vivo, epithelial cells are present in organs, vessels, nerves, and linings. They exist in a 3-dimensional environments and form complicated binding geometries with their immediate environment. Studying cellular migration and force generation in 3D environments is remarkably challenging. Cellular migration is better understood in cells cultured in 2D environments, i.e., *in vitro*[78].

Cells are cultured on gel substrates that provides a surface for cells to adhere to at the cell-substrate interface. Epithelial cells transfer their actin-myosin force by creating a physical connection between the intracellular actin-myosin contractile machinery and the immediate extracellular environment. These connections are specialized anchoring structures that physically connect cells to the substrate. Microscopic imaging shows that these adhesion structures vary from a 200 nm^2 to >4 μm^2 [79, 80].

Cultured motile cells have polarity, a phenomenon that exists *in vivo* but is not easily observable [78]. *In vitro* cells use adhesions to attach and spread onto their substrate. A

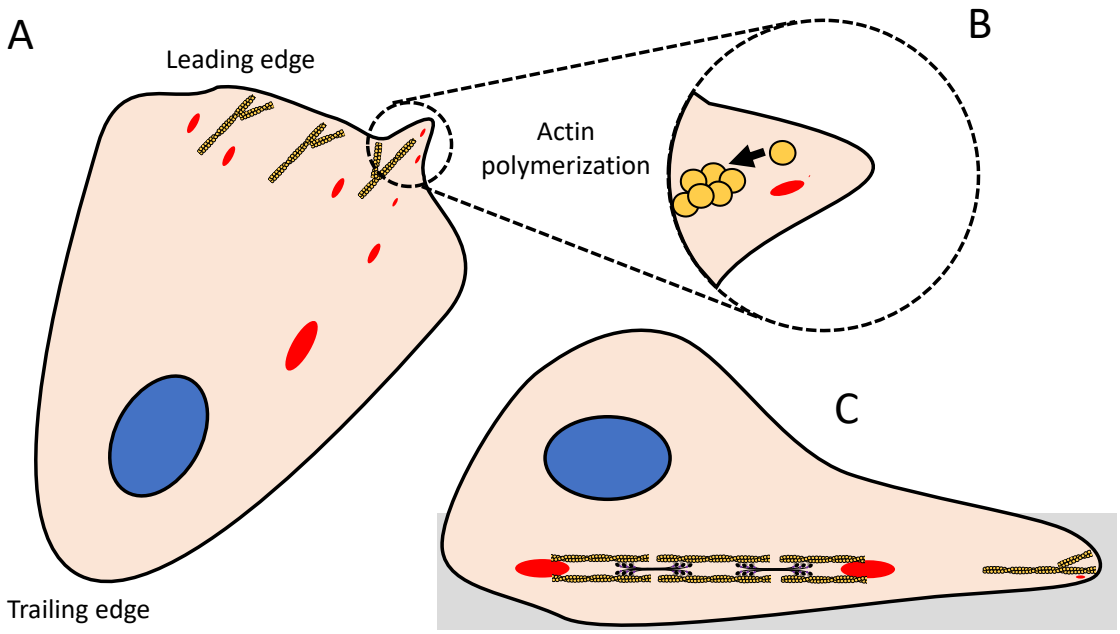

FIGURE 4.1: A) Cells cultured in 2D substrates spread and attach to the substrate by forming adhesion sites (red ovals). The leading edge is active with actin polymerization. B) Actin polymerizes and pushes against the cell membrane, causing it to protrude. At the protrusion site, small adhesions from to anchor the cell at the protrusion site. C) Profile view of a cell show that the cell is domed with a protruding leading edge.

profile view of a cultured epithelial cell reveals that the cell is domed and has a protrusion. The protrusion, or the leading edge, is the front of the cell. The opposite end of the cell is the trailing edge. Cells migrate in the direction of the leading edge by polymerizing actin at the leading edge. Actin pushes against the membrane and locally extends the leading edge. As the leading edge extends away from the cell, adhesions form to attach the cell to the substrate. Meanwhile, the trailing edge dissociates from the substrate as actin-myosin contractility "pulls" the trailing edge towards the leading edge [81].

4.2 Adhesion types

Motile cells attach to the substrate with adhesions. Adhesions are transmembrane structures that contain upwards of 200 unique proteins [82–85]. One protein, integrin, is a

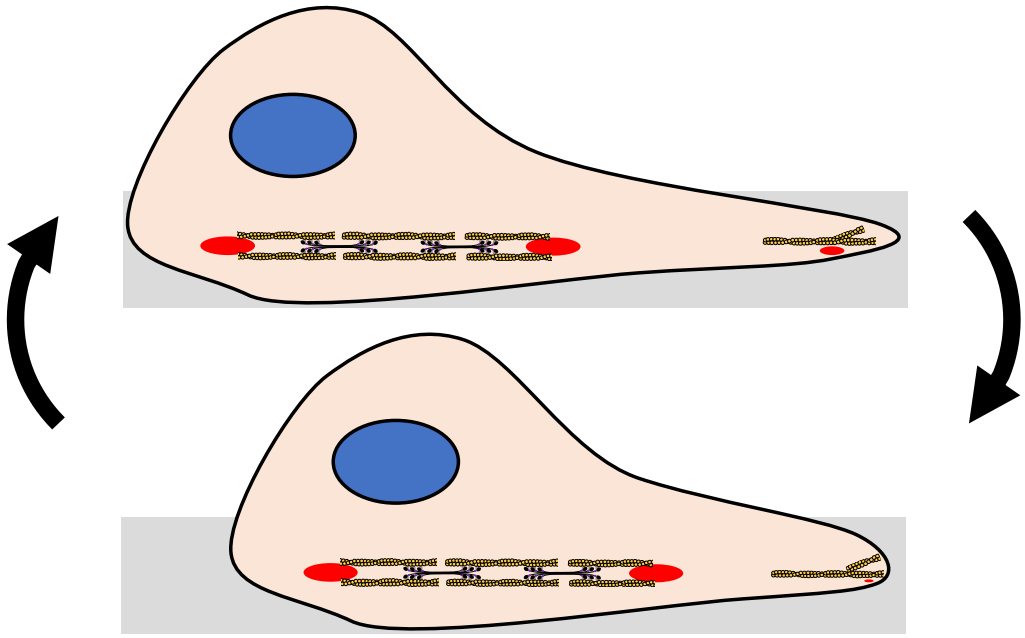

FIGURE 4.2: Cells polymerize actin at the leading edge. The leading edge protrudes and forms adhesions to anchor the newly formed protrusion to the substrate. Actin-myosin contractility "pulls" the cell towards the leading edge. The trailing edge detaches from the substrate allowing the cell to contract [78].

main protein in the adhesion plaque [82, 86]. Actin polymerization at the leading edge extends the cells membrane with integrin-mediated adhesions forming at the leading edge. Integrin is a transmembrane protein with domains that interact with intracellular components and domains that interact with extracellular components. On the extracellular side, integrins contain α and β subunits. The subunits bind to substrate ligands with integrin binding specificity. On the intracellular side, integrin binds to numerous scaffolding and signaling proteins [82–85].

Integrin adhesions assemble in a hierarchical process.

1. Integrins activate by pre-complexing with talin, a scaffolding and mechanosensitive protein [87–89]

2. Integrins bind to the substrate

3. Vinculin binds to talin

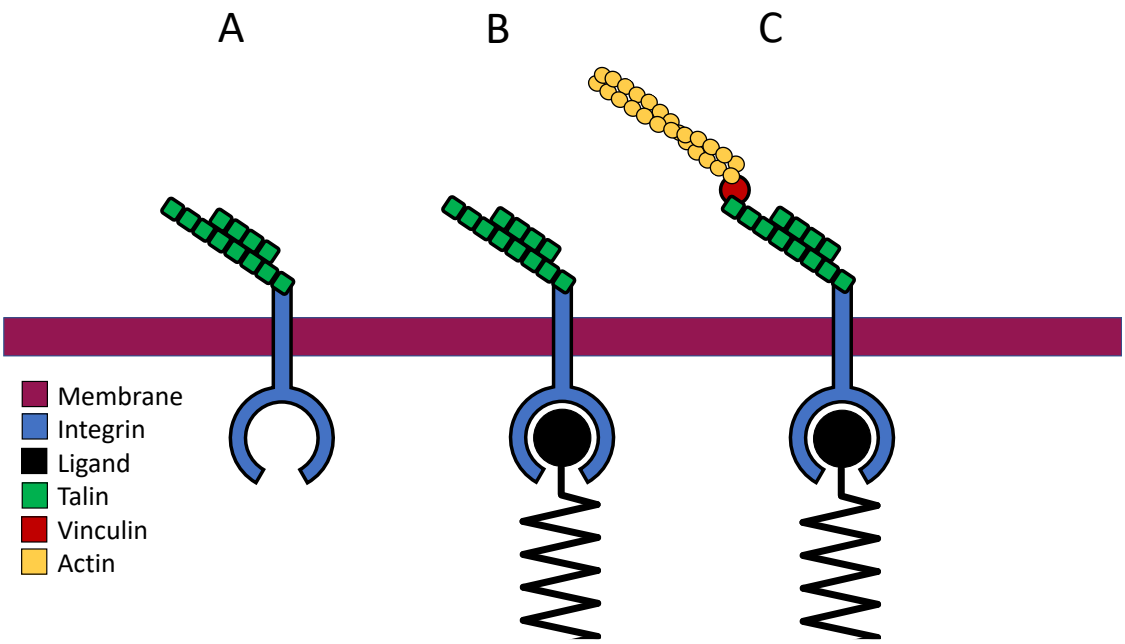

FIGURE 4.3: A) Integrins at the leading edge form adhesions. Adhesion sites are activated by pre-complexing with talin B) After activation, integrin attaches to the substrate C) Followed by the attachment of vinculin and actin-myosin

4. Actin-myosin filaments bind to talin via vinculin [90]

5. Other signaling and scaffolding proteins bind

The adhesion terminology depends on the proteins present in the adhesion. Early adhesions with integrin and talin are called nascent adhesions or early focal complexes [91–93]. These are not attached to any actin-myosin machinery and do not transfer actin-myosin stress. The adhesion matures to become a late focal complex with the addition of vinculin. Sarcomeric actin-myosin attaches to vinculin bound to talin [85, 92, 94–96]. At this point, the focal complex matures to a early focal adhesion. Early focal adhesions have the necessary components to transfer actin-myosin force by creating a physical sarcomere-talin-integrin-substrate pathway that transmits force. Early focal adhesion recruit more scaffolding and signaling proteins to form a mature focal adhesion. Of the numerous proteins identified in the adhesome we focus on integrin, talin, actin, and myosin.

4.3 Substrate Stiffness

Migrating cells need a physical connection with their substrate. The force that an individual integrin experiences is modulated by responses to the cell's environment. Substrate stiffness is a factor in actin-myosin force generation. Cells cultured on stiff substrates generate greater forces than cells of the same type that cultured on soft substrates [97, 98]. On stiff substrates cells spread more, develop focal adhesion clusters, and polarize more rapidly than cells cultured on soft substrates [99]. Substrate stiffness affects stem-cell differentiation and scar tissue formation [100–103]. Tissue stiffness range from soft (lung tissue) to hard (bone). Table 4.1 has some representative tissue stiffness values.

TABLE 4.1: Tissue stiffness values

Tissue	**Stiffness**	**Source**
Lung	0.84-1.96 kPa	[104–106]
Brain	1-3 kPa	[107–109]
Pancreas	1.1-2.9 kPa	[110–112]
Adipose	1.6-5.5 kPa	[113, 114]
Kidney	4-8 kPa	[115]
Cardiac muscle	5-50 kPa	[116, 117]
Skeletal muscle	5-170 kPa	[118–121]
Spleen	15-20 kPa	[122–124]
Bladder	20-100 kPa	[125]
Skin	60-850 kPa	[126–128]
Bone	1.28-20.7 GPa	[129, 130]

Stiffness values vary depending on the tissue.

Not only do cells generate greater forces on stiff substrates, they also become more migratory and even seek out stiffer substrates. Durotactic cells migrate with the stiffness gradient. Experiments have shown that cells cultured on substrates with varying stiffness values migrate towards the stiffer substrates in a process called durotaxis [131]. Mechanical cues, like substrate stiffness, are significant contributors to force production and motility and are a necessary component when studying cellular forces.

Chapter 5

Modeling the Effects of Chemical Signaling on Actin-Myosin Force Generation

Esteban Vazquez-Hidalgo[1]

in collaboration with

Tae-Hyung Kim[2,3]

Amy C. Rowat[2,4,5]

[1]Computational Science Research Center, San Diego State University, San Diego, California, USA
[2]Department of Integrative Biology and Physiology,
[3]Cousins Center for Psychoneuroimmunology, Semel Institute for Neuroscience and Human Behavior,
[4]Department of Bioengineering,
[5]UCLA Jonsson Comprehensive Cancer Center,
University of California, Los Angeles, California, USA

Funding information: National Science Foundation BMMB-1763132

Article preprint found at: https://doi.org/10.1101/777755

5.1 Chemical Signaling

Motile cells modulate their force as a response to not only mechanical cues, but to other cues as well, such as soluble cues [132]. For example, in MCF10A (non-tumorigenic), MDA-MB-231 (human breast cancer), and MDA-MB-231^{HM} (highly metastatic variant) cell lines, activation of β-adrenergic receptor (βAR) signaling by soluble cues resulted in increased cellular traction force and increased invasiveness [132, 133]. The increase in migration and force generation is attributed to increased actin-myosin contractility. Chemical signals that increase actin-myosin contractility do so by regulating myosin's availability to work by adding (activating) or removing (deactivating) a phosphate group to myosin light chain 2 (MLC2) located on myosin's neck domain. βAR signaling increases MLC2 phophorylation (ppMLC2). Adding a phosphorylation to MLC2 (ppMLC2) changes the conformational shape of myosin. Unphosphorylated myosin is "tangled" with itself. The heavy chains are not available to interact with other myosin tails. Phosphorylated myosin has tails that are free to interact with other myosin tails. Note that phosphorylation of MLC2 does not increase the total number of myosin. Instead, it changes then the number of myosin that are available to work out of the entire myosin population. This means that it shifts the ratios of available motors to total motors. This mechanism of regulating myosin activity is different than cardiac contractility regulation by calcium signaling. To better understand the effects of ppMLC2 on cellular force, we use experimental results of βAR activation by isoproterenol (Iso), a non-selective βAR agonist. We use computational modeling to gain mechanistic insights into how chemical signaling by βAR activation, but not restricted to βAR, affects the mechanisms of actin-myosin force generation.

5.2 Computational Model

We modify the 4-state crossbridge cycle to include MLC2 phosphorylation and ppMLC2 dephosphorylation. Each state in the crossbridge cycle has a transition rate from the current state, i, to the next state, j and follows the notation k_{ij}. The forward transition rates

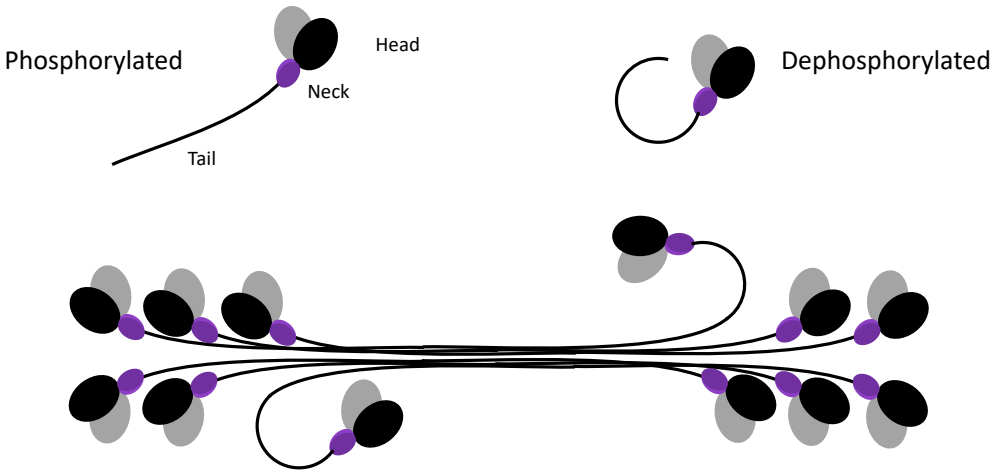

FIGURE 5.1: Dephosphoryalated myosin cannot interact with other myosin to form thick filaments. In thick filaments, myosin dephosphorylation prevents myosin from interacting with actin.

are k_{12}, k_{23}, k_{34}, k_{41}, k_{215}, where k_{215} represents the dephosphorylation of ppMLC2. This introduces a new state, state 15 that represents dephosphorylated NMII. ATP hydrolysis is reversible and is represented by the reverse transition rate k_{32}. MLC2 dephosphorylation is also reversible and is represented by the reverse transition rate k_{152} (Figure 5.2). We simulated the effect of ppMLC2 on actin-myosin generated forces with a stochastic model of the crossbridge cycle (Figure 5.3).

Transition rates for k_{215} and k_{152} are derived from western blot ppMLC2:MLC2 ratios.

$$\frac{k_{152}}{k_{215}} = \frac{ppMLC2}{MLC2} \tag{5.1}$$

Transition rates for myosin bound to actin are modified by strain the motor stalks due to the forces acting on the stalk from other attached myosin [134]. The effect of strain on the transition rates are modeled as

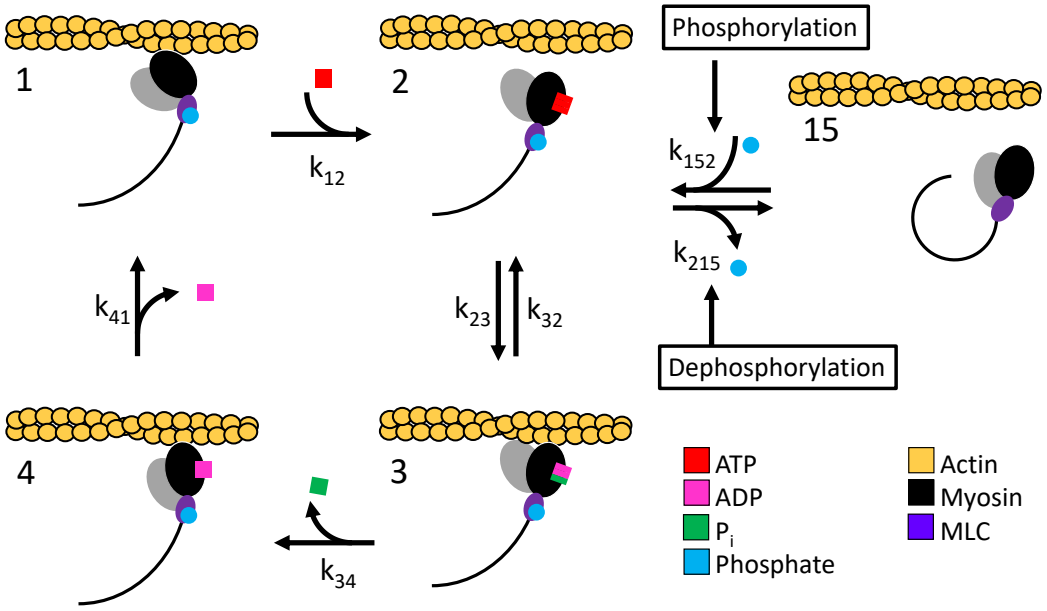

FIGURE 5.2: Modified crossbridge cycle with 5 states. The classic crossbridge model (states 1-4) with transition rates k_{12}, k_{23}, k_{34}, k_{41}, and k_{215}. The model includes state 15 to represent unphosphorylated MLC2. Motors enter state 15 from the detached state 2. Phosphorylation and ATP hydrolysis are reversible reactions. Our model includes reversible rates k_{32} and k_{152}.

$$ks_{12} = k_{12} \exp\left(\frac{\frac{1}{2}k_m\epsilon^2}{k_BT}\right) \tag{5.2}$$

and

$$ks_{34} = k_{34} \exp\left(\frac{k_m\epsilon\delta}{k_BT}\right) \tag{5.3}$$

where k_m is the stiffness in the motor stalk, ϵ is the strain in the stalk, k_B is the Boltzmann constant, T is the absolute temperature, and δ is the characteristic bond length of the actin-myosin bond. The state change of each motor is updated independently. We calculate the probability that a motor will change states from the current state to the next state by

$$P_{ij}\left(t < \Delta t\right) = 1 - \exp\left(k_{ij}\Delta t\right) \tag{5.4}$$

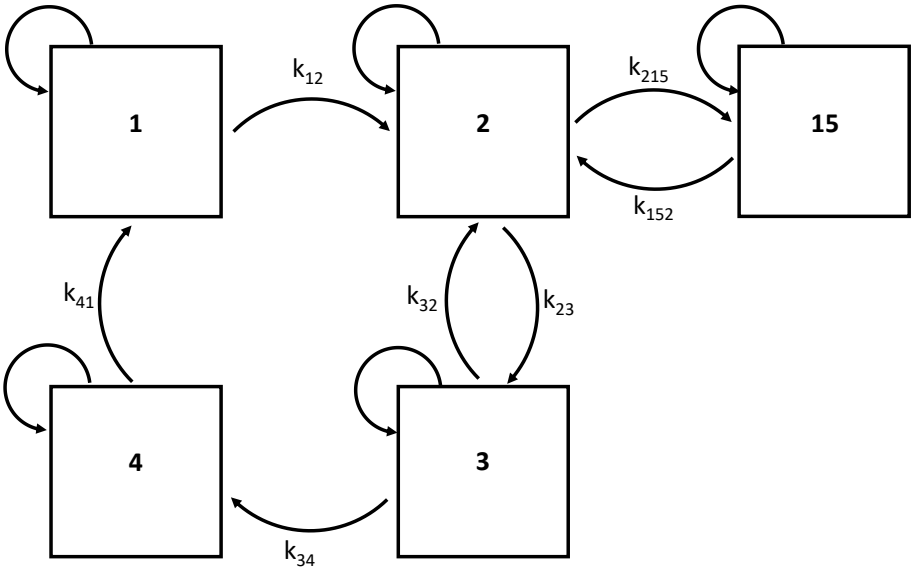

FIGURE 5.3: 5-state rate diagram for the myosin crossbridge cycle. Myosin in states with only forward rates can transition to the next state or stay at the current state. Myosin in states with forward and reverse rates can transition to the next state, the previous state, or stay at the current state.

for rates not modified by strain and

$$P_{ij}\left(t < \Delta t\right) = 1 - \exp\left(ks_{ij}\Delta t\right) \tag{5.5}$$

for states modified by strain. The forces generated by myosin on actin are

$$F_{act}(t) = \left(k_m y\left(N_1 + N_4\right)\right) - \left(\sum_i^N k_m \epsilon_i\right) \tag{5.6}$$

where N_1 and N_4 is the number of motors in states 1 and 4, respectively, and y is the motor step size. the first term represents the force that is actively generated by the motors in state 4. The second term represents the passive force from the strain in the motor stalks of all motors. Motors that are not attached do not contribute the the stain experienced by the current motor.

The myosin-generated force on actin is transferred to the integrin. The actin-myosin contraction pulls against the substrate. The displacement, x, is given by the solution of

$$F_{act} - k_{spring}x = \gamma \frac{dx}{dt} \tag{5.7}$$

where k_{spring} is the effective spring constant of the substrate and the integrin protein and γ is the drag on the actin-myosin filament.

The integrin catch-slip bond dissociation rate k_{cs} is modeled by

$$k_{cs} = k^0_{catch} \exp\left(\frac{-f\varepsilon}{k_B T}\right) + k^0_{slip} \exp\left(\frac{f\varepsilon}{k_B T}\right) \tag{5.8}$$

where k_{catch} represents the catch regime, k_{slip} is the slip regime, and ε is the length scale for binding/unbinding [135]. The force exerted on the integrin is

$$F_i(t) = k_{spring}x_i(t) \tag{5.9}$$

Within a certain force range, integrin bond lifetimes increase, however, the bond will revert to a slip bond if the force exceeds the range. Integrins that break their bond with the substrate have a probability of reattaching

$$P_{attach} = \exp(k_{att}(t)) \tag{5.10}$$

Traction stress at time (t) is calculated as the net force from all the actin-myosin filaments attached to an integrin

$$F_{TF} = \sum F_i H_i \begin{cases} H_i = 1 \text{ if physically linked} \\ H_i = 0 \text{ if not physically linked} \end{cases} \tag{5.11}$$

5.3 Results

To gain mechanistic insight into how stress hormones regulate endogenous force, we used our computational model to predict cellular traction forces. Focal adhesions were

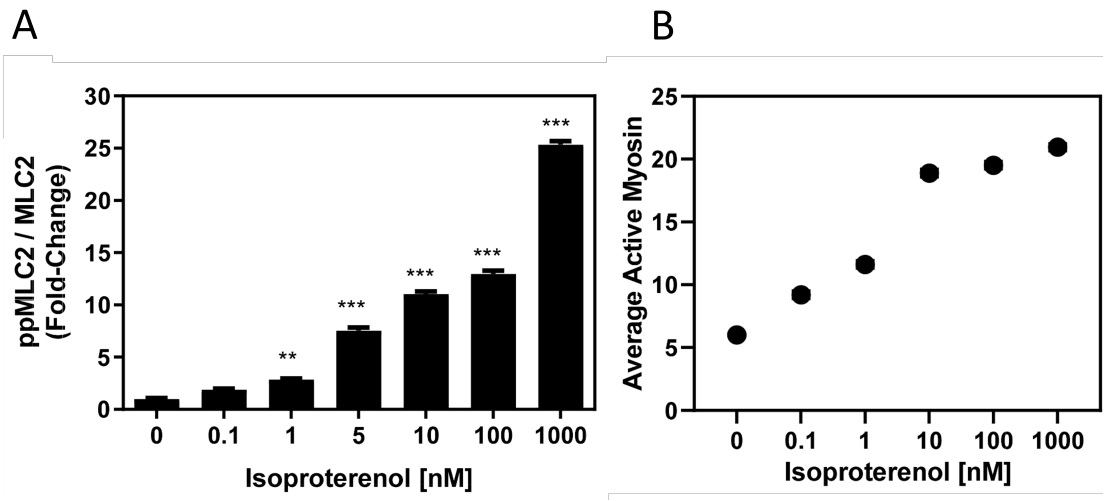

FIGURE 5.4: A) Western blots showing increase in phosphorylated motors increase with [Iso]. B) Models predictions of average number of active motors agrees with western blots [133]

modeled as actin-myosin filaments ($\sim 120/\mu m^2$) [136–138] tugging on their respective substrate bound integrins by the action of myosin motors (~ 32/actin-myosin filament) [139]. We modeled individual actin-myosin filament interactions and integrin dynamics using a stochastic Monte Carlo approach [140].

Individual motor activity was a function of its phosphorylation state, ATP binding and hydrolysis rates, as well as the pushing or pulling force acting on each motor. We used the experimentally determined ratio of ppMLC2 to total MLC2 as a model input to capture MLC2 phosphorylation/dephosphorylation rates. We estimated the force in individual actin stress fibers over time as they bind, tug, and unbind from surface bound integrins. We also determined the net traction force per unit area generated within focal adhesions over time. Increasing isoproterenol concentration from 0 to 1000 nM resulted in a 4-fold increase in the number of active myosin motors (Figure 5.4A). Our model demonstrates that the number of active motors agrees with western blot data (Figure 5.4B). Experiments with isoproterenol concentrations > 10 nM demonstrated a $\sim$2-fold increase in the predicted traction force per unit area (Figure 5.5A). Our model predicted close quantitative agreement with the experimental traction force data (Figure 5.5B).

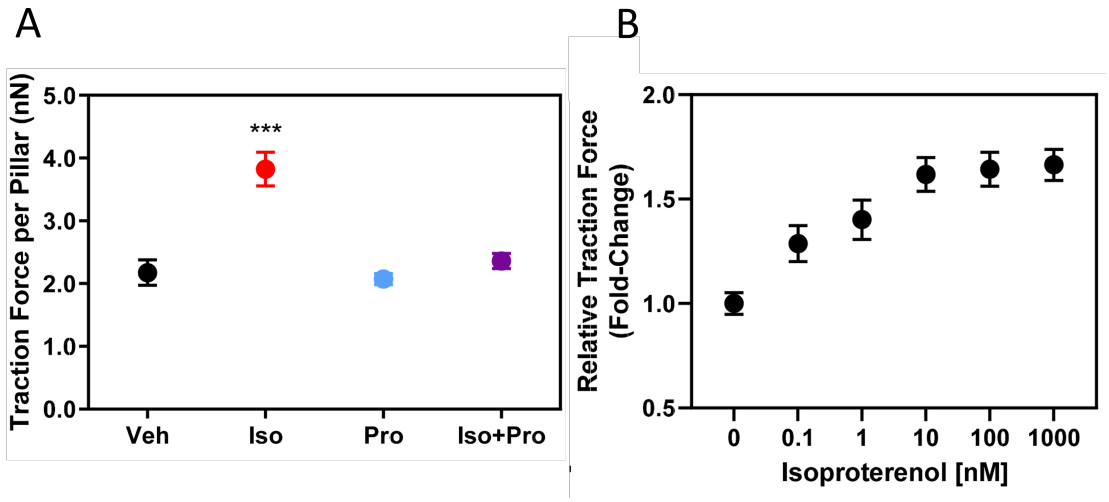

FIGURE 5.5: (A) Experiments with cells treated with isoproterenol show that the their traction forces increased 2-fold compared to the untreated control cells. (B) Simulations with increasing isoproterenol concentrations show that the traction force increase >1.5-fold for [Iso]>10 nM [133]

We further tested our model to examine how this mechanism of cellular force generation compares with the cellular response to matrix stiffness, which is established to increase cellular traction forces [97, 98]. We used the same model to predict traction forces with increasing substrate stiffness by increasing the value of effective k_{spring} in the model. We observed that with increasing substrate stiffness, the model predicts increased traction force while the number of activated motors remains relatively unchanged (Figure 5.6A), as opposed to MLC2 phosphorylation, which does increase the number of active motors (Figure 5.6B). The results obtained from our minimal model sufficiently capture experimental observations of βAR activation on cellular force generation, indicating that we are capturing the predominant mechanisms of traction force generation. Moreover, our observations are consistent with previous models of cellular traction force generation with increasing substrate stiffness [141]. Taken together, these data from both computational modeling and experiments substantiate that βAR activation increases cellular force generation by increasing the number of active motors per actin-myosin filament and suggest that cells may tune force production through

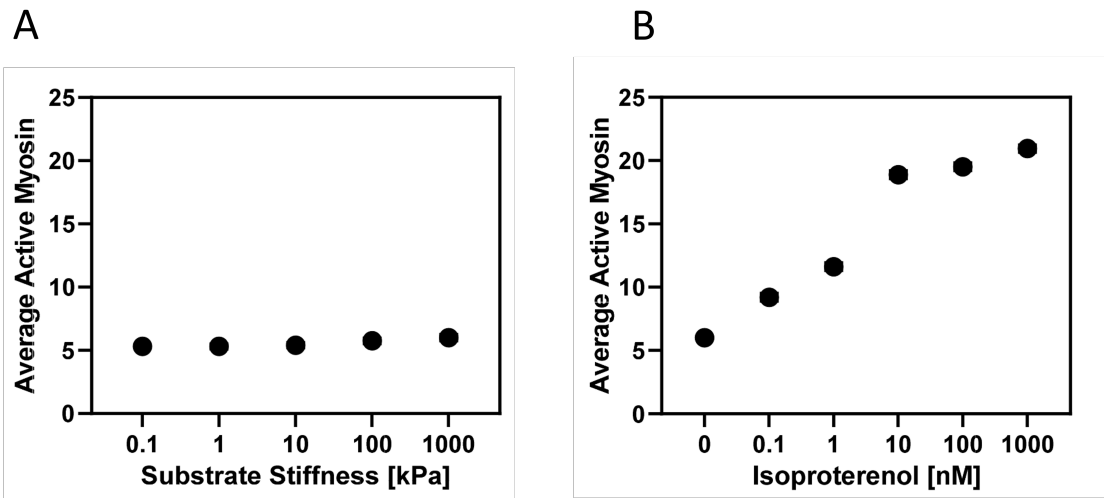

FIGURE 5.6: A) Substrate stiffness does not affect the number of active motors. B) MLC2 phosphorylation increases with [Iso]. Motors increase ∼4-fold [133].

distinctly separate yet complementary mechanisms for soluble versus mechanical cues.

Chapter 6

Modeling the Effects of Chemomechanical Signaling on Actin-Myosin Force Generation

Esteban Vazquez-Hidalgo[1]

in collaboration with

Amy C. Rowat[2,3,4]

[1]Computational Science Research Center, San Diego State University, San Diego, California, USA
[2]Department of Integrative Biology and Physiology,
[3]Department of Bioengineering,
[4]UCLA Jonsson Comprehensive Cancer Center,
University of California, Los Angeles, California, USA

Funding information: National Science Foundation BMMB-1763132

Article to be submitted to Fronteirs in Physics

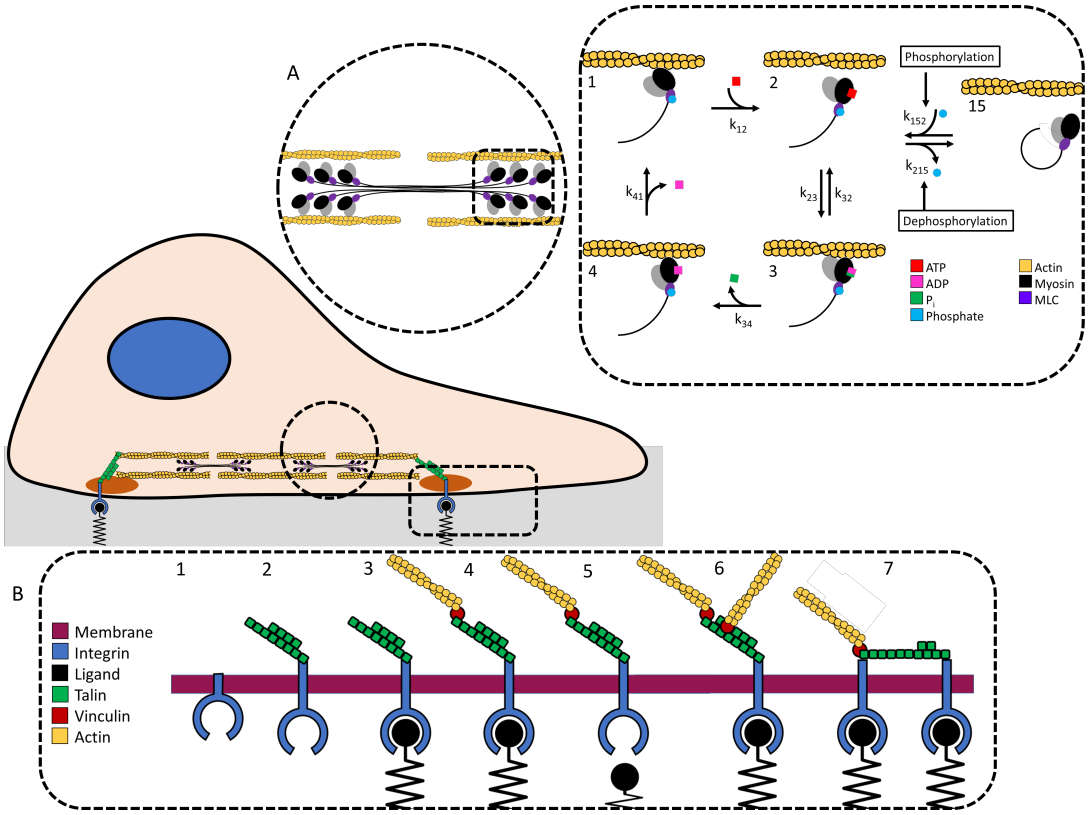

FIGURE 6.1: A) The force in our model is generated by myosin. We use use a stochastic model of the crossbridge cycle. The force generated by actin-myosin filaments. Force is transmitted to the integrins attached to the adhesion plaque. B) Integrin dynamics: 1) Deactivated integrin. 2) Integrin activates when talin binds to integrins intracellular domain. 3) This activates the extracellular domain and allows it to bind to substrate ligands. 4) Once attached to the substrate, vinculin and actin-myosin filaments attach to talin. The force is transmitted to integrin. (5) If the force is too great, the integrin-substrate bond will break. If the applied force does not break the integrin-substrate bond it is possible for talin to (6) recruit additional actin-myosin filaments via vinculin binding, or (7) branch to a neighboring integrin.

Having established baseline ppMLC2 phosphorylation rates that alter actin-myosin force generation, we extend our model to test how MLC2 phosphorylation and substrate stiffness together impact traction force (Figure 6.1). Cellular traction forces that are dependent on actin-myosin activity are necessary for numerous developmental and physiological processes [142]. Traction forces also lead to undesired pathological states such as cancer metastasis [143–145]. Metastatic cancer cells generate larger traction forces,

are more motile, and more invasive relative to their non-metastatic counterparts [144]. As traction force emerges as a promising cancer biomarker [146] the need to understand force generation in response to chemical and mechanical cues needs further investigation. Here, with the help of computational physics based models we aim to understand how much force a cell can really generate and what are the factors that limit this force. We are interested in the effects of 4 key components in traction force generation: number of active myosin motors, substrate stiffness, cell substrate adhesion dynamics, and mechanical reinforcement at adhesion complex.

The number of active motors can be controlled by biochemical signals that activate MLC phosphorylation. Number of active motors has been shown to alter force-velocity relationship [77, 147–149]. While force generation is myosin dependent, force magnitude depends on other factors. Substrate stiffness has been shown to be an important parameter in cellular force generation. Stiffer substrates increase traction force [94, 100, 149–151]. Substrate stiffness also regulates the degree of cell-substrate adhesion and the size of the adhesion complex [152, 153]. Cells anchor to the substrate with adhesions ranging from 200 nm^2 to >4 μm^2 [79, 80]. The size of the adhesion depends on the makeup of the adhesion plaque. Adhesions are composed of protein plaques that have transmembrane components that interact with intercellular and extracellular components. Adhesion assembly is a hierarchical process [84]. Adhesion proteins are added as the plaque grows. The adhesome is variable between cell types but is highly complex and organized [82–84]. Regardless of the cell type, adhesion plaques physically connect the intracellular force-generating actin-myosin machinery to the cell's substrate. This mechanical pathway allows cells to transfer the endogenous force to the substrate as traction force [154]. Of the proteins in the adhesion complex, integrins transmit endogenous force to the substrate [86, 155–158]. Integrins span the membrane with an internal component where actin-myosin can attach via talin/vinculin and an external component that binds to substrate ligands [159–163]. Integrins are essential in force transmission as integrins have a force-dependent dissociation rate. As force increases, so does the probability that the integrin-substrate bond will rupture. Actin-myosin forces

generated by the cell are transmitted as traction forces to the substrate via actin-myosin-integrin-substrate bonds. We show the maximum force an actin-myosin contractile unit can generate and sustain without slipping (stall force) increases with actin-myosin activity and substrate stiffness. We also show that this max force is rarely achieved in contracting epithelial cells as the integrin bonds coupling actin-myosin to the substrate break at lower forces. Bond lifetimes for both slip and catch-slip integrins decrease with increasing actin-myosin activity and substrate stiffness. For these results, we focus on integrins attached to a single actin-myosin filament. Next, we probe how talin-mediated dynamics alter cellular force generation. Force dependent unraveling of talin can add additional actin-myosin filaments (recruitment) or cause talin to bind additional integrins (branching). Traction stress for catch-slip bonds with and without recruitment and branching exhibit biphasic or sigmoidal behavior that is dependent on the combination of myosin activity and substrate stiffness. Adhesion size, defined by the number of integrins actively contributing to traction stress, decreases with actin-myosin activity and substrate stiffness, however this is not a limiting factor in traction stress generation.

6.1 Computational Model

To understand how much force a cell can generate, we assume that traction stress, force per unit area, are generated by actin-myosin filaments attached to integrin receptors [164–166].We simulate a predefined adhesion plaque with a density of 100 integrins per 1 μm^2 [93, 167]. The adhesion plaque is a 10x10 grid representing 100 integrins pre-complexed with talin and vinculin [96]. Talin is necessary to activate integrin [168–171]. Talin binds to integrins cytosolic domain to activate integrin [172]. Furthermore, talin's force dependent unfolding is used to attach more filaments or integrins. There are 100 actin-myosin filaments that are 3 μm [173] long and contains 60 myosin motors [139, 174–176]. Filaments bind to talin via vinculin [177–179]. The forces we are investigating originate from myosin binding and pulling along the actin filaments. We use a stochastic model of the myosin crossbridge cycle [180–182] modified with non-muscle myosin

II transition rate parameters [183] to capture ATP hydrolysis, actin-myosin binding, conformational changes, and detachment (Figure 6.1A) [134, 184]. The forward transition rates are k_{12}, k_{23}, k_{34}, and k_{41} with k_{23} representing ATP hydrolysis. ATP is a reversible process and k_{23} represents the reverse reaction from state 3 to state 2. The crossbridge model consists of 4 states (state 1 through state 4) with respective transition rates from the current state, i, to the next state, j. Each motor is independently updated. State transition rates follow the form k_{ij}. Myosin dependent forces are regulated in part by the number of active myosin. We assume that only myosin with phosphorylated MLC2 can enter the crossbridge cycle and interact with the actin. Myosin that are not phosphorylated or that are dephosphorylated–phosphorylation is reversible–do not participate in the crossbridge cycle. Inactive myosin transition to state 15 from state 2 [185], modifying the 4-state cycle to a 5-state cycle [140]. Phosphorylation and dephosphorylation rates, k_{215} and k_{152} respectively, representing the transition rates from phosphorylated to dephosphorylated states. We define the ratio of phosphorylated MLC2 (ppMLC2) to total non-phosphorylated MLC2 (MLC2) as described in Eq.(5.1),

$$\frac{k_{152}}{k_{215}} = \frac{ppMLC2}{MLC2}$$

where the phosphorylation ratio is the input parameter that modifies MLC2 phosphorylation.

Transition rates where the motor is bound to actin (states 1 and 3) are modified by strain resulting from the pushing or pulling of the current motor from the other bound motors in the motor ensemble. We use Eq.(5.2)

$$ks_{12} = k_{12} \exp\left(\frac{\frac{1}{2}k_m\epsilon^2}{k_BT}\right)$$

and Eq.(5.3)

$$ks_{34} = k_{34} \exp\left(\frac{k_m\epsilon\delta}{k_BT}\right)$$

for the strain-dependent rate modifications where k_m is the stiffness in the current motor's stalk, ϵ is the strain on the motor's stalk, k_B is Boltzmann's constant, T is the

absolute temperature, and δ is the characteristic bond length of the myosin bond [77].

Each motor's state is independently updated. The probability that a motor will transition from state i to state j within the given time is Eq.(5.4)

$$P_{ij}(t < \Delta t) = 1 - \exp\left(k_{ij}\Delta t\right)$$

for transition rates that are not modified by strain and Eq.(5.5)

$$P_{ij}(t < \Delta t) = 1 - \exp\left(ks_{ij}\Delta t\right)$$

for transition rates modified by strain.

Adhesion plaques form in a hierarchical process (Figure 6.1B) [85, 92]. The first step in forming an adhesion plaque requires integrin activation. Integrin activates by complexing with talin at a rate k_{act}. Activated integrins attach to the substrate ligand at a rate k_{att}. Once attached to the substrate, actin-myosin filaments bind to talin. These dynamics are temporally regulated. Integrin activation, integrin attachment, and actin-myosin attachment occur at independent time steps. The force generated in a single actin-myosin ensemble due to myosin activity is calculated by Eq.(5.6)

$$F_{act}(t) = \left(k_m y\left(N_1 + N_4\right)\right) - \left(\sum_i^N k_m \epsilon_i\right)$$

where N_1 and N_4 are the number of motors in the ensemble in states 1 and 4 and y is the motor step size. The force in the actin-myosin filament is myosin-dependent. The first term represents the number of motors actively generating force by pulling on actin while the second term is the contribution of passive force from the strain of all actin-bound myosin in the ensemble. Motors that are not bound to actin do not contribute to the passive force. Conversion of endogenous actin-myosin force to traction force requires a physical pathway. Integrin is the mechanosensor that determines if the endogenous force is converted to traction force. The force experienced at integrin-substrate bond is dependent on the displacement from pulling on integrin by the actin-myosin filament.

We solve for the displacement with Eq.(5.7)

$$F_{act} - k_{spring}x = \gamma \frac{dx}{dt}$$

where x is the displacement, k_{spring} is the effective spring constant between substrate and integrin, and γ is the drag on the actin-myosin filament [186]. Integrin-substrate bond lifetimes have force-independent association rates and force dependent dissociation rates. Two integrin dissociation rates are reported: slip bonds and catch-slip bonds [135, 187]. Slip bond lifetimes continuously decrease with increasing force whereas catch-slip bonds have a force range that strengthens the bond and increases the bond lifetime [135, 188]. Catch-slip integrins experience an increase in bond lifetime up to an optimum applied force before reverting to a slip bond. Slip bond force-dependent dissociation rates are modeled by

$$k_{off}(f) = k_0 \exp\left(\frac{f}{F_b}\right) \tag{6.1}$$

where k_0 is the unloaded off rate, f is the force at the integrin-substrate interface, and F_b is the characteristic bond rupture force. Integrins with catch-slip dynamics are modeled by [131]

$$k_{off}(f) = \left[A \exp\left(\frac{-f\xi}{k_B T}\right) + \left(B \exp\left(\frac{f\xi}{k_B T}\right) + C \exp\left(\frac{-f\xi}{k_B T}\right)\right)^{-1}\right]^{-1} \tag{6.2}$$

where A, B, and C are constants, ξ is the unbinding length, and f is the load on the integrin. We use the dissociate rate, k_{off}, to calculate the dissociation probability

$$P_{off} = 1 - \exp(-k_{off}(f)\Delta t) \tag{6.3}$$

Simulation for slip and catch-slip bond dynamics require talin-mediated integrin activation before integrin-substrate binding. The probability of integrin activating is

$$P_{activate} = 1 - \exp(-k_{act}\Delta t) \tag{6.4}$$

where k_{act} is the integrin activation rate. Activated and attached integrins are available for actin-myosin filament binding. The probability for an integrin to bind to the substrate is described in Eq.(5.10)

$$P_{attatch}(t < \Delta t) = 1 - \exp(-k_{att}\Delta t)$$

where k_{att} it the rate at which activated integrin attach to the substrate. Activated and substrate-bound integrins are available for actin-myosin binding. The probability that an actin-myosin filament attaches to integrin is

$$P_{sfatt}(t < \Delta t) = 1 - \exp(-k_{sfatt}\Delta t) \tag{6.5}$$

where k_{sfatt} is the actin-myosin binding rate. We track integrin activation, integrin-substrate binding, actin-myosin filament attachment, and talin-mediated actin-myosin filament recruitment (more than one actin-myosin filament per integrin) or talin-integrin branching (more than one integrin per actin-myosin filament). We use talin-mediated dynamics to create a more realistic model. A complete physical pathway from actin-myosin to substrate enables transmission of endogenous forces to the cell's immediate surrounding via integrin-substrate attachment. The force on individual integrin-substrate bonds by the actin-myosin filament activity is calculated by Eq.(5.9)

$$F_i(t) = k_{spring}x_i(t)$$

where k_{spring} is the spring constant of the substrate and x_i is the displacement of the filament. In the case that the force does not rupture the integrin-substrate bond, the force is successfully transmitted to the substrate. Non-ruptured bonds allow myosin to continue to increase the displacement of the filament, increasing the forces experienced at the integrin-substrate bond. As force increases linearly with displacement there will be a max force at which the bond will break, ending its attachment period. Individual integrins experience force generated by actin-myosin. We use the individual forces at

the integrins to determine the traction stress, or the collective force of all filaments actively generating and transmitting force. Traction stress is sensitive to bond lifetimes of individual integrins in the adhesion plaque. Traction stress is determined by Eq.(5.11)

$$F_{TF} = \sum F_i H_i \begin{cases} H_i = 1 \text{ if physically linked} \\ H_i = 0 \text{ if not physically linked} \end{cases}$$

Similarly, adhesion size, which we define as only those integrins bound to the substrate actively transmitting actin-myosin force, is

$$FA(t) = \sum H_i(t) \begin{cases} H_i = 1 \text{ if physically linked} \\ H_i = 0 \text{ if not physically linked} \end{cases} \tag{6.6}$$

For simulations where talin is permitted to recruit filaments or branch to integrins, we calculate the probability of talin unfolding and allow up to 8 actin filaments to attach to a single integrin-talin complex or branching to 2 integrins. Talin unfolding probabilities are

$$P_{rec} = 1 - \exp\left(-k_{rec}\right) \tag{6.7}$$

and

$$P_{branch} = 1 - \exp\left(-k_{branch}\right) \tag{6.8}$$

with k_{rec} representing the talin unfolding rate for recruiting filaments and k_{branch} representing the talin unfolding rate for branching. We represent the adhesion plaque and the proteins required to establish a physical link from actin-myosin to substrate with matrices that are $n \times m$ where n is the number of integrins/filaments/attachment status, etc., and m is time in ms. Each matrix tracks motor state changes, integrin activation, integrin attachment, filament displacement, force, recruitment, and branching. For talin recruiting filaments, the displacement of the filaments is calculated by

$$\sum_{i=1}^{R} F_{act} - k_{spring}x = \gamma \frac{dt}{dx} \tag{6.9}$$

where R is the number of recruited stress fibers. The force on the integrin is calculated using Eq.5.9. Similarly the displacement of branched filaments attached to multiple integrins is calculated by

$$F_{act} - bk_{spring}x = \gamma \frac{dx}{dt} \tag{6.10}$$

where b is the number of branches. The force on the integrins is calculated using Eq.5.9. Single filament average bond lifetimes are calculated by determining the time intact mechanical pathways are bound to the substrate

$$\bar{\tau} = \frac{1}{n} \sum_{1}^{n} L_t \tag{6.11}$$

where n is the number of binding events and L_t is the duration in ms of the binding event.

The stall force for the actin-myosin fibers is calculated by fitting the force generated over time with

$$f = f_{stall} \left(1 - \exp\left(-\alpha t\right)\right) \tag{6.12}$$

The stall force reported is the average stall force over 100 actin-myosin filaments. When integrins bonds break in a force dependent manner, we obtain the maximum force generated by the actin-myosin filament during any attachment event. We report the average of the maximum force as

$$F_{maxavg} = \frac{1}{n} \sum_{i=1}^{n} F_{AM}(j) \tag{6.13}$$

where F_{AM} is the vector n elements long that contains the maximum force generated in all binding events of filament j. Similarly, the average non-zero force generated is

$$F_{nonzero} = \frac{1}{N} \sum F_{NZ} \tag{6.14}$$

where N is the number of filaments and F_{nz} is the non-zero average of the filament. We report the maximum traction force per μm^2 by fitting

$$F_{TF} = F_{TFmax} \left(1 - \mathrm{e}^{-\beta t}\right) \tag{6.15}$$

6.2 Results

We explore how force develops in single filaments by varying integrin bond type, number of active motors, substrate stiffness, and talin-mediated actin-myosin filament recruiting or talin branching. Furthermore, we show how these factors influence traction stress.

6.2.1 Stall Force

Stall force corresponds to the maximum force a single actin-myosin filament can generate in the absence of integrin-substrate detachment. Increasing ppMLC2 and substrate stiffness increases stall force (Figure 6.2A). An obvious factor that controls the stall force of an actin-myosin filament has to be the number of active motors generating forces. We test this by changing the number of active motors in the crossbridge cycle by increasing the ratio of MLC phosphorylation to dephosphorylation rates. Stall force are dependent on the number of motor proteins actively generating force per actin-myosin filament. Stall force increases linearly with the number of motors in force-generating states (Figure 6.3) [174]. A less obvious factor that controls the stall force of an actin-myosin filament is the stiffness of the substrate against which the actin-myosin filament is pulling. We observe that in the absence of unbinding/breaking of the actin-integrin-substrate connection, the stall force generated in a single actin-myosin filament strongly depends on the stiffness of the substrate it is pulling against. This is an interesting result, not previously considered in most cell traction force generation and migration models.

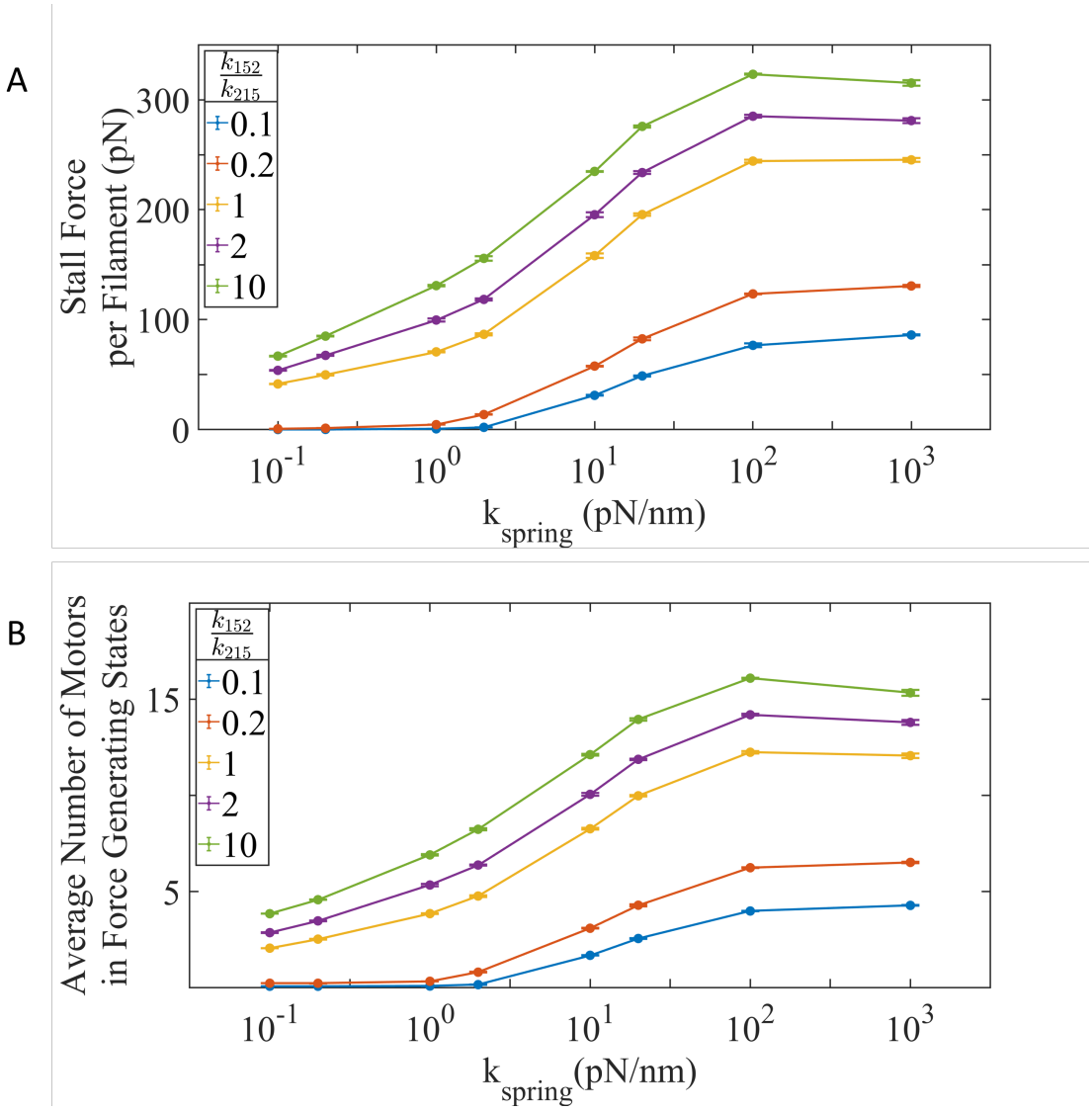

FIGURE 6.2: A) Stall force increases with ppMLC2 and substrate stiffness in integrins with ideal bond. B) The number of motors actively generating force increases with ppMLC2 and substrate stiffness, albeit via distinct mechanisms. Phosphorylation increases the number of motors available to work. Stiffness increases force which increases myosin's duty ratio. Our simulations show that approximately one quarter or less of available motors are required to generate large stall forces.

This dependence of the stall force on substrate stiffness arises because pulling against a stiffer substrate synchronizes myosin cross-bridge cycling and recruits more myosin into the actin bound, force generating states (Figure 6.2B). The results show that the

forces transmitted by individual actin-myosin filaments (and consequently the traction stress) is not limited by the stall forces of the filaments, as these stall forces are far greater than observed forces transmitted across individual actin-integrin-substrate bonds.

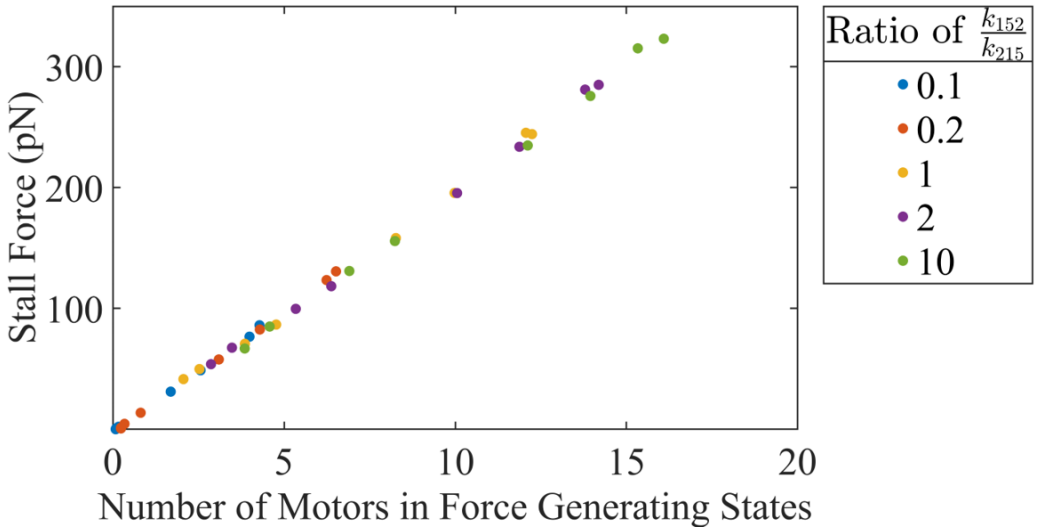

FIGURE 6.3: Stall force increases linearly with number of motors in force-generating states

6.2.2 Forces transmitted across the adhesion complex in the presence of force dependent integrin-substrate bond lifetime

Stall force shows us how much force is possible in the absence of integrin-substrate unbinding. Clearly, one would expect that a higher stall force for an actin-myosin filament would result in a higher overall traction force generated by the cell. Integrins, however, do break their attachment with the substrate in a force-dependent fashion. If we allow integrin bond to break, then the stall force in an actin-myosin filament does not limit the forces transmitted across the cell-substrate bond. Instead, bond lifetime emerges as a critical limiting factor. The bond lifetime can limit the force being transmitted from the cell to the substrate in two ways – 1) by restricting the how high forces in individual actin-integrin-substrate adhesions can ramp up to before the individual integrin-substrate bond breaks, and 2) by affecting how many actin-integrin-substrate

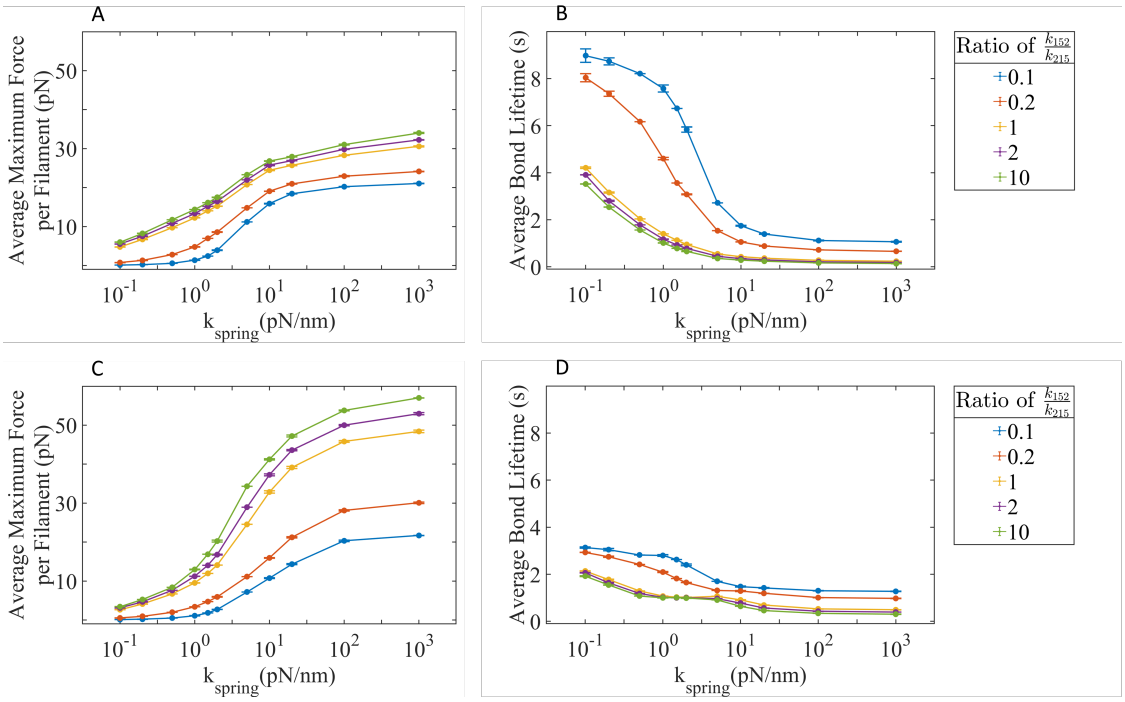

FIGURE 6.4: Maximum force transmitted is bond type dependent. Both slip bonds and catch-slip bond integrins transmit increasing forces with increased ppMLC2 and substrate stiffness with slip bonds (A) transmitting lower forces that (B) catch-slip bonds. Both slip (B) and catch-slip (D) integrins experience decreased bond lifetimes with increased ppMLC2 and substrate stiffness

adhesions are actively transmitting cellular forces to the substrate at any given instance. We test the contributions of both these mechanisms under slip as well as catch-slip integrin-substrate bind detachment kinetics. We observe that the maximum force increases with ppMLC2 and substrate stiffness in both bond types (Figure 6.4A,C). Both bond types have monotonically increasing maximum forces with catch-slip bonds generating larger forces than slip bonds. The maximum force captures the force at which the integrin-substrate bond ruptures. Slip bonds generate forces >30 pN while catch-slip bonds generate forces >50 pN which agrees with experimental observations [189, 190]. As expected, the increase in force decreases the bond lifetime in both bond types (Figure 6.4B,D). At low forces, slip bond lifetimes outlast catch-slip lifetimes. As force builds, bond lifetimes for each bond type settle to similar values under similar experimental conditions. This is due to the slip regime driving the bond lifetimes at high

forces.

6.2.3 Total traction stress transmitted by the cell with and without mechanosensitive actin-myosin fiber recruitment and branching

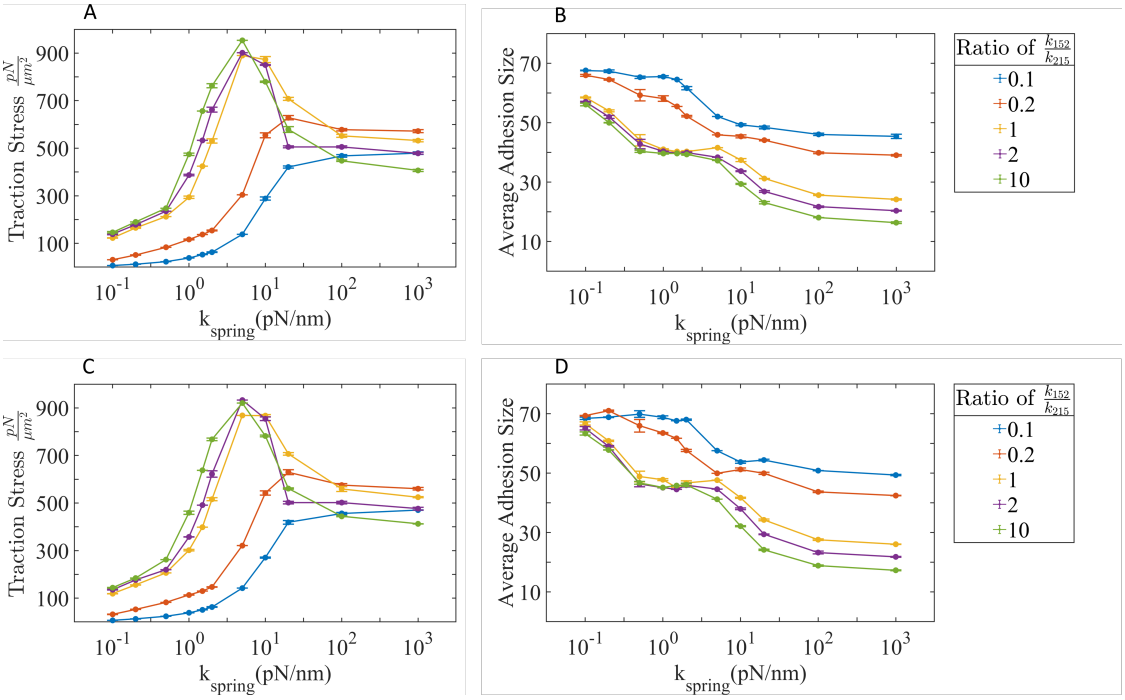

FIGURE 6.5: A,C) Traction stress without and with talin-mediated adhesion reinforcement demonstrate similar profiles. Both conditions show sigmoidal curves at low ppMLC2 and low substrates but biphasic trends at high ppMLC2 and high substrate stiffness. B,D) Adhesion sizes for both conditions decrease with increased ppMLC2 and substrate stiffness.

Traction force is the sum of the forces by all focal adhesions in a cell [191]. We report traction stress, the force generated over a unit area $1\mu m^2$. Only those actin-myosin filaments with an intact mechanical pathway contribute to traction stress. We test whether talin-mediated recruitment of actin-myosin fibers and integrin branching have any effect on traction stress. Simulations show that traction stress and adhesion size for integrins with and without talin-mediated dynamics are relatively unchanged (Figure 6.5A,C). Furthermore, adhesion size for both conditions is remarkably similar (Figure 6.5B,D). Figure 6.6 shows time series of adhesions under different stiffness and ppMLC2

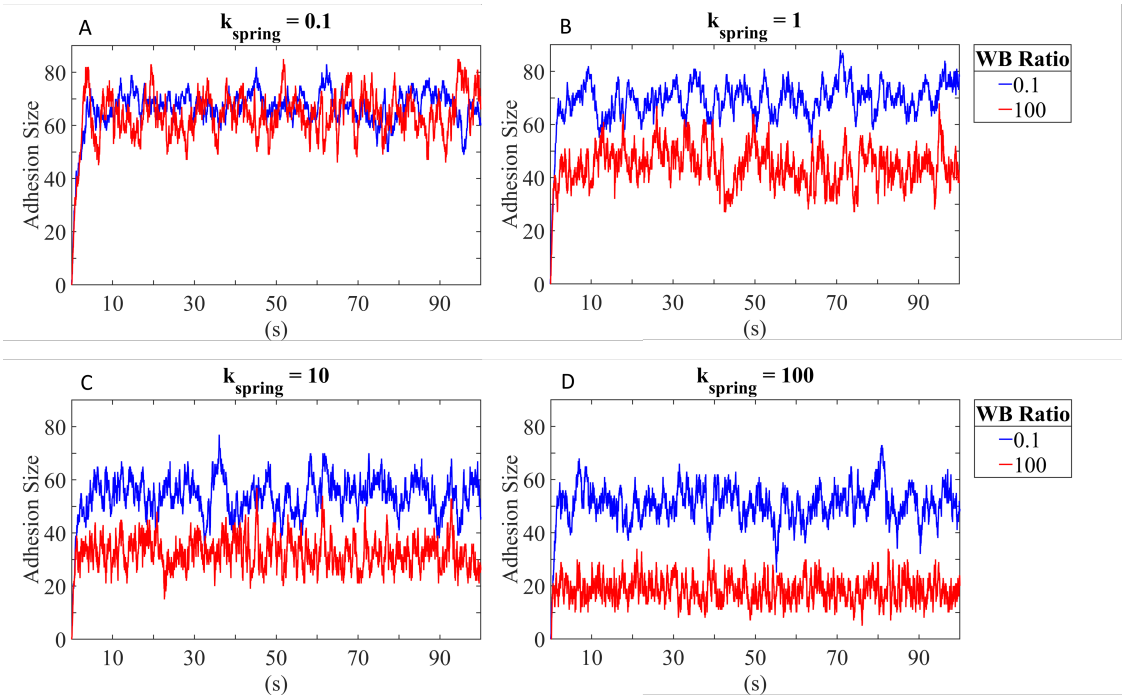

FIGURE 6.6: Samples of adhesion growth over time under varying conditions.

values. Both conditions show traction stress is nonlinear with trends are ppMLC and substrate dependent. Low ppMLC traction stresses demonstrate a sigmoidal trend while high ppMLC traction stresses are biphasic. Talin contains 4 domains that unfold with applied force as low as 2 pN [159, 160]. 3 of these domains (I, II, and IV) have vinculin binding sites and one domain (III) has an integrin binding site. Regions II-IV have force-dependent unfolding rates $< 2.5 \times 10^{-5} s^{-1}$ [159]. These unfolding rates are too restrictive and are unlikely to happen during our 100 s simulation. Region I has an unfolding rate fast enough (0.018 s^{-1} [159]) for talin-mediated actin-myosin recruitment to occur within our simulation time.

6.3 Discussion

The maximum force a single actin-myosin unit can generate is context-dependent and can be modulated by either one or more of the following conditions: integrin bond

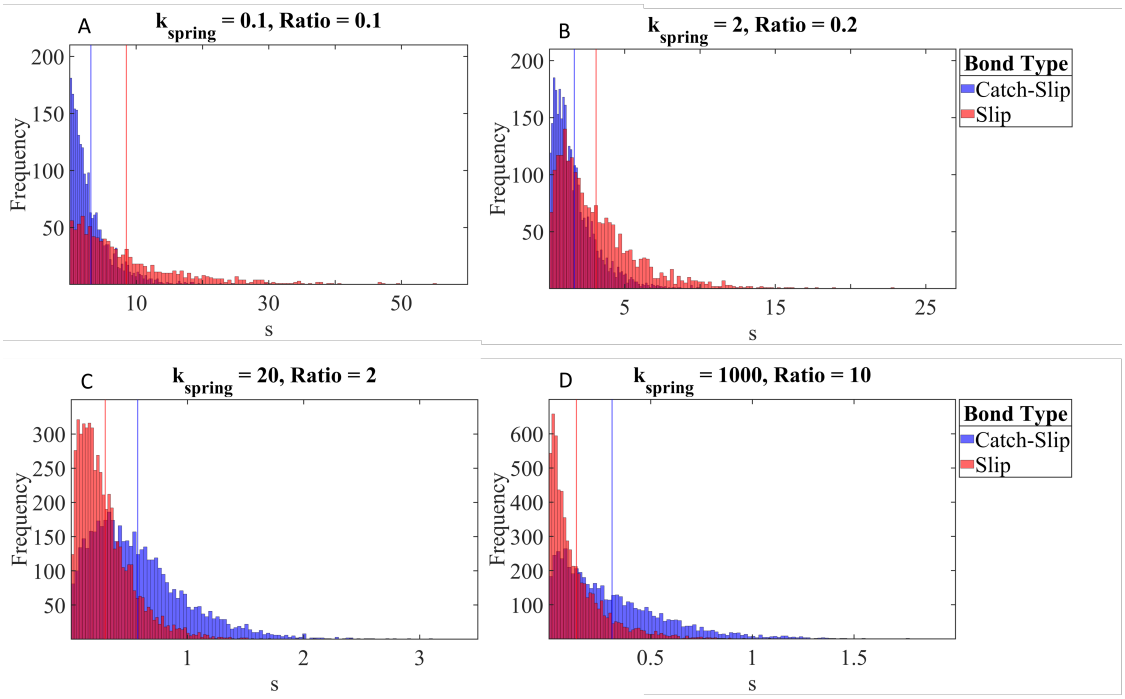

FIGURE 6.7: Average bond lifetimes for slip and catch-slip bonds are similar. We see that the lifetime distributions for slip bond have longer tails than catch-slip bonds at low ppMLC2 and low substrate stiffness. However, at high ppMLC2 and high substrate stiffness catch-slip bonds lifetime distributions have longer tails. The tails shift the average bond lifetimes. While the bond lifetimes averages may be similar, the positive skewness contributes to increased bond lifetimes.

type, ppMLC, and substrate stiffness. Traction stress, the contribution of all force generating filaments in an adhesion complex, and force per filament have drastically different profiles even though traction stress is entirely dependent on single filament forces. Forces generated by actin-myosin filaments are modulated by two independent mechanisms: the number of motors and substrate stiffness. For example, simulations with integrin bonds that do not break show that if we hold ppMLC2 ratios constant, traction force increases with substrate stiffness. Likewise, if we keep substrate stiffness constant, stall force increases with ppMLC2. Furthermore, force generation has a positive effect on myosin as myosin is mechanosensitive [192]. Myosin duty ratio shifts in a force-dependent manner [77]. The duty ratio increases with load which increases

the number of attached motors as substrate stiffness increases in a ppMLC independent mechanism. The increase in motors is not a response to stiffer substrates but a response to increased force. Stall force then is a response to both the number ppMLC2 activated motors and substrate stiffness. Our simulations with catch-slip bonds with and without talin-mediated actin-filament recruitment or integrin branching agree with experimental results showing that single integrin bonds withstand forces ranging from $<$2 pN to $>$54 pN [190], while disagreeing with other experiments that show single integrin bonds break between 10-30 pN [193, 194]. Although catch-slip bonds can withstand forces greater than the 10-30 pN range reported, slip bonds cannot. Slip bonds rupture at forces $<$30 pN (Figure 6.4A). These results do not support assumptions made in models with fixed rupture forces [151]. As forces increase, bond lifetimes decrease. Interestingly, bond lifetimes for slip bond and catch-slip bonds settle at similar bond lifetimes while having different maximum force profiles. This is likely due to distribution of the bond lifetimes. At low ppMLC2 and low substrate stiffness bond lifetimes for slip bonds skew farther right while at high ppMLC2 and substrate stiffness catch-slip distributions skew farther right (Figure 6.7). It is this extended positive skewness that increases the maximum force for catch-slip bonds at high ppMLC2 and high substrate stiffness. Bond lifetimes impact adhesion size. Increasing the force in individual actin-myosin filaments decreases the adhesion lifetime and consequently adhesion size. Our definition of an adhesion, only those integrins actively contributing to traction force, is likely too narrow as it disregards scaffolding proteins that contribute to the composition of the adhesion. Nonetheless, our simulations show similar number of force transmitting integrins bound to substrate ligands agree with experiments showing that adhesions measuring up to 2 μm^2 have 52 $\pm$ 42 integrin-bound ligands per adhesion [91].

However, adhesion size is a poor predictor for traction stress, contrary to reports that use adhesions to predict traction force [80] there is a large range of traction stress at adhesions containing 50 bound integrins (Figure 6.8A). We show that traction stress is biphasic with adhesion size. There is an optimal adhesion size that maximizes traction

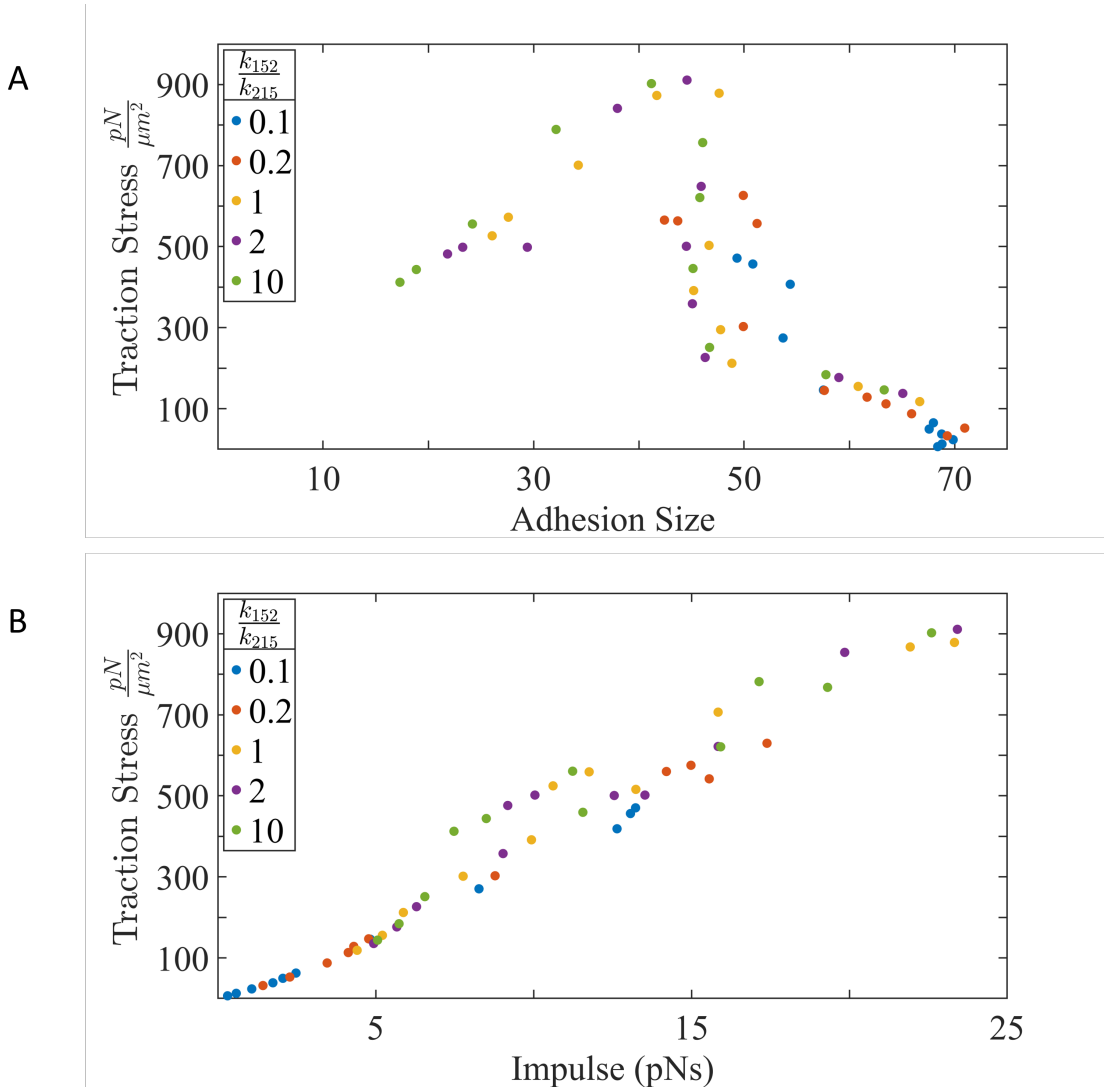

FIGURE 6.8: A) Traction stress is biphasic with adhesion size. There is an initial increase in traction stress with adhesion growth, followed by a decrease in traction stress with adhesion growth. B) Traction force increases almost linearly with impulse.

force. Passing this optimal size, traction force decreases. These results could explain how highly motile cells exhibit inverse correlation between adhesion size, migration speed, and increased invasiveness [144, 195]. Increasing forces increase the likelihood that integrins will rupture their bond with the substrate and decreases the bonds lifetime. Decreasing bond lifetimes affect adhesion size. We can make a generalization that large adhesion have integrins that experience longer bond lifetimes but transmit

lower forces than small adhesions whose integrins experience shorter bond lifetimes but transmit greater forces. In this respect, our results agree with trends that relatively small adhesions transmit greater forces that large adhesions [196] and that adhesions $< 1\mu\text{m}^2$ exhibit widely variable traction stress [197, 198]. However, below a certain adhesion size, there might not be sufficient active attachments transmitting forces and traction force falls again. Individual integrins experience a range of forces that when evaluated as an aggregate reveal traction stress. Traction force is not simply the product of motor activity, substrate stiffness, bond lifetime, or adhesion size. Experiments show that traction force increases monotonically with substrate stiffness [199, 200]. This is certainly true within a specific substrate stiffness range spanning 3 orders of magnitude, after which traction force decreases. The traction stress biphasic behavior we observe is predicted in other models where those biphasic behaviors are attributed to actin retrograde flow, which may not be that different from bond breaking [201–203]. We note that the biphasic behavior of traction stress is context dependent. The biphasic behavior is not seen in simulations with low ppMLC2. These simulations instead show a sigmoidal behavior. The existence of both biphasic and monophasic traction force response is a novel finding beyond what is reported by other models. In either case, the traction stresses arise solely from the combined actin-myosin contractility and not from actin flow. We have identified how force develops in single filaments and how both ppMLC2 and substrate stiffness are sufficient to increase force. These observations of force generation in individual fibers does not scale up to traction stress per μm^2. Instead, if we consider the impulse transmitted by individual actin-myosin filaments during each active binding event, a trend emerges (Figure 6.8B). Impulse is calculated by

$$I = \int_{\tau_1}^{\tau_2} F \, dt \tag{6.16}$$

where τ_1 to τ_2 is the time window when an actin-myosin filament is actively transmitting force to the substrate via an integrin bond.

6.4 Conclusion

Different cell types generate different levels of traction stress. The forces themselves are not exclusive to a cell type. Rather, forces are dependent on myosin contractility and microenvironment. We showed this by explicitly modeling motor activity. Stall forces for individual actin-myosin filaments are dependent on the number of motors and substrate stiffness. Counterintuitively, traction stress is not linearly dependent on stall force. Rather, traction stress is limited by the bond lifetime. Consequently, we show that traction stress is proportional to the impulse by individual actin-myosin substrate attachments. Further more, there is no direct relationship with traction stress and adhesion size. We show that traction stress increases within a limited range of adhesion growth followed by a decrease in traction force as the adhesion size increases. Our model outputs can be used as inputs in other pathways that are dependent on force, such as FAK signaling to create a unified model with chemomechanical feedback.

Chapter 7

Conclusion

Proper regulation of cellular function requires the integration of many signals. We explored intracellular calcium signaling activated by chemoelectric signals in heart cells and how proper calcium signaling is crucial to force generation to maintain heart health and function. We discussed how dysregulation of calcium handling in heart cells affects force production and has deleterious effects on cardiovascular health. In epithelial cells, we described a mechanism by which βAR activation by chemical cues increased force generation. We further explored how epithelial cells generate force as a response substrate stiffness. Both chemical and mechanical signaling are known to increase a tumor's metastatic potential. Clearly, chemomechanical signal transduction connects mechanics to biology. Thus, quantitative evaluation of force is useful in understanding physiological and pathological processes.

Aiding our understanding of cellular force generation are mathematical and computational models that integrate physics, biophysics, and biochemistry. Modeling allows us to impose data-driven assumptions regarding biophysical and biochemical properties. Models are incrementally leveling up our understanding of how chemical signals affect cellular mechanics. Computational models allow us to simulate scenarios at spatial and temporal scales not yet feasible experimentally. This is a powerful advantage

as we are not limited by instrument sampling rates. Thus, mathematical and computational models allow us to generate testable hypotheses, or hypotheses that are not yet testable.

While we only focused on a handful of proteins, our model yielded insightful mechanistic explanations of force generation at the molecular level. Our model has the potential to be used by researchers investigating force generation by actin-myosin contractility. For example, while our model does not currently have calcium as a regulatory signal, it can be easily adapted to include calcium dependency [140]. In this manner, we could use the calcium transient from our neonatal cell model as an input parameter in the contractility model. Other applications of our model could include cadherins. Cadherins are similar to integrins, except that cadherins attach cells to neighboring cells, not a substrate. This could be incredibly useful for models of collective cell migration. Further more, our model could be used as a module for another model that requires simulated real-time force.Furthermore, our model could provide a missing link between force generation and mechanotransduction, the conversion of mechanical signals into biochemical signals, such as activation of FAK (focal adhesion kinase) signaling. This would be a significant contribution to our model as we currently do not have any downstream effects of force by other mechanosensitive proteins, like FAK. FAK is perched between integrins and actin-myosin filaments and is a key regulator of traction force. Those signals could then feedback into our model to provide a more complete picture. We look forward to the exciting discoveries that the next decade will bring in this highly collaborative interdisciplinary area of research.

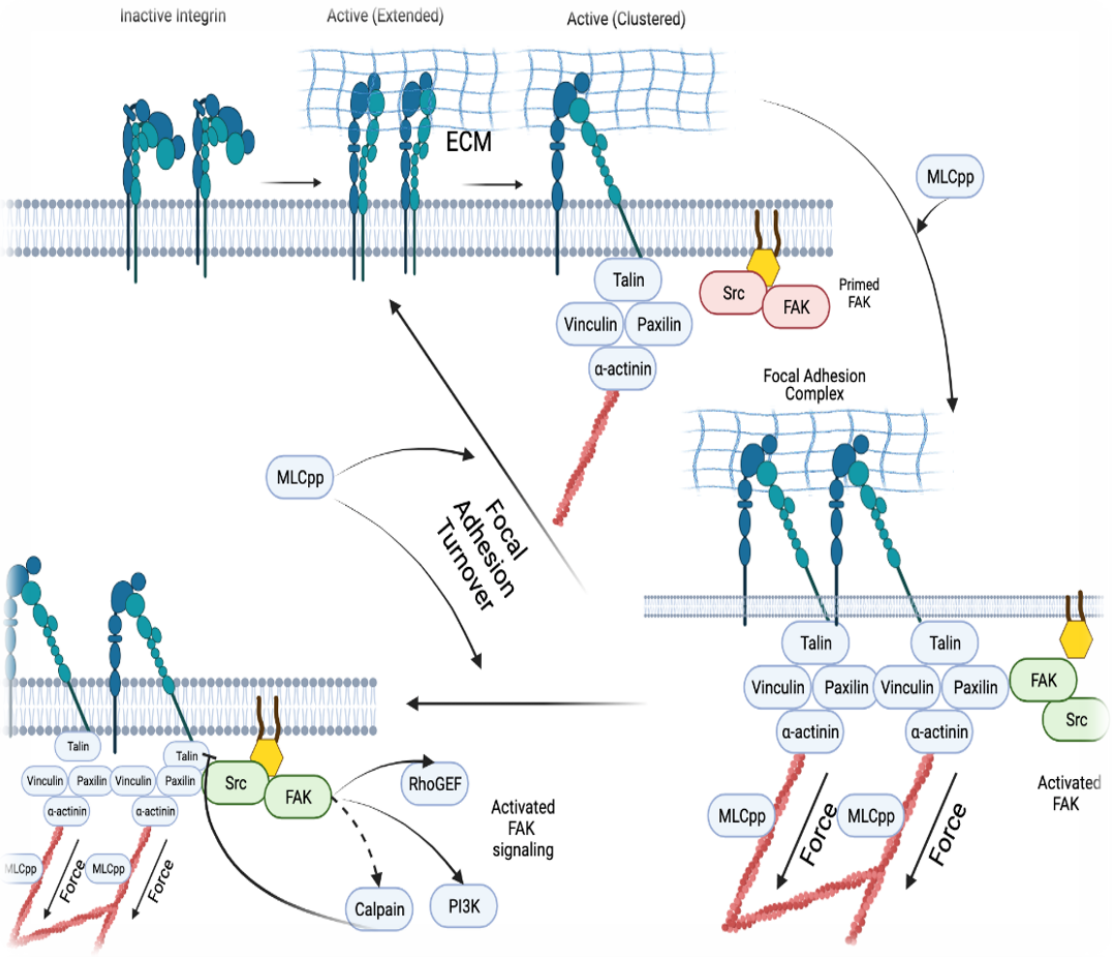

FIGURE 7.1: Our model could be useful for force sensitive proteins that provide downstream signaling and feedback into our model. FAK (focal adhesion kinase) is a likely candidate for transducing mechanical signals to chemical signals.

Appendix A

Supplementary Material: Tables

Supplementary Table 1. qRT-PCR results of RyR, NCX, and SERCa 48 hours after RyR siRNA transfection.

	Control						**Transfected**					
	GAPDH	GAPDH	GAPDH	RyR	RyR	RyR	GAPDH	GAPDH	GAPDH	RyR	RyR	RyR
C_T	26.04	26.24	26.32	25.24	25.24	25.24	26.05	27.00	26.22	27.02	27.11	27.04
Mean C_T			26.20			25.34			26.42			27.06
ΔC_T[a]						-0.86						0.63
$\Delta\Delta C_T$[b]												1.49
$2^{-\Delta\Delta CT}$												0.35
	GAPDH	GAPDH	GAPDH	NCX	NCX	NCX	GAPDH	GAPDH	GAPDH	NCX	NCX	NCX
C_T	26.04	26.24	26.32	27.02	27.11	27.04	26.04	26.19	26.01	25.95	26.35	26.10
MeanC_T			26.20			27.06			26.08			26.13
ΔC_T[a]						0.86						0.05
$\Delta\Delta C_T$[b]												-0.81
$2^{-\Delta\Delta CT}$												1.75
	GAPDH	GAPDH	GAPDH	SERCA	SERCA	SERCA	GAPDH	GAPDH	GAPDH	SERCA	SERCA	SERCA
C_T	23.28	23.46	23.75	21.32	21.06	20.85	23.87	24.19	54.01	22.32	22.32	22.14
Mean C_T			23.50			21.08			24.02			22.26
ΔC_T[a]						-2.42						-1.76
$\Delta\Delta C_T$[b]												0.66
$2^{-\Delta\Delta CT}$												0.63

[a] ΔC_T = Mean C_T Transfected – Mean C_T GAPDH

[b] $\Delta\Delta C_T$ = ΔC_T Transfected – ΔC_T GAPDH

Supplementary Table 2. qRT-PCR results of RyR, NCX, and SERCa 48 hours after NCX siRNA transfection.

	Control						**Transfected**					
	GAPDH	GAPDH	GAPDH	NCX	NCX	NCX	GAPDH	GAPDH	GAPDH	NCX	NCX	NCX
C_T	27.11	27.11	27.06	23.67	23.67	23.42	26.26	25.73	25.96	24.71	24.57	24.35
Mean C_T			27.09			23.42			25.98			24.54
Δ C_T[a]						-3.68						-1.44
$\Delta\Delta C_T$[b]												2.24
$2^{-\Delta\Delta CT}$												0.21
	GAPDH	GAPDH	GAPDH	SERCA	SERCA	SERCA	GAPDH	GAPDH	GAPDH	SERCA	SERCA	SERCA
C_T	16.84	16.95	17.01	18.55	18.07	18.32	16.71	16.47	16.58	17.22	17.32	17.43
MeanC_T			16.93			18.31			16.59			17.32
Δ C_T[a]						1.38						0.74
$\Delta\Delta C_T$[b]												-0.64
$2^{-\Delta\Delta CT}$												1.56
	GAPDH	GAPDH	GAPDH	RyR	RyR	RyR	GAPDH	GAPDH	GAPDH	RyR	RyR	RyR
C_T	27.08	27.08	26.03	24.23	24.94	24.79	26.51	26.70	27.03	24.75	24.63	24.78
Mean C_T			26.73			24.65			26.75			24.72
Δ C_T[a]						-2.08						-2.03
$\Delta\Delta C_T$[b]												0.05
$2^{-\Delta\Delta CT}$												0.97

[a] ΔC_T = Mean C_T Transfected – Mean C_T GAPDH

[b] $\Delta\Delta C_T$ = ΔC_T Transfected – ΔC_T GAPDH

TABLE A.1: Model parameters

Parameter	Definition	Value	Unit	Reference
k_{12}	State 1 to 2 rate	1.4×10^{-4}	ms^{-1}	[183]
k_{23}	State 2 to 3 rate	7.0×10^{-3}	ms^{-1}	[183]
k_{32}	State 3 to 2 rate	1.1×10^{-2}	ms^{-1}	[183]
k_{34}	State 4 to 4 rate	1.6×10^{-4}	ms^{-1}	[183]
k_{41}	State 4 to 1 rate	2.8×10^{-2}	ms^{-2}	[183]
k_{152}	State 15 to 2 rate	1	ms^{-1}	Estimated
k_{215}	State 2 to 15 rate	$k_{152} \times \frac{MLC}{ppMLC}$	ms^{-1}	Calculated
k_m	Motor stalk stiffness	4	pN	[204]
k_B	Boltzmann's constant	$1.3890610\times^{-2}$	J/K	
T	Temperature	300	K	
δ	Myosin bond length	2.5	nm	[77]
k_{act}	Integrin activation rate	23	ms^{-1}	[205]
k_{att}	Integrin attachment rate	1×10^{3}	ms^{-1}	[206]
y	Motor step size	5.3	nm	[207]
k_{spring}	Substrate spring constant	0.1-1000	pN/nm	
k_0	Slip bond off rate	0.1	ms^{-1}	[208]
γ	Drag on actin-myosin	6×10^{-4}	pNms/nm	[209]
k^0_{catch}	Unloaded catch off rate	5.5×10^{-2}	ms^{-1}	[188]
k^0_{slip}	Unloaded slip off rate	5.2×10^{-7}	ms^{-1}	[188]
A	Fitting constant	3309	ms^{-1}	[131]
B	Fitting constant	3.942×10^{-7}	ms^{-1}	[131]
C	Fitting constant	5.819×10^{-2}	ms^{-1}	[131]
ξ	Unbinding length	0.74	nm	[131]
k_{sfatt}	Actin-myosin attachment rate	0.65	ms^{-1}	[206]
k_{rec}	Talin recruiting rate	1.8×10^{-2}	ms^{-1}	[210]
k_{branch}	Talin branching rate	2.5×10^{-5}	ms^{-1}	[210]
R	No. of recruited filaments	From simulation		
b	No. of branched integrins	From simulation		

Appendix B

Supplementary Material: Figures

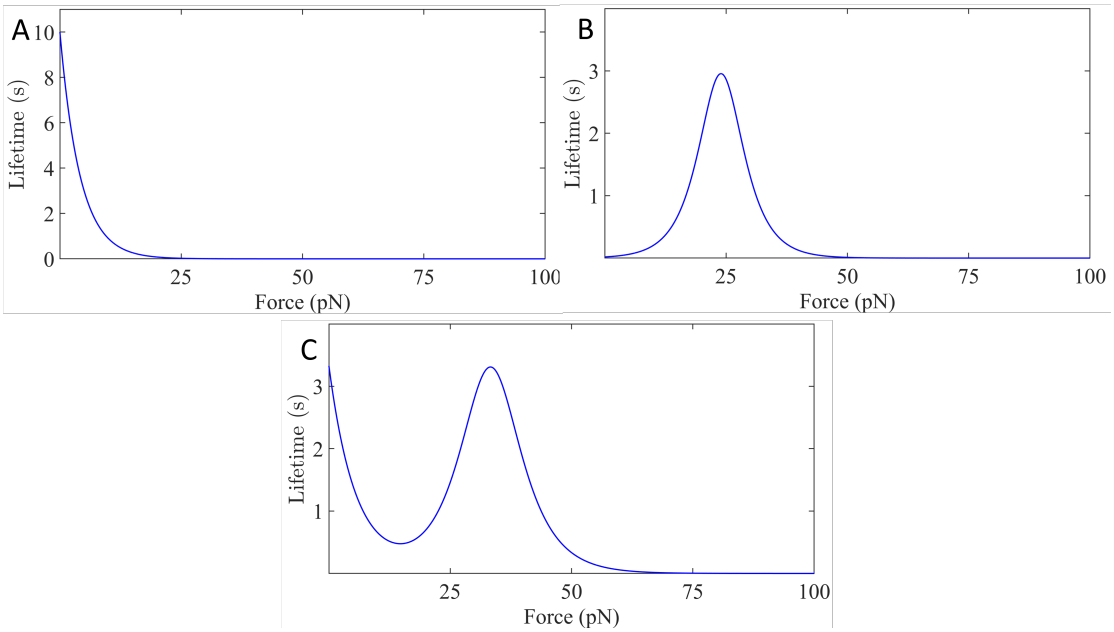

FIGURE B.1: Theoretical lifetimes for A) slip bonds, B) catch-slip bonds, and C) updated catch-slip bonds

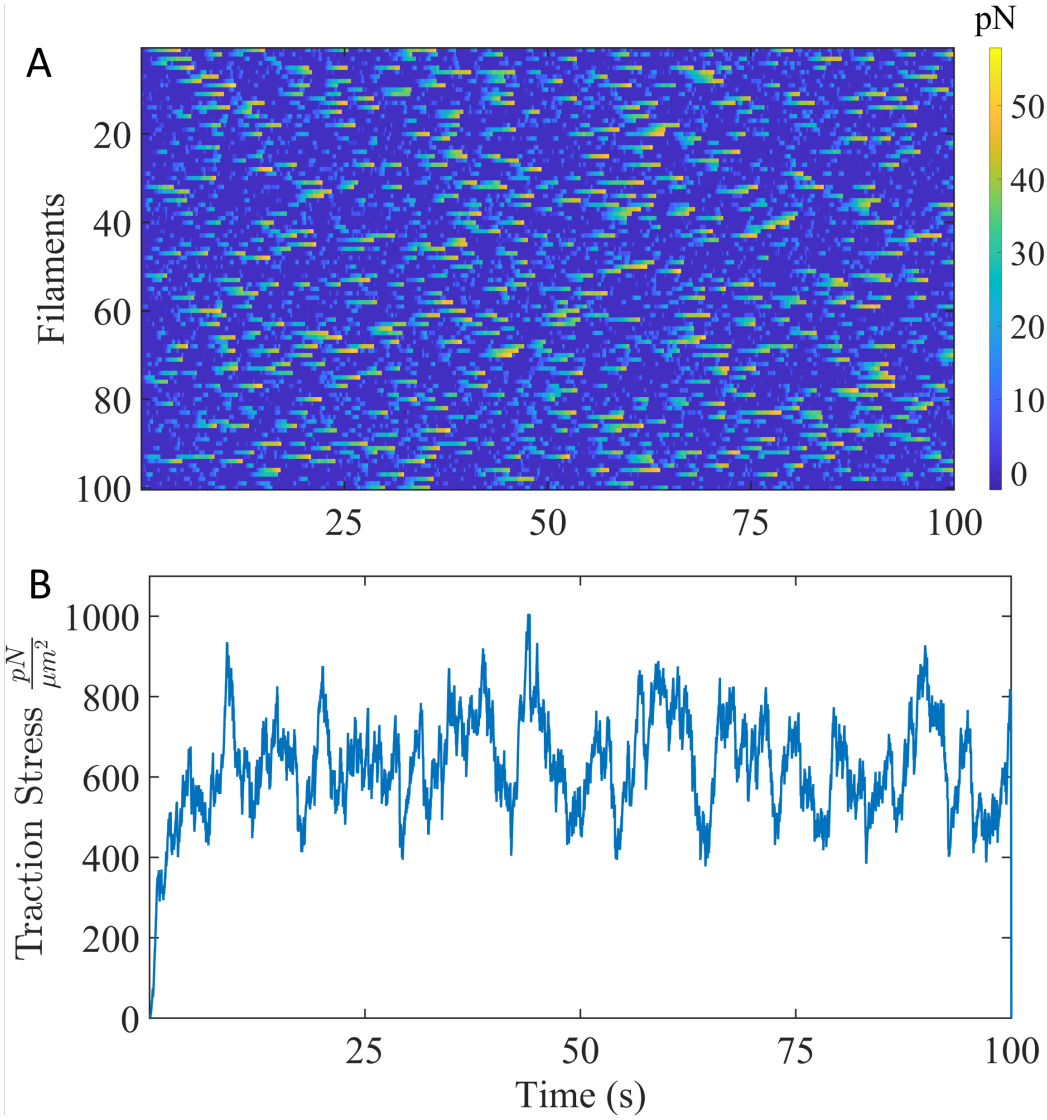

FIGURE B.2: A) Heatmap representation of 100 force-transducing integrins over 1– seconds. B) Traction stress is the sum of all forces of 100 integrins at time t for all t.

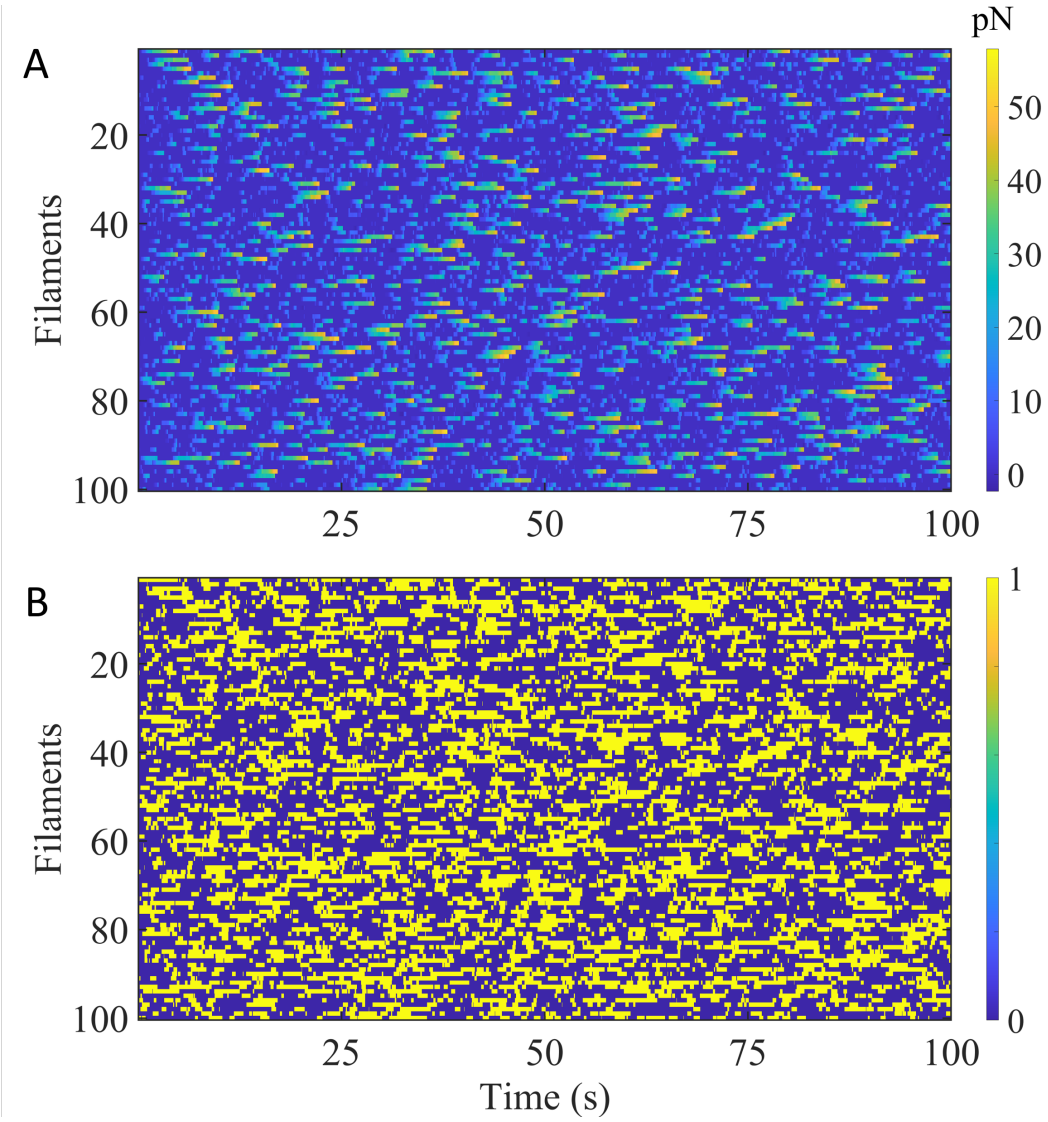

FIGURE B.3: A) Heatmap representation of 100 force-transducing integrins (y-axis) over 100 seconds (x-axis). Force is transmitted to the substrate when there is an intact physical connection between actin-myosin and integrin. B) Matrix representation of integrins trasmitting force to the substrate (1 = force transducing integrin, 0 = non-force transducing integrin. Bond lifetimes are calculated by counting the consecutive 1's.

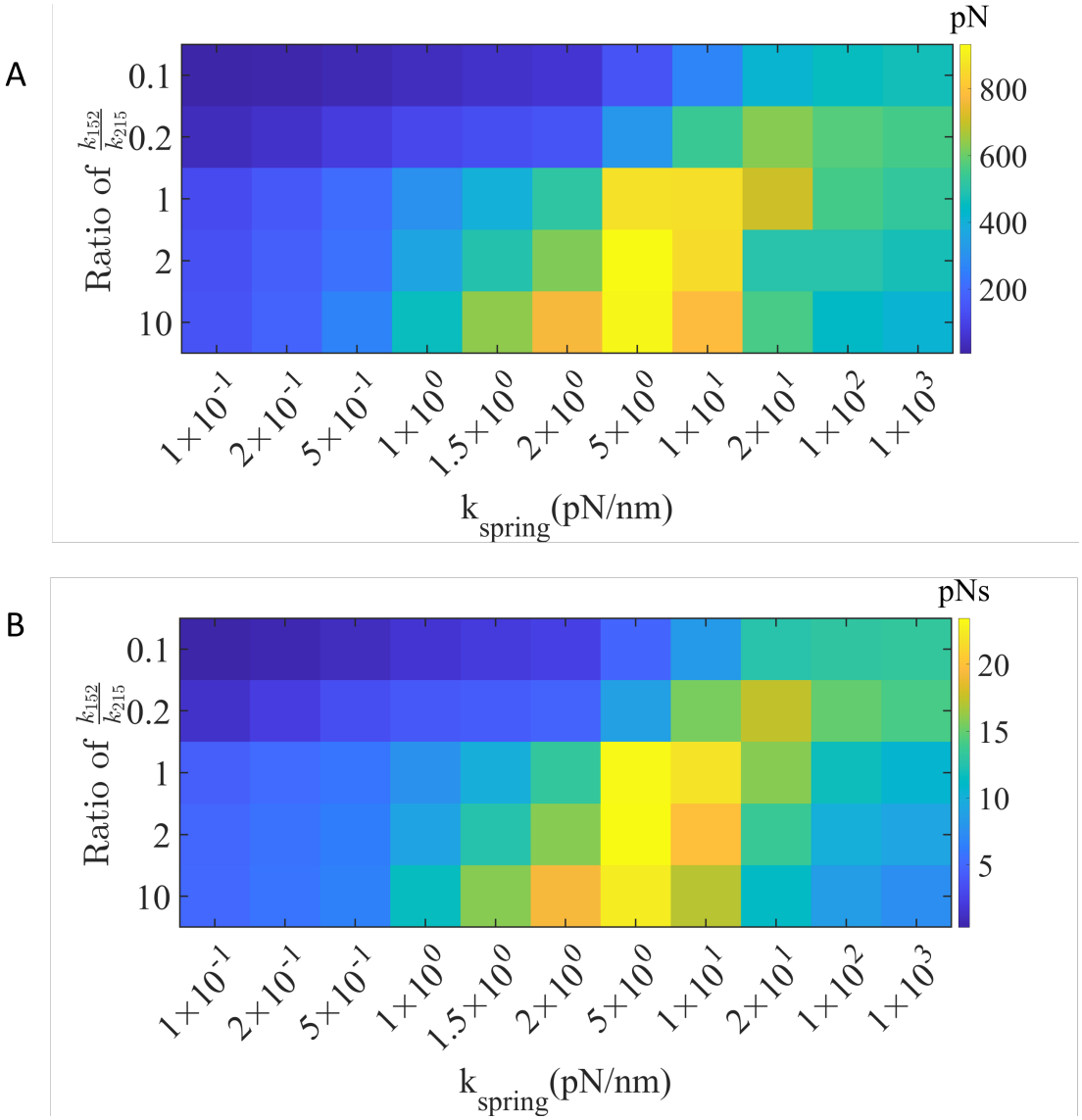

FIGURE B.4: Heatmaps of (A) traction stress (B) and impulse show similar trends, suggesting that impulse drives traction force magnitude

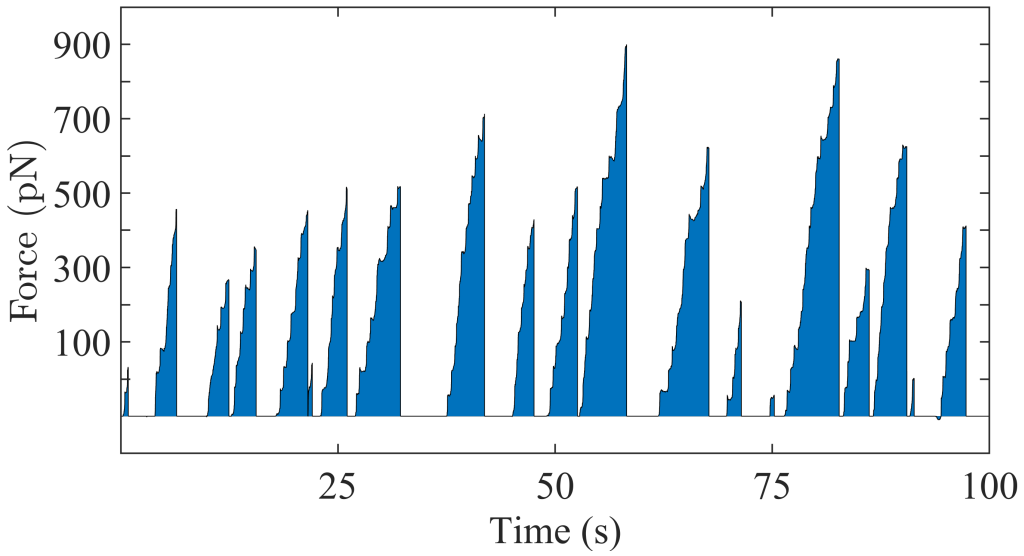

FIGURE B.5: Impulse is the area under the force curve. We calculate the curve for each binding event. We then take the average of all impulse values to determine average impulse.

References

[1] Henry N Higgs and Thomas D Pollard. "Regulation of Actin Complex and WASp / Scar Proteins". In: *Journal of Biological Chemistry* 274.46 (1999), pp. 32531–32534. ISSN: 0021-9258. DOI: 10.1074/jbc.274.46.32531. URL: http://dx.doi.org/10.1074/jbc.274.46.32531.

[2] M Amanda Hartman and A James. "The myosin superfamily at a glance". In: *Journal of Cell Science* 125.7 (2011), pp. 1627–1632. DOI: 10.1242/jcs.094300.

[3] Miguel Vicente-Manzanares et al. "Nonmuscle myosin II takes centre stage in cell adhesion and migration". In: *Nature Reviews Molecular Cell Biology* 10.778-790 (2009). DOI: https://doi.org/10.1038/nrm2786.

[4] S. Pellegrin and H. Mellor. "Actin stress fibres". In: *Journal of Cell Science* 120.20 (2007), pp. 3491–3499. DOI: 10.1242/jcs.018473.

[5] A. F. Huxley. "The Journal of Physiology, Vol. 243, No. 1 Frontispiece". In: *The Journal of Physiology* 243.1 (1974), pp. 1–43.

[6] AF Huxley and R Niedergerke. "Structural changes in muscle during contraction: interference microscopy of living muscle fibres". In: *Nature* 173 (1954), pp. 971–973. DOI: https://doi.org/10.1038/173973a0.

[7] Thomas Brand. "Heart development: Molecular insights into cardiac specification and early morphogenesis". In: *Developmental Biology* 258.1 (2003), pp. 1–19. DOI: 10.1016/S0012-1606(03)00112-X. arXiv: NIHMS150003.

[8] Stefan Neef and Lars S Maier. "Remodeling of Excitation-contraction Coupling in the Heart : Inhibition of Sarcoplasmic Reticulum Ca^{2+} Leak as a Novel Therapeutic Approach". In: *Current Heart Failure Reports* 4 (2007), pp. 11–17. DOI: https://doi.org/10.1007/s11897-007-0020-7.

[9] Sumihiko Seki et al. "Fetal and postnatal development of Ca^{2+} transients and Ca^{2+} sparks in rat cardiomyocytes". In: *Cardiovascular Research* 58 (2003), pp. 535–548. DOI: doi:10.1016/S0008-6363(03)00255-4.

[10] Donald M Bers. "Calcium Fluxes Involved in Control of Cardiac Myocyte Contraction". In: *Circulation Research* 87 (2000), pp. 275–281. DOI: https://doi.org/10.1161/01.RES.87.4.275.

[11] Gordon J Betts et al. *Anatomy and Physiology*. Houston, Texas: OpenStax College, CC BY 3.0 https://creativecommons.org/licenses/by/3.0, via Wikimedia Commons, 2013. URL: https://commons.wikimedia.org/wiki/File:2037_Embryonic_Development_of_Heart.jpg.

[12] Hadi S Hosseini, Kara E Garcia, and Larry A Taber. "A new hypothesis for foregut and heart tube formation based on differential growth and actomyosin contraction". In: *Development* 144 (2017), pp. 2381–2391. DOI: 10.1242/dev.145193.

[13] Timothy Vu, Ricardo Miguel Castro, and Lidong Qin. "Bridging the gap: microfluidic devices for short and long distance cell-cell communication". In: *Lab Chip* 17 (2017), pp. 1009–1023. DOI: 10.1039/c6lc01367h.

[14] Donald M Bers. "Calcium Cycling and Signaling in Cardiac Myocytes". In: *Annual Review of Physiology* 70 (2008), pp. 23–49. DOI: 10.1146/annurev.physiol.70.113006.100455.

[15] Eric A Sobie and Hena R Ramay. "Excitation – contraction coupling gain in ventricular myocytes : insights from a parsimonious model". In: *Journal of Physiology* 6 (2009), pp. 1293–1299. DOI: 10.1113/jphysiol.2008.163915.

[16] Andrew R Marks. "Cardiac Intracellular Calcium Release Channels. Role in Heart Failure". In: *Circulation Research* 87 (2000), pp. 8–11. DOI: https://doi.org/10.1161/01.RES.87.1.8.

[17] Shmuel Hurwitz. "Homeostatic Control of Plasma Calcium Concentration". In: *Critical Reviews in Biochemistry and Molecular Biology* 31.1 (1996), pp. 41–100. DOI: 10.3109/10409239609110575.

[18] Topi Korhonen, Risto Rapila, and Pasi Tavi. "Mathematical Model of Mouse Embryonic Cardiomyocyte Excitation-Contraction Coupling". In: *The Journal of General Physiology* 132.4 (2008), pp. 407–419. DOI: 10.1085/jgp.200809961.

[19] Pasi Tavi, Topi Korhonen, and Sandra L Ha. "Model of Excitation-Contraction Coupling of Rat Neonatal Ventricular Myocytes". In: *Biophysical Journal* 96 (2009), pp. 1189–1209. DOI: 10.1016/j.bpj.2008.10.026.

[20] Donald M Bers. "Cardiac excitation–contraction coupling". In: *Nature* 415 (2002), pp. 198–205. DOI: https://doi.org/10.1038/415198a.

[21] T. R. Shannon, K. S. Ginsburg, and D. M. Bers. "Potentiation of fractional sarcoplasmic reticulum calcium release by total and free intra-sarcoplasmic reticulum calcium concentration". In: *Biophysical Journal* 78 (2000), pp. 334–343. DOI: 10.1016/S0006-3495(00)76596-9.

[22] Donald M Bers and Edward Perez-reyes. "Ca channels in cardiac myocytes : structure and function in Ca influx and intracellular Ca release". In: *Cardiovascular Research* 42 (1999), pp. 339–360. DOI: https://doi.org/10.1016/S0008-6363(99)00038-3.

[23] G.N. Phillips, J.P. Fillers, and C. Cohen. "Tropomyosin crystal structure and muscle regulation". In: *Journal of Molecular Biology* 192.1 (1986), pp. 111–127. DOI: https://doi.org/10.1016/0022-2836(86)90468-7.

[24] William Lehman, Elumalai Pavadai, and Michael J. Rynkiewicz. "C-terminal troponin-I residues trap tropomyosin in the muscle thin filament blocked-state". In: *Biochemical and Biophysical Research Communications* 551 (2021), pp. 27–32. ISSN: 0006-291X. DOI: https://doi.org/10.1016/j.bbrc.2021.03.010. URL: https://www.sciencedirect.com/science/article/pii/S0006291X21003922.

[25] Setsuro Ebashi, Takeyuki Wakabayashi, and Fumiko Ebashi. "Troponin and Its Components". In: *Journal of Biochemistry* 66.2 (1971), pp. 441–445. DOI: https://www.jstage.jst.go.jp/article/biochemistry1922/69/2/69_2_441/_article/-char/ja.

[26] Chuck S Farah and Fernando C Reinach. "The troponin compolex and regulation of muscle contraction". In: *FASEB Journal* 9 (1995), pp. 755–767. DOI: 10.1096/fasebj.9.9.7601340.

[27] AF Huxley. "Muscle structure and theories of contraction". In: *Nature* 173 (1957), pp. 971–973. DOI: PMID:13485191.

[28] Scott A Henderson et al. "Functional Adult Myocardium in the Abscence of Na^{+}-Ca^{2+} Exchange. Cardiac-Specific Knockout of NCX1". In: *Circulation Research* 17.6 (2004), pp. 604–611. DOI: 10.1161/01.RES.0000142316.08250.68.

[29] Gerd Hasenfuss et al. "Excitation-Contraction Coupling and Contractile Protein Function in Failing and Nonfailing Human Myocardium". In: *Interactive Phenomena in the Cardiac System*. Ed. by Samuel Sideman and Rafael Beyar. Boston, MA: Springer US, 1993, pp. 91–100. ISBN: 978-1-4615-2946-0. DOI: 10.1007/978-1-4615-2946-0_9. URL: https://doi.org/10.1007/978-1-4615-2946-0_9.

[30] Steven M Pogwizd and Donald M Bers. "Calcium Cycling in Heart Failure : The Arrhythmia Connection". In: *Journal of cardiovascular electrophysiology* 13.1 (2002), pp. 88–91. DOI: https://doi.org/10.1046/j.1540-8167.2002.00088.x.

[31] Andriy E Belevych et al. "The relationship between arrhythmogenesis and impaired contractility in heart failure : role of altered ryanodine receptor function". In: *Cardiovascular Research* 90 (2011), pp. 493–502. DOI: 10.1093/cvr/cvr025.

[32] M Lindner et al. "Calcium sparks in human ventricular cardiomyocytes from patients with terminal heart failure". In: *Cell Calcium* 31 (2002), pp. 175–182. DOI: 10.1054/ceca.2002.0272.

[33] Steven O Marx et al. "PKA Phosphorylation Dissociates FKBP12 . 6 from the Calcium Release Channel (Ryanodine Receptor): Defective Regulation in Failing Hearts". In: *Cell* 101 (2000), pp. 365–376. DOI: https://doi.org/10.1016/s0092-8674(00)80847-8.

[34] Zuzana Kubalova et al. "Abnormal intrastore calcium signaling in chronic heart failure". In: *Proceedings of the National Academy of Sciences* 102.39 (2005), pp. 1–6. DOI: https://doi.org/10.1073/pnas.0504298102.

[35] Robert H G Schwinger et al. "Reduced Ca^{2+} Sensitivity of SERCA 2a in Failing Human Myocardium due to Reduced Serin-16 Phospholamban Phoshorylation". In: *Journal of Molecular and Cellular Cardiology* 491 (1999), pp. 479–491. DOI: https://doi.org/10.1006/jmcc.1998.0897.

[36] Valentino Piacentino et al. "Human Ventricular Myocytes". In: *Circulation Research* 92 (2003). DOI: 10.1161/01.RES.0000062469.83985.9B.

[37] Carlos Bazan et al. "Image processing techniques for assessing contractility in isolated neonatal cardiac myocytes". In: *International Journal of Biomedical Imaging* 2011 (2011), pp. 1–9. DOI: 10.1155/2011/729732.

[38] Paul Paolini et al. "Developmental and extracellular matrix-remodeling processes in rosiglitazone-exposed neonatal rat cardiomyocytes". In: *Pharmacogenomics* 15.6 (2014), pp. 759–774. DOI: 10.2217/pgs.14.39.Developmental.

[39] Andrew P. Ziman et al. "Excitation-Contraction Coupling Changes During Postnatal Cardiac Development". In: *Journal of Molecular and Cellular Cardiology* 48.2 (2010), pp. 379–386. DOI: 10.1016/j.yjmcc.2009.09.016.Excitation-Contraction.

[40] Peter Lipp and Ernst Niggli. "Modulation of Ca^{2+} Release in Cultured Neonatal Rat Cardiac Myocytes. Insight From Subcellular Release Patterns Revealed by Confocal Microscopy". In: *Circulation Research* 74.5 (1993), pp. 979–990. DOI: https://doi.org/10.1161/01.res.74.5.979.

[41] Laura L Winka, Sheng-Yong Wang, and Glenn A Langer. "Subcellular Ca^{2+} Distribution with Varying Ca^{2+} Load in Neonatal Cardiac Cell Culture". In: *Biophysical Journal* 76 (1999), pp. 2649–2663. DOI: 10.1016/S0006-3495(99)77417-5.

[42] William E Louch, Jussi T Koivum, and Pasi Tavi. "Calcium signalling in developing cardiomyocytes : implications for model systems and disease". In: *Journal of Physiology* 593.5 (2015), pp. 1047–1063. DOI: 10.1113/jphysiol.2014.274712.

[43] Donald M. Bers and Tao Guo. "Calcium signaling in cardiac ventricular myocytes". In: *Annals of the New York Academy of Sciences* 1047 (2005), pp. 86–98. DOI: 10.1196/annals.1341.008.

[44] Fabien Brette et al. "Spatiotemporal characteristics of SR Ca^{2+} uptake and release in detubulated rat ventricular myocytes". In: *Journal of Molecular and Cellular Cardiology* 39 (2005), pp. 804–812. DOI: 10.1016/j.yjmcc.2005.08.005.

[45] Fabien Brette et al. "Ca^{2+} currents in cardiac myocytes: Old story, new insights". In: *Progress in Biophysics and Molecular Biology* 91 (2006), pp. 1–82. DOI: 10.1016/j.pbiomolbio.2005.01.001. URL: http://linkinghub.elsevier.com/retrieve/pii/S0079610705000039.

[46] Alexandre Fabiato. "Time and Calcium Dependence of Activation and Inactivation of Calcium-induced Release of Calcium from the Sarcoplasmic Reticulum of a Skinned Canine Cardiac Purkinje Cell". In: *Journal of General Physiology* 85 (1985), pp. 247–289. DOI: https://doi.org/10.1085/jgp.85.2.247.

[47] A. Lacampagne, C. Caputo, and J. Argibay. "Effect of ryanodine on cardiac calcium current and calcium channel gating current". In: *Biophysical Journal* 70.1 (1996), pp. 370–375. ISSN: 00063495. DOI: 10.1016/S0006-3495(96)79580-2.

[48] Rosana A Bassani and A Rosana. "Contribution of Ca $^{2+}$ transporters to relaxation in intact ventricular myocytes from developing rats". In: *American Journal of Physiology - Heart and Circulatory Physiology* 282 (2002), pp. 2406–2413. DOI: 10.1152/ajpheart.00320.2001.

[49] Dmitry Terentyev et al. "Luminal Ca^{2+} Controls Termination and Refractory Behavior of Ca^{2+}-Induced Ca^{2+} Release in Cardiac Myocytes". In: *Circulation Research* 91 (2002), pp. 414–420. DOI: 10.1161/01.RES.0000032490.04207.BD.

[50] Min Fu et al. "Sarcoplasmic reticulum Ca^{2+} release channel ryanodine receptor (RyR_2) plays a crucial role in aconitine-induced arrhythmias". In: *Biochemical Pharmacology* 75 (2008), pp. 2147–2156. DOI: 10.1016/j.bcp.2008.02.027.

[51] Rajanya D Shah et al. "Cellular Physiology and Biochemistr y Biochemistry The Antidiabetic Agent Rosiglitazone Upregulates SERCA2 and Enhances TNF-α- and LPS-Induced NF-κB-Dependent Transcription and TNF-α- Induced IL-6 Secretion in Ventricular Myocytes". In: *Cellular Physiology and Biochemistry* 15 (2004), pp. 41–50. DOI: https://doi.org/10.1159/000083637.

[52] Akiyuki Takahashi et al. "Measurement of Intracellular Calcium". In: *Physiological Reviews* 79.4 (1999), pp. 1089–1125. DOI: https://doi.org/10.1152/physrev.1999.79.4.1089.

[53] TR Shannon. "Integrated Ca^{2+} Management in Cardiac Myocytes". In: *Annals of the New York Academy of Sciences* 1015 (2004), pp. 28–38. DOI: 10.1196/annals.1302.003.

[54] S Morotti et al. "A novel computational model of mouse myocyte electrophysiology to assess the synergy between Na^+ loading and CaMKII". In: *Journal of Physiology* 592.6 (2014), pp. 1181–1197. DOI: 10.1113/jphysiol.2013.266676.

[55] Eleonora Grandi, Francesco S Pasqualini, and Donald M Bers. "A novel computational model of the human ventricular action potential and Ca transient". In: *Journal of Molecular and Cellular Cardiology* 48 (2010), pp. 112–121. ISSN: 0022-2828. DOI: 10.1016/j.yjmcc.2009.09.019.

[56] Gerd Hasenfuss and Burkert Pieske. "Calcium Cycling in Congestive Heart Failure". In: *Journal of Molecular and Cellular Cardiology* 34 (2002), pp. 951–969. DOI: doi:10.1006/jmcc.2002.2037. URL: http://www.idealibrary.com.

[57] Gerd Hasenfuss et al. "Relationship Between Na^+-Ca^{2+}-Exchanger Protein Levels and Diastolic Function of Failing Human Myocardium". In: *Circulation* 99 (1999), pp. 641–648. DOI: https://doi.org/10.1161/01.cir.99.5.641.

[58] Christian Pott, Joshua I Goldhaber, and Kenneth D Philipson. "Genetic manipulation of cardiac Na^+/Ca^{2+} change expression". In: *Biochemical and Biophysical Research Communications* 322 (2004), pp. 1336–1340. DOI: 10.1016/j.bbrc.2004.08.038.

[59] Christian Pott et al. "Regulation of Cardiac L-Type Ca^{2+} Current in Na^+-Ca^{2+} Exchanger Knockout Mice : Functional Coupling of the Ca Channel and the Na^+-Ca^{2+} Exchanger". In: *Biophysical Journal* 92.4 (2007), pp. 1431–1437. ISSN: 0006-3495. DOI: 10.1529/biophysj.106.091538. URL: http://dx.doi.org/10.1529/biophysj.106.091538.

[60] Donald M Bers, David A Eisner, and Héctor H. Valdivia. "Sarcoplasmic Reticulum Ca^{2+} and Heart Failure". In: *Circulation Research* 93.6 (2003), pp. 487–490. DOI: 10.1161/01.RES.0000091871.54907.6B.

[61] H L Roderick et al. "Calcium in the heart: when it's good, it's very very good, but when it's bad, it's horrid". In: *Biochemical Society Transactions* 35.5 (2007), pp. 957–961. ISSN: 03005127. DOI: 10.1042/BST0350957.

[62] W M Bassani, Weilong Yuan, and Donald M Bers. "Fractional SR Ca release is regulated by trigger and SR Ca content in cardiac myocytes". In: (2021).

[63] Roland Studer et al. "Gene Expression of the Cardiac Na^{+}-$^{2+}$ Exchanger in End-Stage Human Heart Failure". In: *Circulation Research1* 75.3 (1994), pp. 443–453. DOI: https://doi.org/10.1161/01.res.75.3.443.

[64] Konstantina Dipla et al. "The Sarcoplasmic Reticulum and the Na^{+}/Ca^{2+} Both Contribute to the Ca^{2+} Transient of Failing Human Ventricular Myocytes". In: *Circulation Research* 84 (1999), pp. 435–444. DOI: https://doi.org/10.1161/01.res.84.4.435.

[65] D. A. Eisner et al. "The control of Ca release from the cardiac sarcoplasmic reticulum: regulation versus autoregulation". In: *Cardiovascular Research* 38 (1998), pp. 589–604. DOI: https://doi.org/10.1016/S0008-6363(98)00062-5.

[66] Steven R. Houser, Valentino Piacentino, and Jutta Weisser. "Abnormalities of calcium cycling in the hypertrophied and failing heart". In: *Journal of Molecular and Cellular Cardiology* 32.9 (2000), pp. 1595–1607. DOI: 10.1006/jmcc.2000.1206.

[67] Donald M. Bers. "Macromolecular complexes regulating cardiac ryanodine receptor function". In: *Journal of Molecular and Cellular Cardiology* 37.2 (2004), pp. 417–429. DOI: 10.1016/j.yjmcc.2004.05.026.

[68] Glenn T Lines et al. "Contribution of the Na^{+}/Ca^{2+}2 1 Exchanger to Rapid Ca^{2+} Release in Cardiomyocytes". In: *Biophysical Journal* 91.3 (2006), pp. 779–792. ISSN: 0006-3495. DOI: 10.1529/biophysj.105.072447. URL: http://dx.doi.org/10.1529/biophysj.105.072447.

[69] D A Eisner et al. "What role does modulation of the ryanodine receptor play in cardiac inotropy and arrhythmogenesis?" In: *Journal of Molecular and Cellular Cardiology* 46.4 (2009), pp. 474–481. ISSN: 0022-2828. DOI: 10.1016/j.yjmcc.2008.12.005. URL: http://dx.doi.org/10.1016/j.yjmcc.2008.12.005.

[70] Sarah C W Stevens et al. "Intra-sarcoplasmic reticulum Ca^{2+} oscillations are driven by dynamic regulation of ryanodine receptor function by luminal Ca^{2+} in cardiomyocytes". In: *Journal of Physiology* 20 (2009), pp. 4863–4872. DOI: 10.1113/jphysiol.2009.175547.

[71] GL Aistrup, CW Balke, and Ja Wasserstrom. "Arrhythmia triggers in heart failure: The smoking gun of [Ca2+]i dysregulation". In: *Heart Rhythm* 8.11 (2011), pp. 1804–1808. ISSN: 1547-5271. DOI: 10.1016/j.hrthm.2011.06.012.

[72] Roland Vetter et al. "Reciprocal Changes in the Postnatal Expression of the Sarcolemmal Na^{+}-Ca^{2+}-exchanger and SERCA2 in Rat Heart". In: *Journal of Molecular and Cellular Cardiology* 1701 (1995), pp. 1689–1701. DOI: https://doi.org/10.1016/S0022-2828(95)90788-2.

[73] Donald M. Bers. *Excitation-Contraction Coupling and Cardiac Contractile Force*. 2nd. Dordrecht: Springer Science, 2001. DOI: 10.1007/978-94-010-0658-3.

[74] Linda J Wang and Eric A Sobie. "Mathematical model of the neonatal mouse ventricular action potential". In: *American Journal of Physiology - Heart and Circulatory Physiology* 294 (2008), pp. 2565–2575. DOI: 10.1152/ajpheart.01376.2007..

[75] Kerry L Hull and Steve Harvey. "Growth Hormone and Reproduction : A Review of Endocrine and Autocrine - Paracrine Interactions". In: *International Journal of Endocrinology* 2014 (2014). DOI: http://dx.doi.org/10.1155/2014/234014.

[76] Peter Devreotes and Alan Rick Horwitz. "Signaling Networks that Regulate Cell Migration". In: *Cold Spring Harbor Perspectives in Biology* 7 (2021). DOI: doi:10.1101/cshperspect.a005959.

[77] Samantha Stam et al. "Isoforms Confer Characteristic Force Generation and Mechanosensation by Myosin II Filaments". In: *Biophysical Journal* 108.8 (2015), pp. 1997–2006. ISSN: 0006-3495. DOI: 10.1016/j.bpj.2015.03.030. URL: http://dx.doi.org/10.1016/j.bpj.2015.03.030.

[78] Rajagopal Rangarajan and Muhammad H Zaman. "Status and challenges Modeling cell migration in 3D". In: *Cell Adhesion an* 2.2 (2008), pp. 106–109. DOI: 10.4161/cam.2.2.6211.

[79] Pakorn Kanchanawong et al. "Nanoscale architecture of integrin-based cell adhesions". In: *Nature* 468.7323 (2010), pp. 580–584. ISSN: 0028-0836. DOI: 10.1038/nature09621. URL: http://dx.doi.org/10.1038/nature09621.

[80] Dong-hwee Kim and Denis Wirtz. "Focal adhesion size uniquely predicts cell migration". In: *The FASEB Journal* 27.4 (2013), pp. 1351–1361. DOI: 10.1096/fj.12-220160.

[81] Anne J. Ridley et al. "Cell Migration: Integrating Signals from Front to Back". In: *Science* 302.5651 (2003), pp. 1704–1709. DOI: 10.1126/science.1092053. eprint: https://www.science.org/doi/pdf/10.1126/science.1092053.

[82] Edward R Horton et al. "Definition of a consensus integrin adhesome and its dynamics during adhesion complex assembly and disassembly". In: *Nature Cell Biology* September (2015). DOI: 10.1038/ncb3257.

[83] Edward R Horton et al. "The integrin adhesome network at a glance". In: *Journal of Cell Science* 129 (2016), pp. 4159–4163. DOI: 10.1242/jcs.192054.

[84] Ronen Zaidel-bar et al. "Functional atlas of the integrin adhesome". In: *Nature Cell Biology* 9.8 (2007), pages858–867. DOI: https://doi.org/10.1038/ncb0807-858.

[85] Ronen Zaidel-bar et al. "Hierarchical assembly of cell – matrix adhesion complexes". In: *Biochemical Society Transactions* 32.3 (2004), pp. 416–420. DOI: https://doi.org/10.1042/bst0320416. URL: https://portlandpress.com/biochemsoctrans/article/32/3/416/63403/Hierarchical-assembly-of-cell-matrix-adhesion.

[86] E Zamir and B. Geiger. *Focal Adhesions and Related Integrin Contacts*. 2nd ed. Elsevier Inc., 2013, pp. 318–323. DOI: 10.1016/B978-0-12-378630-2.00473-4. URL: http://dx.doi.org/10.1016/B978-0-12-378630-2.00473-4.

[87] Marina Theodosiou et al. “Kindlin-2 cooperates with talin to activate integrins and induces cell spreading by directly binding paxillin”. In: *eLife* 5 (Jan. 2016). Ed. by Vivek Malhotra, e10130. ISSN: 2050-084X. DOI: 10.7554/eLife.10130.

[88] Mark H. Ginsberg Asoka Banno. “Integrin activation”. In: *Biochem Soc Trans* 36 (2016), pp. 229–234. DOI: https://doi.org/10.1042/BST0360229.

[89] Kate L. Wegener et al. “Structural Basis of Integrin Activation by Talin”. In: *Cell* 128.1 (2007), pp. 171–182. DOI: https://doi.org/10.1016/j.cell.2006.10.048. URL: https://www.sciencedirect.com/science/article/pii/S0092867406015960.

[90] Alex Carisey et al. “Vinculin Regulates the Recruitment and Release of Core Focal Adhesion Proteins in a Force-Dependent Manner”. In: *Current Biology* 23.4 (2013), pp. 271–281. DOI: https://doi.org/10.1016/j.cub.2013.01.009.

[91] Rishita Changede et al. “Nascent Integrin Adhesions Form on All Matrix Rigidities After Integrin Activation”. In: *Developmental Cell* 35.5 (2015), pp. 614–621. ISSN: 1534-5807. DOI: 10.1016/j.devcel.2015.11.001. URL: http://dx.doi.org/10.1016/j.devcel.2015.11.001.

[92] Zhiqi Sun, Armin Lambacher, and Reinhard Fassler. “Nascent Adhesions : From Fluctuations to a Hierarchical Organization”. In: *Current Biology* 24.17 (2014), pp. 801–803. DOI: 10.1016/j.cub.2014.07.061.

[93] Tamara C Bidone et al. “Multiscale model of integrin adhesion assembly”. In: *PLoS Computational Biology* 15.6 (2019), pp. 1–20. DOI: https://doi.org/10.1371/journal.pcbi.1007077.

[94] Dennis W Zhou et al. “Effects of substrate stiffness and actomyosin contractility on coupling between force transmission and vinculin – paxillin recruitment at single focal adhesions”. In: *Molecular Biology of the Cell* 28 (2017), pp. 1901–1911. DOI: 10.1091/mbc.E17-02-0116.

[95] Rajaa Boujemaa-paterski et al. “Talin-activated vinculin interacts with branched actin networks to initiate bundles”. In: *E-Journal Akuntansi Universitas Udayana* 9.e53990 (2020), pp. 1–26. DOI: DOI:https://doi.org/10.7554/eLife.53990.

[96] Sangyoon J Han et al. “Pre-complexation of talin and vinculin without tension is required for efficient nascent adhesion maturation”. In: *eLife* (2021), pp. 1–29. DOI: DOI:https://doi.org/10.7554/eLife.66151.

[97] Sangyoon J Han et al. “Decoupling Substrate Stiffness, Spread Area, and Micropost Density: A Close Spatial Relationship between Traction Forces and Focal Adhesions”. In: *Biophysical Journal* 103.August (2012), pp. 640–648. DOI: 10.1016/j.bpj.2012.07.023.

[98] Joseph P. Califano and Cynthia A. Reinhart-King. “Substrate stiffness and cell area predict cellular traction stresses in single cells and cells in contact”. In: *Cell and Molecular Bioengineering* 3.1 (2010), pp. 68–75. DOI: 10.1007/s12195-010-0102-6.Substrate.

[99] Samuel Bell, Anna-Lena Redmann, and Eugene M. Terentjev. "Universal Kinetics of the Onset of Cell Spreading on Substrates of Different Stiffness". In: *Biophysical Journal* 116.3 (2019), pp. 551–559. DOI: https://doi.org/10.1016/j.bpj.2018.12.020. URL: https://www.sciencedirect.com/science/article/pii/S0006349519300153.

[100] Dennis E Discher, Paul Janmey, and Yu-li Wang. "Tissue Cells Feel and Respond to the Stiffness of Their Substrate". In: *Science* 310.5751 (2005), pp. 1139–1143. ISSN: 0036-8075, 1095-9203. DOI: 10.1126/science.1116995. URL: http://www.sciencemag.org/content/310/5751/1139.

[101] Tony Yeung et al. "Effects of substrate stiffness on cell morphology, cytoskeletal structure, and adhesion". In: *Cell Motility* 60.1 (2005), pp. 24–34. DOI: https://doi.org/10.1002/cm.20041.

[102] Adam J. Engler et al. "Matrix Elasticity Directs Stem Cell Lineage Specification". In: *Cell* 126.4 (2006), pp. 677–689. DOI: https://doi.org/10.1016/j.cell.2006.06.044. URL: https://www.sciencedirect.com/science/article/pii/S0092867406009615.

[103] Boris Hinz. "Formation and Function of the Myofibroblast during Tissue Repair". In: *Journal of Investigative Dermatology* 127.3 (2007), pp. 526–537. DOI: https://doi.org/10.1038/sj.jid.5700613.

[104] John P Marinelli et al. "Quantitative Assessment of Lung Stiffness in Patients With Interstitial Lung Disease Using MR Elastography". In: *Journal of Magnetic Resonance Imaging* 46 (2017), pp. 365–374. DOI: 10.1002/jmri.25579.

[105] Yogesh K Mariappan et al. "Estimation of the absolute shear stiffness of human lung parenchyma using H Spin Echo, Echo planar magnetic resonance elastography". In: *Journal of Magnetic Resonance Imaging* 40.5 (2015), pp. 1230–1237. DOI: 10.1002/jmri.24479.Estimation.

[106] Adam J Booth et al. "Acellular Normal and Fibrotic Human Lung Matrices as a Culture System for In Vitro Investigation". In: *American Journal of Respiratory and Critical Care Medicine* 186.9 (2012), pp. 866–876. DOI: 10.1164/rccm.201204-0754OC.

[107] Matthew C Murphy et al. "Regional brain stiffness changes across the Alzheimer's disease spectrum". In: *NeuroImage: Clinical* 10 (2016), pp. 283–290. ISSN: 2213-1582. DOI: 10.1016/j.nicl.2015.12.007. URL: http://dx.doi.org/10.1016/j.nicl.2015.12.007.

[108] Arunark Kolipaka et al. "Magnetic resonance elastography to estimate brain sti ff ness : Measurement reproducibility and its estimate in pseudotumor cerebri patients". In: *Clinical Imaging* 51.January (2018), pp. 114–122. ISSN: 0899-7071. DOI: 10.1016/j.clinimag.2018.02.005. URL: https://doi.org/10.1016/j.clinimag.2018.02.005.

[109] Arvin Arani et al. "Measuring the effects of aging and sex on regional brain stiffness with MR elastography in healthy older adults". In: *NeuroImage* 111 (2015), pp. 59–64. ISSN: 1053-8119. DOI: 10.1016/j.neuroimage.2015.02.016. URL: http://dx.doi.org/10.1016/j.neuroimage.2015.02.016.

[110] Yu Shi et al. "Feasibility of using 3d MR elastography to determine pancreatic stiffness in healthy volunteers". In: *Journal of Magnetic Resonance Imaging* 41.2 (2016), pp. 369–375. DOI: 10.1002/jmri.24572.Feasibility.

[111] Roberta Pozzi et al. "Point shear-wave elastography in chronic pancreatitis : A promising tool for staging disease severity". In: *Pancreatology* 17.6 (2017), pp. 905–910. ISSN: 1424-3903. DOI: 10.1016/j.pan.2017.10.003. URL: https://doi.org/10.1016/j.pan.2017.10.003.

[112] Arunark Kolipaka et al. "Magnetic resonance elasography of the pancreas: Measurement reproducibility and relationship with age". In: *Magnetic Resonance Imaging* 42 (2017), pp. 1–7. DOI: 10.1016/j.mri.2017.04.015.Magnetic.

[113] Nadia Alkhouli et al. "The mechanical properties of human adipose tissues and their relationships to the structure and composition of the extracellular matrix". In: *American Journal of Endocrinology and Metabolism* 305 (2021), pp. 1427–1435. DOI: 10.1152/ajpendo.00111.2013.

[114] Kerstyn Comley and Norman A Fleck. "A micromechanical model for the Young's modulus of adipose tissue". In: *International Journal of Solids and Structures* 47.21 (2010), pp. 2982–2990. ISSN: 0020-7683. DOI: 10.1016/j.ijsolstr.2010.07.001. URL: http://dx.doi.org/10.1016/j.ijsolstr.2010.07.001.

[115] Anthony E Samir et al. "Shear wave elastography in chronic kidney disease : a pilot experience in native kidneys". In: *BMC Nephrology* 16 (2015), pp. 1–9. ISSN: 1471-2369. DOI: 10.1186/s12882-015-0120-7. URL: http://dx.doi.org/10.1186/s12882-015-0120-7.

[116] Arvin Arani et al. "Cardiac MR Elastography for Quantitative Assessment of Elevated Myocardial Stiffness in Cardiac Amyloidosis". In: *Journal of Magnetic Resonance Imaging* 46 (2017), pp. 1361–1367. DOI: 10.1002/jmri.25678.

[117] Ibrahim J Domian, Hanry Yu, and Nikhil Mittal. "On Materials for Cardiac Tissue Engineering". In: *Advanced Healthcare Materials* 6 (2017), pp. 2016–2018. DOI: 10.1002/adhm.201600768.

[118] Sarah F Eby et al. "Shear wave elastography of passive skeletal muscle stiffness: Influences of sex and age throughout adulthood". In: *Clinical Biomechanics* 30.1 (2015), pp. 22–27. ISSN: 0268-0033. DOI: 10.1016/j.clinbiomech.2014.11.011. URL: http://dx.doi.org/10.1016/j.clinbiomech.2014.11.011.

[119] Hio Teng Leong, François Hug, and Siu Ngor Fu. "Increased Upper Trapezius Muscle Stiffness in Overhead Athletes with Rotator Cuff Tendinopathy". In: *PLoS ONE* 11.5 (2016), pp. 1–13. DOI: 10.1371/journal.pone.0155187.

[120] Joline E Brandenburg et al. "Feasibility and Reliability of Quantifying Passive Muscle Stiffness in Young Children by Using Shear Wave". In: *Journal of Ultrasound in Medicine* 34 (2015), pp. 663–670. DOI: 10.7863/ultra.34.4.663.

[121] Robin Souron et al. "Sex differences in active tibialis anterior stiffness evaluated using supersonic shear imaging". In: *Journal of Biomechanics* 49.14 (2016), pp. 3534–3537. ISSN: 0021-9290. DOI: 10.1016/j.jbiomech.2016.08.008. URL: http://dx.doi.org/10.1016/j.jbiomech.2016.08.008.

[122] Horia Stefanescu et al. "Spleen stiffness measurement using fibroscan for the noninvasive assessment of esophageal varices in liver". In: *Journal of Gastroenterology and Hepatology* 26.164-170 (2011). DOI: 10.1111/j.1440-1746.2010.06325.x.

[123] Xiangdong Hu et al. "Indirect Prediction of Liver Fibrosis by Quantitative Measurement of Spleen Stiffness Using the FibroScan System". In: *Journal of Ultrasound in Medicine2* 33.73-81 (14). DOI: 10.7863/ultra.33.1.73.

[124] Aleksander Pawlus et al. "Shear wave elastography of the spleen : evaluation of spleen stiffness in healthy volunteers". In: *Abdominal Radiology* 41 (2016). DOI: 10.1007/s00261-016-0834-4.

[125] Ivan Nenadic, Lance Mynderse, and Douglas Husmann. "Noninvasive Evaluation of Bladder Wall Mechanical Properties as a Function of Filling Volume : Potential Application in Bladder Compliance Assessment". In: *PLoS ONE* 11.6 (2016), pp. 1–14. DOI: 10.1371/journal.pone.0157818.

[126] Toru Hamasaki, Takahiro Yamaguchi, and Masami Iwamoto. "Estimating the influence of age-related changes in skin stiffness on tactile perception for static stimulations". In: *Journal of Biomechanical Science and Engineering* 13.1 (2018), pp. 1–12. DOI: 10.1299/jbse.17-00575.

[127] Leonardo Peñuela et al. "Atomic force microscopy for biomechanical and structural analysis of human dermis : A complementary tool for medical diagnosis and therapy monitoring". In: *Experimental Dermatology* 27 (2018), pp. 150–155. DOI: 10.1111/exd.13468.

[128] Liyun Wang et al. "Quantitative assessment of skin stiffness in localilzed scleroderma using ultrasound shear-wave elastography". In: *Ultrasound in Medicine and Biology* 43.7 (2017), pp. 1339–1347. DOI: 10.1016/j.ultrasmedbio.2017.02.009.

[129] Stuart J Mcdonald et al. "Early Fracture Callus Displays Smooth Muscle-Like Viscoelastic Properties Ex Vivo : Implications for Fracture Healing". In: *Journal of Orthopaedic Research* (2009), pp. 1508–1513. DOI: 10.1002/jor.20923.

[130] Petar Milovanovic et al. "Age-related deterioration in trabecular bone mechanical properties at material level : Nanoindentation study of the femoral neck in women by using AFM". In: *Experimental Gerentology* 47.2 (2012), pp. 154–159. DOI: 10.1016/j.exger.2011.11.011. URL: http://dx.doi.org/10.1016/j.exger.2011.11.011.

[131] Benjamin Yeoman et al. "Adhesion strength and contractility enable metastatic cells to become adurotactic". In: *Cell Reports* 34.108816 (2021), pp. 1–9. ISSN: 2211-1247. DOI: 10.1016/j.celrep.2021.108816. URL: https://doi.org/10.1016/j.celrep.2021.108816.

[132] Tae-hyung Kim et al. "Cancer cells become less deformable and more invasive with activation of β -adrenergic signaling". In: *Journal of Cell Science* 129 (2016), pp. 4563–4575. DOI: 10.1242/jcs.194803.

[133] Tae-Hyung Kim et al. "β-adrenergic signaling modulates cancer cell mechanotype through a RhoA-ROCK-myosin II axis". In: *bioRxiv* (2019). DOI: 10.1101/777755.

[134] Lorenzo Marcucci and Carlo Reggiani. "Mechanosensing in myosin filament solves a 60 years old conflict in skeletal muscle modeling between high power output and slow rise in tension". In: *Frontiers in Physiology* 7.SEP (2016), pp. 1–9. DOI: 10.3389/fphys.2016.00427. arXiv: 1607.05855.

[135] Elizaveta A. Novikova and Cornelis Storm. "Contractile fibers and catch-bond clusters: A biological force sensor?" In: *Biophysical Journal* 105.6 (2013), pp. 1336–1345. ISSN: 00063495. DOI: 10.1016/j.bpj.2013.07.039. URL: http://dx.doi.org/10.1016/j.bpj.2013.07.039.

[136] Lorna E Young, Henry N Higgs, and Cell Biology. "Focal adhesions undergo longitudinal splitting into fixed-width units". In: *Current Biology* 28.13 (2018), pp. 2033–2045. DOI: 10.1016/j.cub.2018.04.073.Focal.

[137] Shiqiong Hu et al. "Structured Illumination Microscopy Reveals Focal Adhesions are Composed of Linear Subunits". In: *Cytoskeleton* 245.May (2015), pp. 235–245. DOI: 10.1002/cm.21223.

[138] Louise P Cramer, Margaret Siebert, and Timothy J Mitchison. "Identification of Novel Graded Polarity Actin Filament Bundles in Locomoting Heart Fibroblasts: Implications for the Generation of Motile Force". In: *The Journal of Cell Biology* 136.6 (1997), pp. 1287–1305. DOI: https://doi.org/10.1083/jcb.136.6.1287.

[139] Michael Mak et al. "Interplay of active processes modulates tension and drives phase transition in self-renewing, motor-driven cytoskeletal networks". In: *Nature Communications* May 2015 (2016). DOI: 10.1038/ncomms10323.

[140] Carly Farris. "The role of myosin head state and binding site availability in calcium-dependent regulation of a muscle mimetic system". In: *Masters Abstracts International* 57.91 (2017).

[141] Bahador Marzaban, Xin Yi, and Hongyan Yuan. "A minimal mechanics model for mechanosensing of substrate rigidity gradient in durotaxis". In: *Biomechanics and Modeling in Mechanobiology* 17.915 (2018). DOI: https://doi.org/10.1007/s10237-018-1001-3.

[142] William J Polacheck and Christopher S Chen. "Measuring cell-generated forces : a guide to the available tools". In: *Nature Methods* 13.5 (2016), pp. 415–423. DOI: 10.1038/nmeth.3834.

[143] Valentina Peschetola et al. "Time-Dependent Traction Force Microscopy for Cancer Cells as a Measure of Invasiveness". In: *Cytoskeleton* 70 (2013), pp. 201–214. DOI: 10.1002/cm.21100.

[144] Casey M. Kraning-Rush, Joseph P. Califano, and Cynthia A. Reinhart-King. "Cellular traction stresses increase with increasing metastatic potential". In: *PLoS ONE* 7.2 (2012). DOI: 10.1371/journal.pone.0032572.

[145] Thornsten M Koch et al. "3D Traction Forces in Cancer Cell Invasion Thorsten". In: *PLoS ONE* 67.11 (2017), pp. 1664–1669. DOI: 10.1371/journal.pone.0033476. arXiv: 1203.2655.

[146] Zhen Li et al. "Cellular traction forces: a useful parameter in cancer research". In: *Nanoscale* 9 (2017), pp. 19039–19044. DOI: 10.1039/c7nr06284b.

[147] Marco Linari et al. "Force generation by skeletal muscle is controlled by mechanosensing in myosin filaments". In: *Nature* 528 (2015), pp. 576–279. ISSN: 0028-0836. DOI: 10.1038/nature15727.

[148] Lennart Hilbert et al. "The kinetics of mechanically coupled myosins exhibit group size-dependent regimes". In: *Biophysical Journal* 105.6 (2013), pp. 1466–1474. ISSN: 00063495. DOI: 10.1016/j.bpj.2013.07.054. URL: http://dx.doi.org/10.1016/j.bpj.2013.07.054.

[149] Bryant L Doss et al. "Cell response to substrate rigidity is regulated by active and passive cytoskeletal stress". In: *Proceedings of the National Academy of Sciences* 117.23 (2020), pp. 12817–12825. DOI: 10.1073/pnas.1917555117.

[150] Rebecca G Wells. "The Role of Matrix Stiffness in Regulating Cell Behavior". In: *Hepatology* 47.4 (2008), pp. 1394–1400. DOI: 10.1002/hep.22193.

[151] Hans Van Oosterwyck. "Modeling of Mechanosensing Mechanisms Reveals Distinct Cell Migration Modes to Emerge From Combinations of Substrate Stiffness and Adhesion Receptor-Ligand Affinity". In: *Frontiers in Bioengineering and Biotechnology* 8.June (2020), pp. 1–19. DOI: 10.3389/fbioe.2020.00459.

[152] Robert J. Pelham and Yu-li Wang. "Cell locomotion and focal adhesions are regulated by substrate flexibility". In: *Proceedings of the National Academy of Sciences* 95 (1998), pp. 13661–13665. DOI: https://doi.org/10.1073/pnas.94.25.13661.

[153] Hong-bei Wang et al. "Substrate flexibility regulates growth and apoptosis of normal but not transformed cells". In: *American Journal of Cell Physiology* 279 (200), pp. 1345–1350. DOI: https://doi.org/10.1152/ajpcell.2000.279.5.c1345.

[154] Jenny Z Kechagia and Johanna Ivaska. "Integrins as biomechanical sensors of the microenvironment". In: *Nature Reviews Molecular Cell Biology* 20 (2019), pp. 457–473. ISSN: 1471-0080. DOI: 10.1038/s41580-019-0134-2. URL: http://dx.doi.org/10.1038/s41580-019-0134-2.

[155] Anna Huttenlocher and Alan Rick Horwitz. "Integrins in Cell Migration". In: *Cold Spring Harbor Perspectives in Biology* (2019). DOI: doi:10.1101/cshperspect.a005074.

[156] Alexander Bershadsky, Michael Kozlov, and Benjamin Geiger. "Adhesion-mediated mechanosensitivity: a time to experiment, and a time to theorize". In: *Current Opinion in Cell Biology* 18.5 (2006), pp. 472–481. DOI: 10.1016/j.ceb.2006.08.012.

[157] B. Geiger and A. Bershadsky. "Assembly and mechanosensory function of focal contacts". In: *Current Opinion in Cell Biology* 13.5 (2001), pp. 584–592. DOI: 10.1016/S0955-0674(00)00255-6.

[158] Benjamin Geiger, Joachim P Spatz, and Alexander D Bershadsky. "Environmental sensing through focal adhesions". In: *Nature Reviews Molecular Cell Biology* 10 (2009). DOI: 10.1038/nrm2593.

[159] Mingxi Yao et al. "The mechanical response of talin". In: *Nature Communications* 7.May (2016), pp. 1–11. DOI: 10.1038/ncomms11966.

[160] Soham Chakraborty et al. "Force-Directed Mechanointeractome of Talin-Integrin". In: *Biochemistry* 58 (2019), pp. 4677–4695. DOI: 10.1021/acs.biochem.9b00442.

[161] David R Critchley. "Smurf1 zaps the talin head". In: *Nature Cell Biology* 11.5 (2009), pp. 2008–2010. DOI: https://doi.org/10.1038/ncb0509-538.

[162] Ian Fillingham et al. "A vinculin binding domain from the talin rod unfolds to form a complex with the vinculin head". In: *Structure* 13.1 (2005), pp. 65–74. DOI: 10.1016/j.str.2004.11.006.

[163] Paul R Elliott et al. "The Structure of the Talin Head Reveals a Novel Extended Conformation of the FERM Domain". In: *Structure* 18 (2010), pp. 1289–1299. DOI: 10.1016/j.str.2010.07.011.

[164] Elias Lazarides. "Actin, α-actinin, and tropomyosin interaction in the structural organization of actin filaments in nonmuscle cells". In: *The Journal of Cell Biology* 68 (1976), pp. 202–219. DOI: https://doi.org/10.1083/jcb.68.2.202.

[165] Magdalena Chrzanowska-wodnicka and Keith Burridge. "Rho-stimulated Contractility Drives the Formation of Stress Fibers and Focal Adhesions". In: *Journal of Cell Biology* 133.6 (1996), pp. 1403–1415. DOI: doi:10.1083/jcb.133.6.1403.

[166] Keith Burridge and Christophe Guilluy. "Focal adhesions, stress fibers and mechanical tension". In: *Experimental Cell Research* 343.1 (2016), pp. 14–20. DOI: 10.1002/jmri.25711.PET/MRI.

[167] Patrick W Oakes et al. "Lamellipodium is a myosin-independent mechanosensor". In: *Proceedings of the National Academy of Sciences* 115.11 (2018), pp. 2646–2651. DOI: 10.1073/pnas.1715869115.

[168] Benjamin T Goult et al. "Structure of a double ubiquitin-like domain in the talin head: A role in integrin activation". In: *The EMBO Journal* June 2014 (2010). DOI: 10.1038/emboj.2010.4.

[169] Esen Goksoy et al. "Article Structural Basis for the Autoinhibition of Talin in Regulating Integrin Activation". In: *Molecular Cell* 31 (2008), pp. 124–133. DOI: 10.1016/j.molcel.2008.06.011.

[170] Anjana Nayal, Donna J Webb, and Alan F Horwitz. "Talin : an emerging focal point of adhesion dynamics". In: *Current Opinion in Cell Biology* 16 (2004), pp. 94–98. DOI: 10.1016/j.ceb.2003.11.007.

[171] Keith Burridge and Laurie Connell. "Talin : A Cytoskeletal Component Concentrated in Adhesion Plaques and Other Sites of Actin-Membrane Interaction". In: *Cell Motility* 3 (1983), pp. 405–417. DOI: doi:10.1002/cm.970030509..

[172] Jia-huai Wang. "Pull and push : Talin activation for integrin signaling". In: *Nature Publishing Group* 22.11 (2012), pp. 1512–1514. ISSN: 1001-0602. DOI: 10.1038/cr.2012.103.

[173] Sari Tojkander et al. "Generation of contractile actomyosin bundles depends on mechanosensitive actin filament assembly and disassembly". In: *eLife* 4 (2015), pp. 1–28. DOI: 10.7554/elife.06126.

[174] Todd Thoresen, Martin Lenz, and Margaret L Gardel. "Thick Filament Length and Isoform Composition Determine Self-Organized Contractile Units in Actomyosin Bundles". In: *Biophysical Journalj* 104.3 (2013), pp. 655–665. ISSN: 0006-3495. DOI: 10.1016/j.bpj.2012.12.042. URL: http://dx.doi.org/10.1016/j.bpj.2012.12.042.

[175] Neil Billington et al. "Characterization of three full-length human nonmuscle myosin II paralogs". In: *Journal of Biological Chemistry* 288.46 (2013), pp. 33398–33410. DOI: 10.1074/jbc.M113.499848.

[176] Alexander B. Verkhovsky and Gary Borisy. "Non-Sarcomeric Mode of Myosin II Organization in the Fibroblast Lamellum". In: *Journal of Cell Biology* 123.3 (1993), pp. 637–652. DOI: https://doi.org/10.1083/jcb.123.3.637.

[177] Anabelle Opazo Saez et al. "Tension development during contractile stimulation of smooth muscle requires recruitment of paxillin and vinculin to the membrane". In: *American Journal of Cell Physiology* 286 (2003), pp. 433–447. DOI: 10.1152/ajpcell.00030.2003.

[178] Javad Golji and Mohammad R K Mofrad. "The Interaction of Vinculin with Actin". In: *PLoS Computational Biology* 9.4 (2013). DOI: 10.1371/journal.pcbi.1002995.

[179] Alberto Elosegui-Artola et al. "Image Analysis for the Quantitative Comparison of Stress Fibers and Focal Adhesions". In: *PLoS ONE* 9.9 (2014). DOI: 10.1371/journal.pone.0107393.

[180] Sam Walcott, David M. Warshaw, and Edward P. Debold. "Mechanical coupling between myosin molecules causes differences between ensemble and single-molecule measurements". In: *Biophysical Journal* 103.3 (2012), pp. 501–510. DOI: 10.1016/j.bpj.2012.06.031. URL: http://dx.doi.org/10.1016/j.bpj.2012.06.031.

[181] James A. Spudich. "The myosin swinging cross-bridge model". In: *Nature Reviews Molecular Cell Biology* 2.5 (2001), pp. 387–392. ISSN: 14710072. DOI: 10.1038/35073086.

[182] C David Williams, Michael Regnier, and Thomas L Daniel. "Axial and Radial Forces of Cross-Bridges Depend on Lattice Spacing". In: *PLoS Computational Biology* 6.12 (2010). DOI: 10.1371/journal.pcbi.1001018.

[183] Mihály Kovács et al. "Functional divergence of human cytoplasmic myosin II. Kinetic characterization of the non-muscle IIA isoform". In: *Journal of Biological Chemistry* 278.40 (2003), pp. 38132–38140. DOI: 10.1074/jbc.M305453200.

[184] John Jeremy Rice et al. "Ising Model of Cardiac Thin Filament Activation with Nearest-Neighbor Cooperative Interactions". In: *Biophysical Journal* 84.February (2003), pp. 897–909. DOI: https://doi.org/10.1016/s0006-3495(03)74907-8.

[185] Farah Sheikh et al. "Mouse and computational models link Mlc2v dephosphorylation to altered myosin kinetics in early cardiac disease". In: *The Journal of Clinical Investigation* 122.4 (2012), pp. 1209–1221. DOI: 10.1172/JCI61134DS1.

[186] Julien Colombelli et al. "Mechanosensing in actin stress fibers revealed by a close correlation between force and protein localization". In: *Journal of Cell Science* 122 (2009), pp. 1665–1679. DOI: 10.1242/jcs.054577.

[187] David Boettiger et al. "Distinct Ligand-Binding Modes for Integrin $\alpha_v\beta_3$-Mediated Adhesion to Fibronectin Versus Vitronectin *". In: *Journal of Biological Chemistry* 276.34 (2001), pp. 31684–31690. ISSN: 0021-9258. DOI: 10.1074/jbc.M103997200. URL: http://dx.doi.org/10.1074/jbc.M103997200.

[188] Sabyasachi Rakshit and Sanjeevi Sivasankar. "regulates the lifetime of adhesive bonds at the single molecule level". In: *Physical Chemistry Chemical Physics* 16 (2014), pp. 2211–2223. DOI: 10.1039/c3cp53963f.

[189] Steven J Tan et al. "Regulation and dynamics of force transmission at individual cell-matrix adhesion bonds". In: *Science Advances* 6 (2020), pp. 1–12. DOI: https://doi.org/10.1126/sciadv.aax0317.

[190] Xuefeng Wang et al. "Article Integrin Molecular Tension within Motile Focal Adhesions". In: *Biophysical Journal* 109.11 (2015), pp. 2259–2267. ISSN: 0006-3495. DOI: 10.1016/j.bpj.2015.10.029.

[191] Manuel Zundel, Alexander E Ehret, and Edoardo Mazza. "Factors influencing the determination of cell traction forces". In: 12.2 (2017), pp. 1–18. DOI: 10.1371/journal.pone.0172927.

[192] Mihály Kovács et al. "Load-dependent mechanism of nonmuscle myosin 2". In: *Proceedings of the National Academy of Sciences* 104.24 (2007), pp. 9994–9999. DOI: https://doi.org/10.1073/pnas.0701181104.

[193] Harold P Erickson. "Reversible unfolding of fibronectin type III and immunoglobulin domains provides the structural basis for stretch and elasticity of titin and fibronectin". In: *Proceedings of the National Academy of Sciences of the United States of America* 91.October (1994), pp. 10114–10118. DOI: https://doi.org/10.1073/pnas.91.21.10114.

[194] Olivier Thoumine et al. "Short-term binding of fibroblasts to fibronectin: optical tweezers experiments and probabilistic analysis". In: *European Biophysics Journal* 29 (2000), pp. 398–408. DOI: https://doi.org/10.1007/s002490000087.

[195] Douglas A Lauffenburger and Alan F Horwitz. "Cell Migration : A Physically Integrated Molecular Process". In: *Cell* 84 (1996), pp. 359–369. DOI: https://doi.org/10.1016/s0092-8674(00)81280-5.

[196] Rishita Changede and Michael Sheetz. "Integrin and cadherin clusters: A robust way to organize adhesions for cell mechanics". In: *BioEssays* 39.1600123 (2016), pp. 1–12. DOI: 10.1002/bies.201600123.

[197] John L Tan et al. "Cells lying on a bed of microneedles : An approach to isolate mechanical force". In: *Proceedings of the National Academy of Sciences* 2002.100 (2003), pp. 1484–1489. DOI: https://doi.org/10.1073/pnas.0235407100.

[198] Jonathan Stricker et al. "Spatiotemporal Constraints on the Force-Dependent Growth of Focal Adhesions". In: *Biophysical Journal* 100.12 (2011), pp. 2883–2893. ISSN: 0006-3495. DOI: 10.1016/j.bpj.2011.05.023. URL: http://dx.doi.org/10.1016/j.bpj.2011.05.023.

[199] Marion Ghibaudo et al. "Traction forces and rigidity sensing regulate cell functions". In: *Soft Matter* 4 (2008), pp. 1836–1843. DOI: 10.1039/b804103b.

[200] Thomas R Polte et al. "Extracellular matrix controls myosin light chain phosphorylation and cell contractility through modulation of cell shape and cytoskeletal prestress". In: *American Journal of Physiology - Cell Physiology* 286 (2004), pp. 518–528. DOI: 10.1152/ajpcell.00280.2003.

[201] Ying Li, Prabhakar Bhimalapuram, and Aaron R Dinner. "Model for how retrograde actin flow regulates adhesion traction stresses". In: *Journal of Physics: Condensed Matter* 22 (2010). DOI: 10.1088/0953-8984/22/19/194113.

[202] Margaret L Gardel et al. "Traction stress in focal adhesions correlates biphasically with actin retrograde flow speed". In: *Journal of Cell Biology* 183.6 (2008), pp. 999–1005. DOI: 10.1083/jcb.200810060.

[203] Erin M Craig et al. "Model for adhesion clutch explains biphasic relationship between actin flow and traction at the cell leading edge". In: *Physical Biology* 12 (2015). DOI: 10.1088/1478-3975/12/3/035002.

[204] Jonathon Howard. *Mechanics of Motor Proteins and the Cytoskeleton*. Vol. 75. Springer Berlin Heidelberg, 2002, pp. 69–94. DOI: https://doi.org/10.1007/3-540-45701-1_2.

[205] Bo Cheng et al. "Nanoscale integrin cluster dynamics controls cellular mechanosensing via FAKY397 phosphorylation". In: *Science Advances* 6 (2020). DOI: https://doi.org/10.1126/sciadv.aax1909.

[206] M Maraldi, C Valero, and K Garikipati. "A Computational Study of Stress Fiber-Focal Adhesion Dynamics Governing Cell Contractility". In: *Biophysj* 106.9 (2014), pp. 1890–1901. ISSN: 0006-3495. DOI: 10.1016/j.bpj.2014.03.027. URL: http://dx.doi.org/10.1016/j.bpj.2014.03.027.

[207] Kazuo Kitamura et al. "A single myosin head moves along an actin filament with regular steps of 5.3 nanometres". In: *Nature* 397.14 (1999), pp. 129–134. DOI: https://doi.org/10.1038/16403.

[208] Fang Kong et al. "Demonstration of catch bonds between an integrin and its ligand". In: *The Journal of Cell Biology* 185.7 (2009), pp. 1275–1284. DOI: 10.1083/jcb.200810002.

[209] Marie-France Carlier, Guillaume Romet-Lemonne, and Antoine Jegou. "Actin Filament Dynamics Using Microfluidics". In: *Methods in Enzymology*. Vol. 540. Academic Press, 2014. Chap. 1, pp. 3–17.

[210] Rafael Tapia-rojo, Alvaro Alonso-caballero, and Julio M Fernandez. "Direct observation of a coil-to-helix contraction triggered by vinculin binding to talin". In: *Science Advances* 6.May (2020), pp. 1–8. DOI: https://doi.org/10.1126/sciadv.aaz4707.